FACULDADE DE ENGENHARIA DA UNIVERSIDADE DO PORTO

Supersonic Flutter of Variable Stiffness Circular Cylindrical Shells

Duarte José Lourenço Cachulo

A Dissertation submitted for the degree of Master of Science in Mechanical Engineering
to Faculdade de Engenharia, Universidade do Porto

Supervisor: Dr. Pedro Leal Ribeiro

Co-supervisor: Dr. Hamed Akhavan

August 4, 2022

Supersonic Flutter of Variable Stiffness Circular Cylindrical Shells

Duarte José Lourenço Cachulo

A Dissertation submitted for the degree of Master of Science in Mechanical Engineering to Faculdade de Engenharia, Universidade do Porto

Approved in oral examination by the committee:

Chair: Prof. José Fernando Dias Rodrigues

External Examiner: Prof. Pedro Gamboa

Supervisor: Prof. Pedro Leal Ribeiro

August 4, 2022

This research was carried out in the framework of project Nº 030348, POCI-01-0145-FEDER-030348, "Laminated composite panels reinforced with carbon nanotubes and curvilinear carbon fibres for enhanced vibration and flutter characteristics", funded by FEDER, through Programa Operacional Competitividade e Internacionalização – COMPETE 2020, and by National Funds (PIDDAC), through FCT/MCTES.

Cofinanciado por:

COMPETE 2020

PORTUGAL 2020

UNIÃO EUROPEIA
Fundo Europeu
de Desenvolvimento Regional

Abstract

Fiber-reinforced composite laminates are commonly used in many engineering applications where light weight design is necessary for a good structural performance, like in the aeronautic and aerospace industries. Variable stiffness composite laminates (VSCL) have emerged as a specific case of fiber-reinforced composite laminates, that, instead of being constituted by layers with conventional unidirectional tows, are composed by layers with curvilinear fibers that allow to tailor the structure's elastic properties to the expected external loads. In the recent years, efforts have been made to further develop the design and manufacturing techniques of this type of structure, as they present a promising way of improving the mechanical properties of plates and shells.

In this dissertation, the critical free stream static pressure of a supersonic airflow along the axial direction of a VSCL cylindrical shell is calculated with the intent of understanding how the use of curvilinear fibers can prevent the occurrence of the flutter aeroelastic instability. By increasing the pressure at which this phenomenon occurs, even lighter structures can be designed, which is beneficial in numerous applications.

For this work, a linear mathematical model for a thin and circular cylindrical VSCL shell is developed. The equations of motion are obtained resorting to Newton's second law of motion. The aerodynamic pressure caused by the supersonic airflow is modelled recurring to the linearized piston theory. Finally, the p-version of the finite element method is used to discretize the mathematical model, so the natural frequencies and mode shapes of the shell under free vibration and the critical flutter conditions can be obtained.

A convergence test is performed and the model is validated by comparing the values of natural frequency and critical flutter free stream pressure with values found in the literature. Both clamped and simply supported boundary conditions are tested.

Finally, various curvilinear fiber paths, defined by mathematical expressions, are tweaked to find paths that result in higher values of critical flutter free stream pressure comparing to the values obtained for a conventional constant stiffness composite laminate shell.

Keywords: Variable stiffness composite laminates, Curvilinear fibers, Cylindrical shell, p-version finite element method, Linear model, Piston theory, Natural frequency, Natural modes of vibration, Supersonic flutter.

Resumo

Compósitos laminados reforçados por fibras são comumente usados em muitas aplicações de engenharia onde o projeto focado na obtenção de estruturas leves é fulcral para o bom desempenho mecânico, tal como acontece na indústria aeronáutica e aeroespacial. Compósitos laminados de rigidez variável (VSCL) surgiram como um caso específico de compósitos laminados reforçados por fibras que, ao invés de serem constituídos por camadas com fibras unidirecionais convencionais, são compostos por camadas com fibras curvilíneas que permitem ajustar as propriedades elásticas da estrutura às cargas externas esperadas. Nos últimos anos, esforços têm sido feitos no sentido de desenvolver as técnicas de projeto e produção deste tipo de estrutura, visto que apresentam uma forma promissora de melhorar as propriedades mecânicas de placas e cascas.

Nesta dissertação, a pressão estática crítica de um escoamento supersónico de ar ao longo da direção axial de uma casca VSCL cilíndrica é calculada com a intenção de perceber como é que o uso de fibras curvilíneas pode prevenir a ocorrência da instabilidade aeroelástica *flutter*. Aumentando a pressão a que este fenómeno ocorre, estruturas com ainda menos peso podem ser produzidas, o que é benéfico em várias aplicações.

Para este trabalho, um modelo linear matemático para uma casca VSCL cilíndrica e fina é desenvolvido. As equações de movimento são obtidas recorrendo à segunda lei de Newton. A pressão aerodinâmica causada pelo escoamento de ar supersónico é modelada recorrendo à teoria linearizada do pistão. Finalmente, a versão-p do método dos elementos finitos é usada para discretizar o modelo matemático, de forma a que seja possível obter a resposta dinâmica da casca sob vibração livre e sob condições de *flutter*.

Testes de convergência são realizados e o modelo é validado comparando os valores das frequências naturais e da pressão estática crítica a que o *flutter* ocorre com valores encontrados na literatura. As condições de fronteira de encastre e de extremidades simplemente apoiadas são testadas.

Por fim, vários trajetos de fibras curvilíneas são testados. Estes são definidos por expressões matemáticas e os seus parâmetros foram progressivamente ajustados para encontrar trajetos que resultam em maiores valores de pressão estática crítica a que o *flutter* ocorre do que os encontrados para uma casca convencional de rigidez constante.

Palavras-chave: Compósito laminado de rigidez variável, Fibras curvilíneas, Casca cilíndrica, Versão-p do método dos elementos finitos, Modelo linear, Teoria do pistão, Frequência natural, Modos naturais de vibração, *Flutter* supersónico.

Acknowledgements

The present work comes as the culmination of 5 years of hard work, acquired knowledge and much personal and professional development, and I couldn't be more grateful for the journey I went through in this course for which I have such passion.

Firstly, I would like to thank the institution that invested in my development as a future engineer, Faculdade de Engenharia da Universidade do Porto, and all the people that, in some way, have influenced my growth, shared knowledge and helped me build the vision of what type of engineer I aspire to be.

I am very grateful for my supervisors Prof. Dr. Pedro Leal Ribeiro and Dr. Hamed Akhavan, for their guidance, support and for all the knowledge they shared that was pivotal for the completion of this work and that gave me the confidence and resources to overcome the most challenging aspects of this proccess.

During this work I benefited from a research grant for the project POCI-01-0145-FEDER-030348 "Aperfeiçoamento das características dinâmicas e da resistência a instabilidades aeroelásticas de painéis em materiais compósitos através de nanotubos de carbono e de fibras de carbono curvilíneas", FEDER/COMPETE 2020/PIDDAC - FCT/MCTES, a project funded by the Portuguese Science and Technology Foundation (Fundação para a Ciência e a Tecnologia - FCT) and attributed to me by the Institute of Science and Innovation in Mechanical Engineering and Industrial Engineering (Instituto de Ciência e Inovação em Engenharia Mecânica e Engenharia Industrial - INEGI). I am very grateful for this support.

An important part of my life is my family, and their support, not only through the development of this dissertation, but through all of my academic journey, is the main reason that I am able to finish my master's degree successfully. I am forever grateful for their loving presence in my life.

Lastly, I want to thank my girlfriend and my friends for their support, patience and contributions to my happiness throughout these years. I am extremely lucky to confidently say that I am surrounded by the best people.

A big thank you to you all.

Duarte Cachulo

"Eles não sabem, nem sonham,
que o sonho comanda a vida.
Que sempre que um homem sonha
o mundo pula e avança
como bola colorida
entre as mãos de uma criança."

António Gedeão

Contents

1 Introduction **1**
1.1 Overview and Motivation . . . 1
1.2 Introduction of Concepts . . . 1
1.2.1 Fiber Reinforced Composite Laminate Shells . . . 2
1.2.2 Variable Stiffness Composite Laminates . . . 2
1.2.3 Supersonic Flutter . . . 10
1.3 Literature Review . . . 10
1.4 Objectives . . . 12
1.5 Layout . . . 12

2 Mathematical Model **15**
2.1 Introduction . . . 15
2.2 Love's First Approximation . . . 16
2.3 Kinematic Relations . . . 17
2.4 Fundamental Equations of Elasticity . . . 18
2.5 Equations of Motion . . . 22
2.6 Boundary Conditions . . . 23
2.7 Aerodynamic Pressure . . . 25
2.8 The p-version Finite Element Method . . . 25
2.8.1 Shape Functions . . . 26
2.8.2 Stiffness and Mass Matrix Calculation . . . 30
2.8.3 Natural Frequencies and Natural Mode Shapes . . . 38
2.9 Implementing Viscous Damping . . . 39
2.10 Supersonic Flutter . . . 39
2.11 Conclusion . . . 43

3 Model Validation **45**
3.1 Introduction . . . 45
3.2 Convergence Test . . . 45
3.3 Natural Frequencies and Mode Shapes of Vibration . . . 48
3.4 Supersonic Flutter . . . 50
3.5 Conclusions . . . 54

4 Supersonic Flutter of Fiber Reinforced Composite Laminate Cylindrical Shells **57**
4.1 Introduction . . . 57
4.2 Shells with Clamped Boundary Conditions . . . 58
4.2.1 Constant Stiffness Composite Laminates . . . 58
4.2.2 VSCL with Linear Angle Variation Paths: 1 Segment . . . 60

4.2.3 VSCL with Constant in-Plane Curvature Paths: 1 Segment 62
4.2.4 VSCL with Linear Angle Variation Paths: 2 Segments 63
4.2.5 VSCL with Constant in-Plane Curvature Paths: 2 Segments 65
4.2.6 Frequency Analysis 67
4.3 Simply Supported Boundary Conditions Comparison 69
4.4 Conclusions 73

5 Conclusions and Future Work **75**
5.1 Summary 75
5.2 Future Work 77

References **79**

List of Figures

1.1 Tow angle ψ representation of a lamina in a: a) constant stiffness case; b) variable stiffness case. . . . 3
1.2 Schematic view of an advanced fiber placement machine head (reprinted with permission from Evans [3]). . . . 4
1.3 Gap and overlap representation of two adjacent tow paths. . . . 5
1.4 Lamina with 0% and 100% coverage. . . . 6
1.5 Cylinder with a representation of a generic tow path and the angle variation and shifting directions. . . . 7
1.6 Tow path representation for a) linear variation of fiber orientation, b) linear variation of fiber orientation with two segments, c) constant in-plane curvature, d) constant in-plane curvature with two segments ($T_0 = 70º$, $T_1 = 0º$). . . . 9

2.1 Cylindrical shell relevant dimensions and coordinate system (3D view and cross sectional view). . . . 16
2.2 Laminae stacking sequence and nomenclature. . . . 21
2.3 Schematic representation of a circular cylindrical shell subjected to the studied supersonic airflow. . . . 25
2.4 First seven shape functions of the f set. . . . 27
2.5 First seven shape functions of the g set. . . . 28
2.6 Plot of the $e^{t\cdot\mathfrak{Re}(\Omega)}\left[\sqrt{(\mathfrak{Re}(q_i))^2+(\mathfrak{Im}(q_i))^2}\cdot cos\left(\mathfrak{Im}(\Omega)\cdot t+arctan\left(\frac{\mathfrak{Im}(q_i)}{\mathfrak{Re}(q_i)}\right)\right)\right]$ function, for a positive $\mathfrak{Re}(\Omega)$ and for a negative $\mathfrak{Re}(\Omega)$. . . . 42

3.1 Natural mode shapes of a three layered, cross-ply [0º/90º/0º] circular cylindrical shell with C-C boundary conditions ($R = 1$, $l/R = 5$, $h/R = 0.002$, $E_{22} = 7.6$ GPa, $E_{11}/E_{22} = 2.5$, $G_{12} = 4.1$ GPa, $\nu_{12} = 0.26$, $\rho = 1643$ kg/m^3, $m = 1$). . . . 49
3.2 Comparison of the plot of the mode shapes with $m = 1$ and $n = 6$ for a cross ply [0º/90º/0º] circular cylindrical shell with C-C and S-S boundary conditions ($R = 1$ m, $l/R = 5$, $h/R = 0.002$, $E_{22} = 7.6$ GPa, $E_{11}/E_{22} = 2.5$, $G_{12} = 4.1$ GPa, $\nu_{12} = 0.26$, $\rho = 1643$ kg/m^3). . . . 49
3.3 a) $\mathfrak{Re}(\Omega)$ and b) $\mathfrak{Im}(\Omega)$ variation along p_∞ of 2 modes of the first test. . . . 52
3.4 Flutter mode shapes corresponding to points A and B of the plot of the first flutter test ($n_{crit} = 25$). . . . 53
3.5 Flutter mode shapes corresponding to the complex conjugates of points A and B of the plot of the first flutter test ($n_{crit} = 25$). . . . 53

4.1 p_{crit} and n_{crit} for various values of T_0 of a CSCL cylindrical shell. . . . 59
4.2 Critical flutter mode shape of a CSCL shell with $T_0 = 55º$ ($n_{crit} = 20$). . . . 59
4.3 Critical flutter mode shape of a CSCL shell with $T_0 = 40º$ ($n_{crit} = 3$). . . . 59

4.4 Linear angle variation path with 1 segment for $T_0 = 70^o$ and $T_1 = 0^o$. 60
4.5 Critical flutter mode shape of a VSCL shell with a <40º,80º> fiber path ($n_{crit} = 16$). 61
4.6 Constant curvature path with 1 segment for $T_0 = 70^o$ and $T_1 = 0^o$. 62
4.7 Critical flutter mode shape of a VSCL shell with a <25º,85º>$_c$ fiber path ($n_{crit} = 16$). 63
4.8 Linear angle variation path with 2 segments for $T_0 = 70^o$ and $T_1 = 0^o$. 64
4.9 Critical flutter mode shape of a VSCL shell with a <85º,55º,85º> fiber path ($n_{crit} = 16$). 65
4.10 Constant curvature path with 2 segments for $T_0 = 70^o$ and $T_1 = 0^o$. 65
4.11 Critical flutter mode shape of a VSCL shell with a <85º,45º,85º>$_c$ fiber path ($n_{crit} = 17$). 66
4.12 $\mathfrak{Re}(\Omega)$ and $\mathfrak{Im}(\Omega)$ variation along p_∞ of the critical flutter mode and its corresponding coupled mode for a shell $\psi = 55^o$ tow path and a <25º,85º>$_c$ fiber path. 67
4.13 Natural mode shape of free vibration corresponding to $\omega = 1844$ rad/s of a CSCL shell with $\psi = 55^o$. 68
4.14 Natural mode shape of free vibration corresponding to $\omega = 1961$ rad/s of a CSCL shell with $\psi = 55^o$. 68
4.15 Natural mode shape of free vibration corresponding to $\omega = 1052$ rad/s of a VSCL shell with the <25º,85º>$_c$. 68
4.16 Natural mode shape of free vibration corresponding to $\omega = 1522$ rad/s of a VSCL shell with the <25º,85º>$_c$. 69
4.17 Critical flutter mode shape of a CSCL shell with $T_0 = 55^o$ and S-S boundary conditions ($n_{crit} = 18$). 70
4.18 Critical flutter mode shape of a VSCL shell with a <40º,80º> tow path and S-S boundary conditions ($n_{crit} = 14$). 70
4.19 Critical flutter mode shape of a VSCL shell with a <25º,85º>$_c$ tow path and S-S boundary conditions ($n_{crit} = 14$). 70
4.20 Critical flutter mode shape of a VSCL shell with a <85º,55º,85º> tow path and S-S boundary conditions ($n_{crit} = 15$). 71
4.21 Critical flutter mode shape of a VSCL shell with a <85º,45º,85º>$_c$ tow path and S-S boundary conditions ($n_{crit} = 15$). 71
4.22 $\mathfrak{Re}(\Omega)$ and $\mathfrak{Im}(\Omega)$ variation along p_∞ of the critical flutter mode and its corresponding coupled mode for a shell with C-C and S-S boundary conditions and a <40º,80º> tow path. 72

List of Tables

3.1 Convergence study of the lowest natural frequency ω_1 for a three layered, cross-ply [0º/90º/0º] circular cylindrical shell with C-C boundary conditions ($R = 1$ m, $l/R = 5$, $h/R = 0.002$, $E_{22} = 7.6$ GPa, $E_{11}/E_{22} = 2.5$, $G_{12} = 4.1$ GPa, $\nu_{12} = 0.26$, $\rho = 1643$ kg/m^3). 46

3.2 Convergence study of the lowest natural frequency ω_1 for a three layered, cross-ply [0º/90º/0º] circular cylindrical shell with S-S boundary conditions ($R = 1$ m, $l/R = 5$, $h/R = 0.002$, $E_{22} = 7.6$ GPa, $E_{11}/E_{22} = 2.5$, $G_{12} = 4.1$ GPa, $\nu_{12} = 0.26$, $\rho = 1643$ kg/m^3). 47

3.3 Frequency parameters $\Omega = \omega R\sqrt{\rho/E_{22}}$ for a three layered, cross-ply [0º/90º/0º] circular cylindrical shell with C-C and S-S boundary conditions ($l/R = 5$, $h/R = 0.002$, $E_{22} = 7.6$ GPa, $E_{11}/E_{22} = 2.5$, $G_{12} = 4.1$ GPa, $\nu_{12} = 0.26$, $\rho = 1643$ kg/m^3, $m = 1$). 48

3.4 Frequency parameters $\Omega = \omega R\sqrt{\rho/E_{22}}$ of the fundamental natural frequency for a four layered, angle-ply circular cylindrical shell with C-C and S-S boundary conditions ($l/R = 4$, $h/R = 0.01$, $E_{11}/E_{22} = 20$, $G_{12}/E_{22} = 0.65$, $\nu_{12} = 0.25$). . . 50

3.5 Critical free stream pressure p_{crit} (Pa) for the occurrence of flutter for S-S boundary conditions of circular cylindrical shells with the following parameters: $G_{12} = E_{11}/[2\cdot(1+\nu_{12})]$, $h = 0.0001015$ m, $R = 0.203$ m, $\rho = 8900$ kg/m^3, $M = 3$, $a_\infty = 213$ m/s, $\gamma = 1.4$. 51

4.1 Shell and airflow parameters for the performed tests. 57

4.2 Critical free stream pressure p_{crit} for shells with linear angle variation fiber paths <T_0,T_1>. 61

4.3 Critical free stream pressure p_{crit} for shells with constant in-plane curvature paths <T_0,T_1>$_c$. 62

4.4 Critical free stream pressure p_{crit} for shells with linear angle variation fiber paths <T_1,T_0,T_1>. 64

4.5 Critical free stream pressure p_{crit} for shells with constant in-plane curvature fiber paths <T_1,T_0,T_1>$_c$. 66

4.6 Critical free stream pressure p_{crit} and number of circumferential waves of the corresponding mode n_{crit} for shells with C-C and S-S boundary conditions. 69

4.7 Critical free stream pressure p_{crit} for shells with C-C and S-S boundary conditions and linear angle variation paths. 72

Nomenclature

a_∞	Speed of sound
E_{11}, E_{22}, E_{33}	Young's moduli
G_{12}, G_{13}, G_{23}	Shear moduli
g_r	Shape function for membrane displacements u_0 and v_0 along the ξ coordinate
g_{ur}, g_{vr}	Shape function for membrane displacements u_0 and v_0 along the ξ coordinate
f_r	Shape function for transverse displacement w_0 along the ξ coordinate
h_{ur}, h_{vr}, h_{wr}	Shape function for displacement u_0, v_0 and w_0 along the θ coordinate
h	Cylindrical shell's thickness
l	Cylindrical shell's length
k_{xx}, $k_{\theta\theta}$	Shell's change of curvature in the polar coordinate system
$k_{x\theta}$	Shell's twist in the polar coordinate
N_{ij}	Shell's inner force resultant in the ij direction
n	Number of circumferential waves for free vibration / flutter modes
n_{crit}	Number of circumferential waves of the first mode that achieves flutter
M_{ij}	Shell's inner moment resultant in the ij direction
M	Mach number
m	Number of axial waves for free vibration / flutter modes
p_∞	Free flow static pressure
p_a	Aerodynamic pressure
p_{crit}	Critical flutter free flow static pressure
pm, po, pt	Number of shape functions used from the g, f and h sets of shape functions
R	Shell's middle surface radius
r_ψ	Fiber path turning radius
SF	General shape function notation
t	Time variable
u, v, w	Shell's membrane displacement the x, θ and z coordinates
u_0, v_0, w_0	Shell's mid surface displacement along the x, θ and z coordinates
v_{12}, v_{13}, v_{23}	Poisson's ratio in the material's coordinate system
x, θ, z	Polar coordinate system variables
ε_1, ε_2, ε_3	Normal strain in the material's coordinate system
ε_{12}	In-plane shear strain in the material's coordinate system
ε_{13}, ε_{23}	Transverse shear strains in the material's coordinate system
ε_{xx}, $\varepsilon_{\theta\theta}$	Normal strains in the polar coordinate system
ε^0_{xx}, $\varepsilon^0_{\theta\theta}$	Normal strains of the shell's middle surface in the polar coordinate system
γ	Air's specific heat ration
$\gamma_{x\theta}$, γ_{xz}, $\gamma_{\theta z}$	Shear strains in the polar coordinate system
$\gamma^0_{x\theta}$, γ^0_{xz}, $\gamma^0_{\theta z}$	Shell's middle surface shear strains in the polar coordinate system

ψ	Fiber ply angle
ρ	Material volumetric mass
ρ_{fluid}	Fluid volumetric mass
σ_1, σ_2, σ_3	Normal stresses in the material's coordinate system
σ_{12}, σ_{13}, σ_{23}	Transverse shear stresses in the material's coordinate system
σ_{xx}, $\sigma_{\theta\theta}$, $\sigma_{x\theta}$	Normal stresses in the polar coordinate system
$\sigma_{x\theta}$, σ_{xz}, $\sigma_{\theta z}$	Shear stresses in the polar coordinate system
ξ	Adimensional variable of the axial distance
ω_i	Natural Frequency i
Ω	Eigenvalue
$\mathbf{K}$	Stiffness matrix
$\mathbf{N}$	Shape function matrix
$\mathbf{M}$	Mass matrix
$\mathbf{Q}$	Elastic matrix in the material's coordinate system
$\overline{\mathbf{Q}}$	Elastic matrix in the polar coordinate system
$\boldsymbol{\delta_1}$, $\boldsymbol{\delta_2}$,$\boldsymbol{\delta_3}$	Shape function vectors for u_0, v_0 and w_0 displacements
$\mathbf{p}$	External pressure vector
$\mathbf{q}$	Coefficient vector for p-FEM
$\mathbf{q_t}$	Generalized coordinates
2D	Two dimensional
3D	Three dimensional
AFP	Automated fibre placement
ATL	Automated tape laying
CSCL	Constant stiffness composite laminate
CTS	Continuous tow shearing
FEM	Finite element method
h-FEM	h-Version finite element method
HFEM	Hierarchical finite element method
p-FEM	p-Version finite element method
TFP	Tailored fibre placement
VSCL	Variable stiffness composite laminate

Chapter 1

Introduction

1.1 Overview and Motivation

An investigation of the aeroelastic flutter phenomenon caused by the axial flow of air at a supersonic speed around a variable stiffness composite laminate closed thin cylindrical shell is presented. Spacial variable stiffness along the axial direction of the cylindrical shell is achieved by the use of curvilinear fibers in the body's laminae.

Variable stiffness composite laminate shells (VSCL) are structures that allow for the design of lightweight structures with promising mechanical performance, as they allow for an increased level of design flexibility and tailoring towards the loads and conditions that the structure is expected to withstand. Therefore, the study and development of the design and manufacturing techniques of this type of structure benefits the aeronautic and aerospace industries, where lightweight design is crucial.

In these industries, shell structures that enable a high ratio between stiffness and weight are commonly used, for example, in plane and rocket fuselages, and, therefore, the implementation of VSCL and the study of how they react to harsh airflow conditions is increasingly relevant as the threshold of speed achieved by aircraft is constantly being challenged. Thus, the study of flutter is important, as this phenomenon is an aeroelastic instability that might result in the catastrophic failure of the structure. Considering this, the question arises: can the implementation of variable stiffness properties on composite laminate shells improve the mechanical performance against aeroelastic flutter? This dissertation has the goal of answering that question.

1.2 Introduction of Concepts

This section familiarizes the reader with concepts, whose understanding is needed for this study. This includes fiber reinforced composites, the variable stiffness concept and aeroelastic flutter. These concepts are alluded to during the study and understanding them also provides the idea of the motivation behind this study.

1.2.1 Fiber Reinforced Composite Laminate Shells

Fiber reinforced composite materials are widely used in practical engineering applications, as they are efficient structures with the capability of being tailored to the structure's expected loads.

These materials are composed by various fibers embedded in a matrix material. The fibers act to support the loads of the structure, while the matrix agglomerates the fibers and ensures material continuity, enabling stress transfer between the fibers. Fiber can be distributed in different forms: the fibers can be woven, either as a fabric in a 2-dimensional plane or in a 3-dimensional body; the fibers can be randomly distributed in a mould in short segments; they can be wound continuously around a mandrel; or the fibers can be laid down in tape form (this is known as a tow), forming sheets called plies that can be layered. The latter are the subject of this study and are referred to as composite laminates [1].

The mechanical performance of structures with these materials is highly dependent on the fiber orientation of each layer. This is because each fiber supports maximum strength on the direction of the fiber, while it has less resistance to loads on the two perpendicular directions. Therefore, these materials are considered to be orthotropic, which is a characteristic that on one hand makes the structures more complex to analyse and manufacture, but on the other presents more layers of freedom on its functional design, as it allows to tailor each layer's fibers to support the expected loads. Additionally, each layer of the laminate structure may have its own fiber orientation, which permits the mechanical properties of the laminate to be controlled by combining different ply orientations and by choosing the total number of plies. These materials typically present high specific strength and specific stiffness, resulting in lightweight structures, which is functionally, economically and environmentally beneficial in a lot of contexts [1].

Shells are widely used structures in engineering that, by nature, also allow for lightweight design, due to their high specific strength and stiffness. So, fiber reinforced composite laminate shells are extremely appealing structures for industries such as the aerospace industry and for renewable energy technologies, in which reduction of structure weight is vital for the reduction of CO_2 emissions [2].

1.2.2 Variable Stiffness Composite Laminates

Traditional fiber reinforced composite laminates have permitted the increase of freedom on structural design by allowing the adjustment of the elastic properties of a laminate throughout its thickness. However, this concept can be taken further with variable stiffness composite laminates.

By implementing curvilinear fibers, as opposed to the traditional unidirectional fibers, it is possible to control the fibers' angle on each ply in each spacial point of the structure, maximizing the design possibilities and taking full advantage of the mechanical properties of this kind of material, improving its performance without an increase in thickness and, consequently, weight. The control of the fibers' path enables a redistribution of an applied load to a more favorable loading condition in the critical regions of the structure [1].

Therefore, the implementation of curved fiber paths in fiber reinforced composite laminates are recognized as a promising technique, and are gaining increasing relevance in several applications.

A representation of a generic constant stiffness laminae and of a generic variable stiffness laminae can be seen in Figure 1.1, where a cylindrical coordinate system is used.

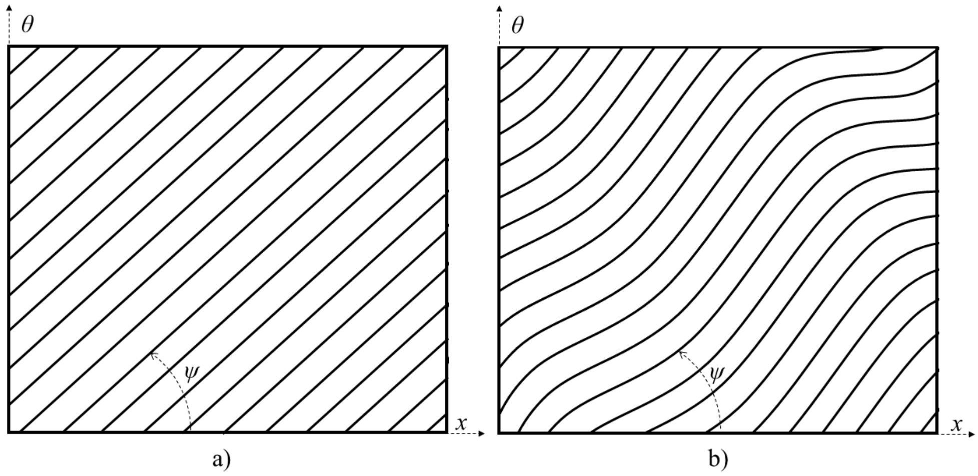

Figure 1.1: Tow angle ψ representation of a lamina in a: a) constant stiffness case; b) variable stiffness case.

1.2.2.1 Production

VSCL have been receiving a lot of attention due to their enhanced design flexibility and so, many great efforts have been made in the last years towards the development of technologies to enable and perfect the manufacturing processes of said laminates.

Originally, fiber-reinforced composite laminates were made by hand, which made it uncommon to use tow angles other than 0º, 90º and ±45º. The appearance of automated production systems made it possible to achieve other fiber orientations and manufacture parts with high quality and larger and more complex geometries [1].

However, the idea of having fiber-reinforced composite laminate structures with a continuously varied tow angle only existed in theory for a long time. Advanced fiber placement processes made it possible to manufacture these laminates. These processes are possible due to machines that typically have seven axes of motion and are controlled by a computer. There are 3 axes dedicated to position of the material deposition head, 3 axes to control its rotation and an axis to control the rotation of the mandrel. Commonly, in the aerospace industry, carbon fibers pre-impregnated with thermoset resin are used. Each tow comes from a reel and is directed by rollers to the deposition site. The tow is heated and then compressed by a compaction roller, which enables the tow to adhere to the desired surface and removes trapped air. This enables the deposition of curvilinear fibers [1, 3].

A schematic of an advanced fiber placement machine head is represented in Figure 1.2.

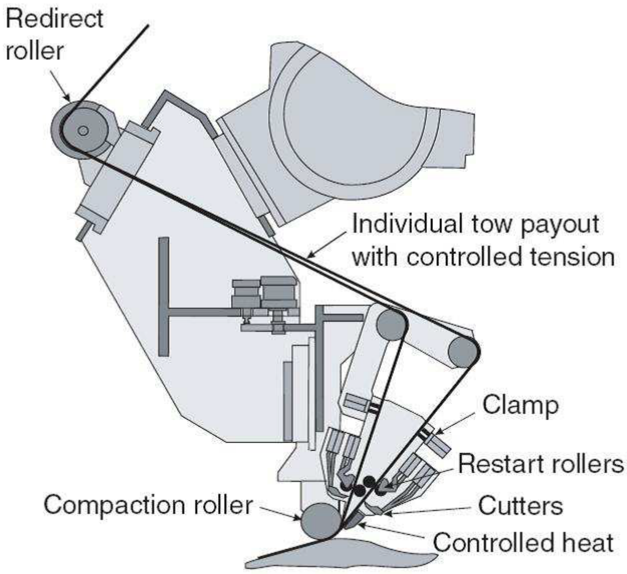

Figure 1.2: Schematic view of an advanced fiber placement machine head (reprinted with permission from Evans [3]).

From the advanced fiber placement process, other techniques were developed. The most commonly used to manufacture VSCL are automated tape laying (ATL), automated fiber placement (AFP), continuous tow shearing (CTS), and tailored fiber placement (TFP) [2].

ATL is a robot-assisted process where pre-impregnated wide tapes are deposited on the surface of a mould using a material deposition head, while automatically removing the ply backing. This process is commonly used for the manufacturing of relatively large components with low curvature.

AFP (also known as automated tow placement) is similar to ATL, but uses a material deposition head to simultaneously deliver a high number (up to 32) of narrow pre-impregnated slices, with a width between 3.175 mm and 12.7 mm. This is a comparatively mature process that creates high-quality structures and presents high potential for future enhancements.

In general, for constant course width tows, adjacent edges of two steered paths do not match, unless the courses are exactly parallel. This results in either gaps or overlaps. A visual representation of these defects may be seen in Figure 1.3, where the dashed lines represents the center-lines of each tow path. Both ATL and AFP processes may originate structures with these imperfections, as well as other flaws, such as local fiber wrinkling.

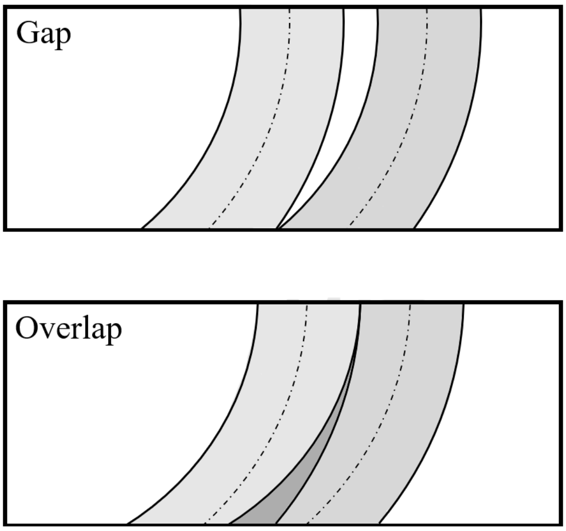

Figure 1.3: Gap and overlap representation of two adjacent tow paths.

The **CTS** technique was developed to tackle these problems by relying on in-plane shear deformation of partially impregnated tow materials, allowing to change the width along a tow. The shear effort is applied by fixing the deposition head rotation as a strip of tow material is placed, and the process simultaneously employs an in-situ impregnation. This mechanism can avoid tows and overlaps by allowing a change in thickness, controlled by the shearing angel, therefore simplifying the modelling and design of the structure, as well as delivering VSCL with high quality. It is however noteworthy that this process is still immature, in comparison with ATL and AFP.

TFP (also known as dry tow placement) is a highly productive process that allows to deposit the fiber roving with a radii of curvature lower than 5 mm. It is an embroidery-based preform manufacturing process with appealing designing freedom on the tow paths. Excellent out-of-plane mechanical performance can be achieved with this process, however, some defects, such as out-of-plane buckling of the tows or resin gaps may appear, due to the process setup characteristics, and a slight overlap is commonly desired to create continuous VSCL with no gaps [2].

Despite the latest efforts on the development of these techniques, there are manufacturability constraints that present crucial limiting factors that cannot be ignored in the modeling and design of VSCL structures. These limitations exist not only to avoid material defects, as well as to present realistic and manufacturable fiber paths, and must be understood by the designer to guarantee the manufacturability and the quality of the produced structure.

For instance, a minimum turning radius of the fiber path exists to avoid out-of-plane tow buckling on the inside of highly curved tows under compressive force and, similarly, tow pull-up on the outside of similar tows under tensile stresses.

The minimum cut length refers to the tow length that should also be respected to ensure that it is possible to lay a tow in a controlled manner, avoiding tow misalignment and, consequently, undesired tow gaps and overlaps. This is relevant, as each tow can be individually cut and restarted, as to reduce scrap rates and control the course width, which is useful to avoid gaps and overlaps.

A lamina where this cut technique is applied is represented in Figure 1.4. The amount of tow cut can be manipulated as to control how the tow path interacts with a given boundary, like an adjacent tow path. A coverage parameter of 0% means that, in a given boundary, the tow is cut as soon as it makes contact with the adjacent edge, which results in a zone with gaps, but no overlaps. On the other hand, a coverage parameter of 100% results in zones with overlaps, but does not allow the existence of gaps. Figure 1.4 schematically represents tow cuts in both of these cases. Intermediate percentages of the coverage parameter can also exist [1, 2].

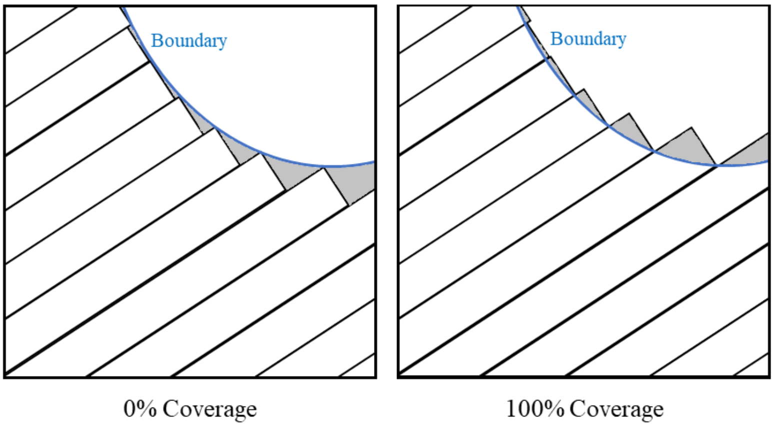

Figure 1.4: Lamina with 0% and 100% coverage.

This dissertation focuses on a theoretical analysis where these geometric imperfections are not modelled, which nonetheless enables to understand the potential mechanical properties that can be achieved with VSCL shells as the manufacturing processes are perfected and as structures with better quality are achieved. However, an effort on the development of realistic tow paths is made, and the minimum turning radius constraint is considered in the results.

1.2.2.2 Curvilinear Fiber Path Definitions

In this section, various fiber paths for VSCL are defined resorting to mathematical expressions, as well as the fiber paths for the constant stiffness cases.

Each fiber path can be defined by its tow angle ψ, which is the in-plane angle between the fiber orientation and the axial direction of the cylinder, as it can be seen for a generic constant stiffness composite laminate (CSCL) and VSCL in Figure 1.1 a) and 1.1 b) respectively, where a planar representation of a cylindrical lamina is made along the axial coordinate x and the angle coordinate θ.

Fiber paths may be obtained by using 2 different strategies: the shifted fiber method and the parallel fiber method. The shifted fiber method considers that each path has the same shape, but that it is shifted in the perpendicular direction to the stiffness variation, which in the case of the studied cylindrical shells is the tangential direction to the cross section. This method allows for a simple mathematical expression to define the tow angle of the fibers, and, since stiffness is only variable along the axial direction, this allows for a less computationally expensive model. However, these paths produce tow coursed that are not exactly parallel. Unparallel adjacent courses with constant width result in overlaps or gaps, depending on the shift distance. Meanwhile, the parallel fiber method consists on laying each fiber with parallel baselines, so that these imperfections are avoided. For this case, a numerical procedure must be implemented to determine each path and the mathematical modeling approach becomes more complex. This also produces variable stiffness along both the axial and the angular directions of the shell [4].

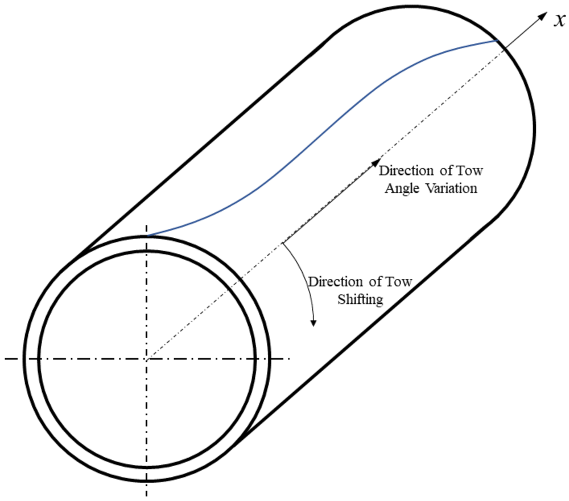

Figure 1.5: Cylinder with a representation of a generic tow path and the angle variation and shifting directions.

Considering this, this study focuses on fiber paths obtained using the shifted fiber method, with only axial tow angle variations considered, as the shifting direction is the circumferential one, as seen in Figure 1.5. Common tow path examples found in the literature are used: linear variation of the fiber orientation, constant in-plane curvature and constant angle path [1, 2]. The geodesic path is also quite common, however, it is not reviewed in this study since it is most relevant for cylinders with varying radius, as for cylindrical shells with constant radius its path is equal to the constant angle path.

Each path is defined using mathematical expressions for the tow angle ψ along the axial adimensional variable ξ, which varies between -1 and 1. T_0 represents the tow angle at $\xi = -1$ and T_1 represents the tow angle at $\xi = 1$, unless stated otherwise.

Linear variations of fiber orientation are widely used and present a concise formulation, as seen in equation 1.1. To refer to this setup, the notation $<T_0,T_1>$ is used.

$$\psi(\xi) = (T_1 - T_0) \cdot \frac{\xi + 1}{2} + T_0 \tag{1.1}$$

Similarly, a **linear variation of fiber orientation** with **two segments** may be employed using expression 1.2, where, in this case, T_0 represents the tow angle at $\xi = 0$ and T_1 represents the tow angle at $\xi = -1$ and at $\xi = 1$. The tow paths can be divided in segments as many times as it is desired, as long as fiber path continuity is ensured. However, in this dissertation, a maximum number of 2 segments is set. The used notation for this type of path is $<T_1,T_0,T_1>$.

$$\psi(\xi) = (T_1 - T_0) \cdot |\xi| + T_0 \tag{1.2}$$

With the intent of producing manufacturable paths, a minimum turning radius of the tow course must be respected as to avoid defects promoted by in-plane bending deformations, such as local buckling and wrinkling of the inner edges of the fibers, which can cause a decline in mechanical properties. To find the turning radius r_ψ of linear angle variation paths, an analytical procedure is done. At any point of the structure, equation 1.3 can be used to calculate it , where $f(x)$ is the function that defines the fiber path along the axial coordinate x that varies between 0 and l, and l corresponds to the axial length of the cylindrical shell [5]. $f(x)$ can be calculated for a given fiber path with the expression 1.4

$$r_\psi(x) = \frac{\left(1 + \left(\frac{\partial f(x)}{\partial x}\right)^2\right)^{3/2}}{|\frac{\partial^2 f(x)}{\partial^2 x}|} \tag{1.3}$$

$$f(x) = \int tan(\psi(x))dx \tag{1.4}$$

The **constant in-plane curvature** path is based on circular arcs and its use is convenient, since it allows to calculate its turning radius in a straightforward manner. The curvature of a tow path is mathematically defined as the inverse of the turning radius. For these paths, the turning radius r_ψ is constant and equation 1.3 can be simplified into equation 1.5. The mathematical expression that describes the angle variation of the fibers along the path is equation 1.6. To refer to this type of path, the notation $<T_0,T_1>_c$ is used.

$$r_\psi = \frac{l}{|sin(T_1) - sin(T_0)|} \tag{1.5}$$

$$\psi(\xi) = arcsin\left[sin(T_0) + [sin(T_1) - sin(T_0)] \cdot \frac{\xi + 1}{2}\right] \tag{1.6}$$

Similarly to what has been done before, a **constant in-plane curvature tow path** with **two segments** may be considered, as it is expressed in equation 1.7, where T_0 represents the tow angle at $\xi = 0$ and T_1 represents the tow angle at $\xi = -1$ and at $\xi = 1$. This type of path is referred to in this document with the notation $<T_1,T_0,T_1>_c$.

$$\psi(\xi) = arcsin\left[sin(T_0) + [sin(T_1) - sin(T_0)] \cdot |\xi|\right] \tag{1.7}$$

For this case, the turning radius is obtained recurring to expression 1.8.

$$r_\psi = \frac{0.5 \cdot l}{|sin(T_1) - sin(T_0)|} \tag{1.8}$$

Lastly, the **constant angle path** corresponds to CSCL shells, and its tow angle is constant throughout the cylinder, as $\psi = T_0$.

A representation of each described curvilinear fiber path can be seen in Figure 1.6.

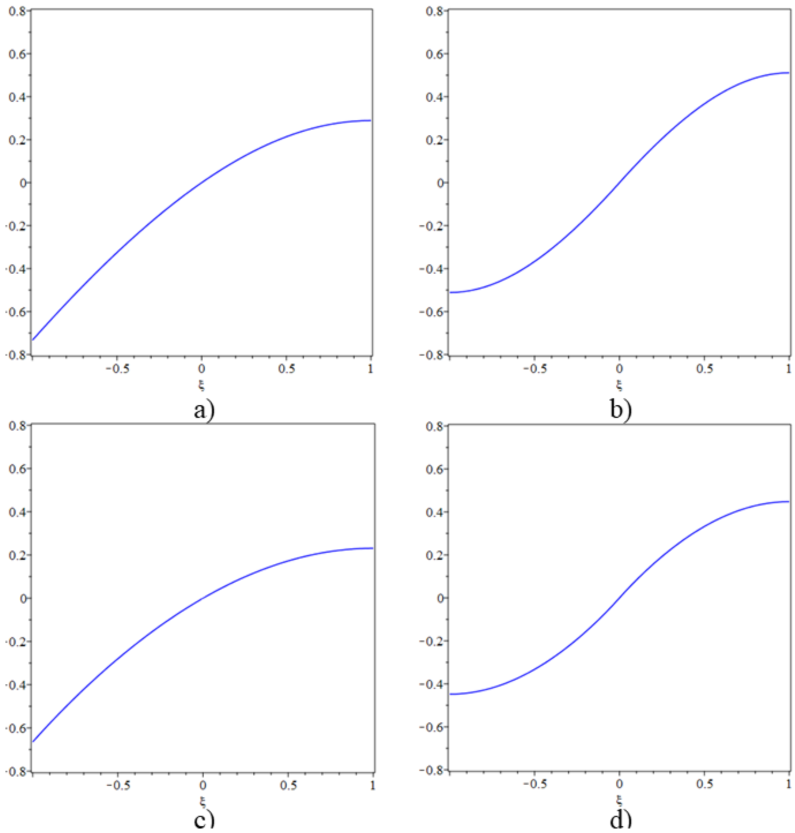

Figure 1.6: Tow path representation for a) linear variation of fiber orientation, b) linear variation of fiber orientation with two segments, c) constant in-plane curvature, d) constant in-plane curvature with two segments ($T_0 = 70^{o}$, $T_1 = 0^{o}$).

It is relevant to add that, in reality, any of these paths presents geometric irregularities due to manufacturing imperfections, such as gaps and overlaps, as well as tow angle discontinuities between tow courses, due to the fact that each tow path is deposited with a set path width determined by the parameters of the material deposition head. In this study, these paths are considered to be ideal, which can lead to some discrepancies with reality.

1.2.3 Supersonic Flutter

Aeroelasticity is a branch in physics that studies phenomena which involve significant mutual interactions among inertial, elastic and aerodynamic forces [6].

Among these phenomena, one of the most dramatic is flutter. It consists on a dynamic instability which may result in catastrophic structural failure. As a structure is subjected to an external flow of fluid, it vibrates. When flutter occurs, the amplitude of these vibrations starts to increase as time passes. For this to happen, a critical set of flow conditions must be achieved and so, this phenomena is specially relevant in industries where structures are subjected to severe flow conditions, like high speeds and aerodynamic pressures, as it happens on the aerospace industry. Therefore, these structures must be designed ensuring that the flutter does not occur at the expected operating conditions.

Flutter is a phenomena that is best understood recurring to a mathematical explanation, so, a deeper review of this subject can be read in section 2.10. This dissertation focuses on understanding if VSCL structures can be tailored so that they can withstand harsher conditions than classic composite laminate structures without flutter occurring. Supersonic conditions are always considered.

1.3 Literature Review

Variable stiffness composite laminates introduce challenges in the design and optimization of these structures, which increase the model's complexity and required computational efforts. However, as this type of material presents promising properties, various authors have addressed this concept in an effort to further theoretically understand it, as well as to minimize its challenges that arise in practical scenarios, mainly the consequent limitations from its manufacturing processes and structural defects that may arise. The goal of this section is to review some of the work that proved useful for the development of this dissertation and that might be relevant to the reader that wishes to obtain more information about some of the topics of this work.

References [7–10] present books with great knowledge about the dynamic behaviour of plates and shells. Kaw [11] has a book focused on the mechanical analysis of composite materials. Petyt [12] has a book about the finite element method used in vibration analysis. These books were useful to understand the foundations that lead to the development of the mathematical model of this dissertation.

References [13–28] present different analyses on the dynamic behaviour of both plates and shells under different conditions.

Aragh et. al [2] and Lozano et. al [29] present State-of-the-Art articles on the manufacturing aspects of VSCL. Heinecke & Willberg [30] review common manufacturing-induced imperfections in composite parts manufactured via automated fiber placement.

Tatting [4] presents an analysis of VSCL cylindrical shells, focused on the effect of the Brazier effect on such structures. Blom [1] presents a study on the optimization of the fundamental frequency and buckling response on VSCL cylinders and modelled the effect of gaps and overlaps, and Fayazbakhsh et. al [31] introduced a method that allows to model these manufacturing defects with a less refined mesh. Blom et. al [32] also presents a theoretical model to study the influence of tow-drop areas on the stiffness and strength of VSCL. Labans & Bisagni [33] did both numerical and experimental tests on the buckling and free vibration of VSCL shells and Rouhi et. al [34] also manufactured a VSCL cylindrical shell and tested it experimentally for buckling conditions. Wu et. al [35] did an optimization work of VSCL plates for buckling behaviour. Waldhart [5] studied the response of VSCL to uni-axial compression and shear deformation and compared the response of laminates with parallel and shifted fiber paths. Tian et. al [36] optimized VSCL with gap-overlap and curvature constraints.

Carvalho et. al [37] did a study on VSCL with manufacturing defects focused on fundamental frequency optimization. Fayazbakhsh [38] studies the effect of manufacturing induced defects on composite laminates with optimized curvilinear fiber paths. Marouene et. al [39] did an optimization work on the buckling behaviour of VSCL structures with the effects of gaps and overlaps taken into account. Blom [40] also did an optimization of VSCL structures with the intent of minimizing ply thickness buildup and maximizing surface smoothness. Nik [41] also did an optimization work of VSCL structures where manufacturing induced defects were considered. Wu et. al [42] does a structural assessment of VSCL shells resorting to experimental and analytical methods. Khani et. al [43] optimized the strength of VSCL plates. Falcó et. al [44] modeled VSCL plates considering manufacturing defects and their influence on the failure behavior. Cairns et. al [45] studied the effect of stress concentration on tow placed laminates. Dang et. al [46] studied the impact behaviour on VSCL. Pan et. al [47] and Wu et. al [48, 49] studied the design of VSCL shells regarding the manufacturing aspects of the process. Lopes [50] studied the damage and failure of VSCL structures.

Ribeiro [51] studied the modes of vibration of VSCL open cylindrical shells. Akhavan [52] studied the non linear vibrations of VSCL structures. Antunes et. al [53] did a modal analysis of a variable stiffness composite laminated plate with diverse boundary conditions under theoretical and experimental conditions. Rodrigues et. al [54] also did an experimental modal analysis on a VSCL plate and compared the results to a FEM analysis.

Regarding aeroelasticity, Dowell et. al [6] has published a book with vast knowledge on this branch of physics. Sabri & Lakis [55], Bismarck [56], Olson [57], Carter & Stearman [58], Ganapathi et. al [59] and Evensen & Olson [60] studied the dynamic effect of aeroelastic supersonic flutter on isotropic cylindrical shells. Amabili & Pellicano [61] also studied it, but included the effect of imperfections of the geometry of the cylindrical shells. Chen & Li [62] studied the same effect, but on composite laminate cylindrical shells. Furthermore, Avramov [63] studied the vibrations of composite cylindrical shells under supersonic flow and Brower [64] studied aeroelastic instabilities of thin panels under turbulent flow. Camacho [65, 66] did studies on the aeroelastic behaviour of hybrid composite laminates with carbon nanotubes and curvilinear fibers.

Akhavan & Ribeiro [67–69] studied the effect of supersonic flutter on the dynamic response of VSCL, and this dissertation intends on further developing the knowledge on this topic. The combined effect of aeroelastic supersonic flutter on variable stiffness composite laminate cylindrical shells has not yet been studied, and, given the interest of VSCL on the aerospace and aeronautic industries, this dissertation focuses on further understanding this subject.

1.4 Objectives

The main goal of the present work is to understand how curvilinear fiber paths on composite laminate shells affect the performance under axial flow of air at supersonic flows. The goal is to improve mechanical performance of the structure against flutter. This goal is achieved by completing the following tasks:

- Development of a linear mathematical model for a VSCL cylindrical shell based on the Love's first approximation assumptions;
- Modeling of the aerodynamic forces applied to the cylindrical shell recurring to the linearized piston theory;
- Implementation of the developed mathematical model on the software *Maple* through the p-version of the finite element method;
- Convergence test and validation of the developed finite element matrices by comparing natural frequency results with others found in the literature;
- Validation of the implementation of the flutter phenomenon by comparing the critical free stream static pressure with other examples found in the literature for circular cylindrical shells;
- Study of the relation between fiber paths and critical conditions for the occurrence of aeroelastic supersonic flutter.

1.5 Layout

This dissertation is structured in 5 chapters, that are described as:

- **Chapter 1: Introduction** - This chapter is the present introduction, where the goals and motivation for this dissertation are explained. A literature review is also present as a means of allowing the reader to better understand the topics and concepts addressed in this work, as well as a bibliography review to familiarize the reader with other authors' work that further explore topics of this dissertation.

- **Chapter 2: Mathematical Model** - In this chapter, a mathematical formulation of the model is presented. The equations of motion for a thin circular cylindrical shell are established based on the Love's first approximation assumptions. The linear model is then implemented using the software *Maple* recurring to a p-version finite element method, which is also described. The aerodynamic forces created by the axial flow of air at supersonic speeds are modelled using the linear piston theory, so then the calculation of the critical free stream pressure for the occurrence of flutter can be made.

- **Chapter 3: Model Validation** - In this chapter, the developed model is tested with the goal of validating it. Firstly, a convergence test is made to understand the required number of shape functions necessary for the results to converge. Then, the natural frequencies of circular cylindrical shells with constant stiffness, both for clamped and simply supported edges, are calculated and compared with results found in literature. Lastly, the critical free stream pressure of the supersonic axial flow for the occurrence of flutter is calculated and is also compared with those found in other works. The obtained eigenvalues and eigenvectors by the solution of the flutter problem are then analyzed.

- **Chapter 4: Supersonic Flutter on Variable Stiffness Composite Laminate Cylindrical Shells** - In this chapter, the developed mathematical model is used to find fiber paths that can increase the value of critical free stream static pressure at which flutter occurs for a given cylindrical shell with clamped edges. The obtained flutter modes are analyzed. Then, the effect of the change of boundary conditions on the flutter modes and on the critical pressure values is studied.

- **Chapter 5: Conclusions and Future Work** - Finally, in this chapter, the developed work for this dissertation is summarized and the drawn conclusions from the convergence tests, the model validation and the flutter tests on VSCL shells are reviewed. Lastly, suggestions are made for future works that can deepen the knowledge about the topics addressed in this dissertation.

Chapter 2

Mathematical Model

2.1 Introduction

In this chapter, a formulation for a mathematical model of a variable stiffness composite laminate circular cylindrical shell under an axial supersonic airflow is described. This model is implemented using the p-version of the finite element method to first study the natural frequencies and modes of vibration of said structure, and then the piston theory is used to model the supersonic axial airflow, so the critical conditions at which flutter occurs can be calculated. This is a linear model, implemented for thin cylindrical shells. It has the versatility of approximating various levels of design complexity, from isotropic cases (like steel shells, for example) to variable stiffness composite laminates (which are the goal of this study). Only axial variation of stiffness is considered and the used fiber paths are described in section 1.2.2.2, as each path is shifted along the θ direction. The effects of manufacturing defects, such as gaps and overlaps, and of fiber path imperfections are not considered.

Shells are three dimensional (3D) objects confined by two relatively close curved surfaces. In general, the distance between those two surfaces - the thickness - is small when compared to its other dimensions, like length, width and radii of curvature. The implementation of the 3D equations of elasticity is complex, however, shell theories are able to reduce this problem to a two dimensional one by developing theories that do not consider the coordinate normal to the shell as a variable. This is a highly advantageous approach, as it allows for a less complex and less computationally heavy model to be implemented, while still approximately respecting the 3D theory of elasticity.

Shells may have different geometrical shapes based on their curvature characteristics, and as such, a cylinder can be thought as a specific case of a shell. It is a solid of revolution, or, in other words, its surfaces are constructed by defining a line and revolving it around its central axis. In the case of cylinders, a circular cross section is produced.

A closed circular cylindrical shell is considered for this analysis. Its two confining surfaces are parallel and, therefore, its thickness is constant. The middle surface of the shell resides between and parallel to the inner and outer surfaces, at an equal distance from both. The radius of the

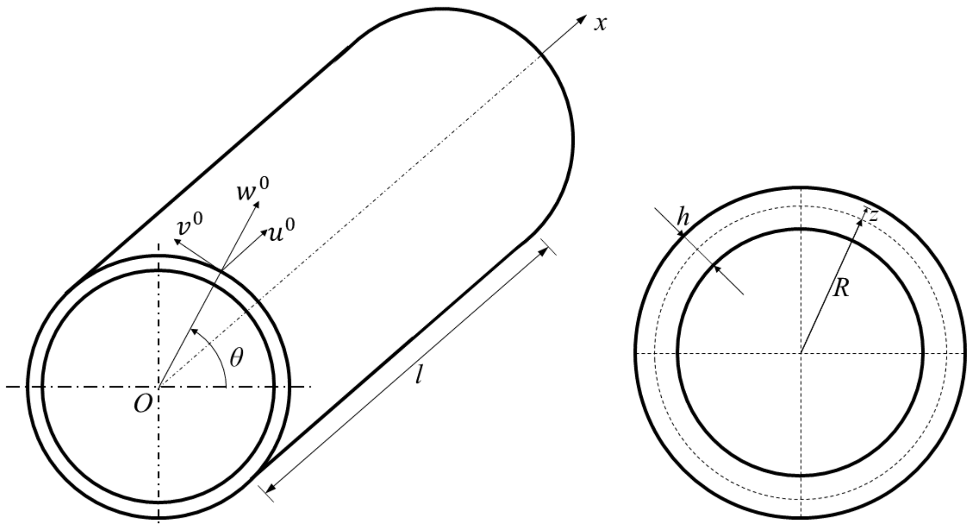

Figure 2.1: Cylindrical shell relevant dimensions and coordinate system (3D view and cross sectional view).

cylinder R is described as the distance from the geometrical center of the profile of the cylinder to the middle surface, which is considered constant along the axial direction. Other relevant measures of the body are its axial length l and the shells thickness h.

Considering this, it is advantageous to use a cylindrical coordinate system, where x is the axial coordinate, θ is the angle coordinate and z is the distance from the middle surface to a given shell point along the radial direction [10].

Figure 2.1 represents the described dimensions, as well as the used coordinate system.

2.2 Love's First Approximation

There are some key assumptions that are the foundation of the whole mathematical model. Love's first approximation hypotheses [7] are considered so that a thin shell linear elastic model can be obtained:

1. The thickness of the shell is small compared to the other dimensions of the shell, like the radius of curvature of the middle surface.

2. Stresses in the normal direction to the middle surface are negligible when compared to the stresses in other directions.

3. Strains and displacements are sufficiently small so that the quantities of second and higher order terms in the strain-displacement are neglectable, when compared to the first order terms.

4. Normals to the middle surface at any point remain straight and normal to the mid surface after shell deformation and suffer no extension.

The first hypothesis allows for the convenient neglection of terms like $\frac{h}{R}$ in the derivation of the shell theory, as they are much lower than the other terms in these expressions. A widely used criteria to consider a shell as a thin shell is that $\frac{h}{R} \leq 1/20$ [9].

The second assumption leads to the consideration that $\sigma_{zz} = 0$.

The third hypothesis allows for a linear analysis of the shell.

Lastly, the fourth assumption is known as Kirchhoff's hypothesis, and has the geometric implication that:

$$\begin{cases} \gamma_{xz} = 0 \\ \gamma_{\theta z} = 0 \\ \varepsilon_{zz} = 0 \end{cases} \quad \text{and, therefore} \quad \begin{cases} \sigma_{xz} = 0 \\ \sigma_{\theta z} = 0 \end{cases} \tag{2.1}$$

In order to satisfy Kirchhoff's hypothesis, the displacement field is bound by the linear relationship stated in equation 2.2. In these equations, u, v, w refer to the displacements components in the x, θ and z direction, respectively, and u_0, v_0, w_0 refer to the displacement components of the shell's middle surface [7].

$$u(x,\theta,z,) = u_0(x,\theta) + z\frac{\partial u(x,\theta)}{\partial z} \tag{2.2a}$$
$$v(x,\theta,z) = v_0(x,\theta) + z\frac{\partial v(x,\theta)}{\partial z} \tag{2.2b}$$
$$w(x,\theta,z) = w_0(x,\theta) \tag{2.2c}$$

2.3 Kinematic Relations

Love's first approximation allows for the elasticity problem to be reduced from a 3D to a 2D problem, where the strains in each point of the body can be expressed as a function of the strain on the mid surface, as follows [7].

$$\varepsilon_{xx}(x,\theta,z) = \varepsilon_{xx}^0(x,\theta) + z \cdot k_{xx}(x,\theta) \tag{2.3a}$$
$$\varepsilon_{\theta\theta}(x,\theta,z) = \varepsilon_{\theta\theta}^0(x,\theta) + z \cdot k_{\theta\theta}(x,\theta) \tag{2.3b}$$
$$\gamma_{x\theta}(x,\theta,z) = \gamma_{x\theta}^0(x,\theta) + z \cdot k_{x\theta}(x,\theta) \tag{2.3c}$$

Equations 2.3 are commonly referred to as the equations of Love and Timoshenko [7]. The terms ε_{xx}^0, ε_{θ}^0, $\gamma_{x\theta}^0$ refer to the strains at the middle surface, k_{xx}, $k_{\theta\theta}$ refer to the changes in curvature and $k_{x\theta}$ to the twist. Choosing to make this simplification enables the derivation of the equations 2.4, which are valid for the specific case of a closed cylinder in cylindrical coordinates [10, 24].

$$\varepsilon_{xx}^{0} = \frac{\partial u_0}{\partial x} \tag{2.4a}$$

$$\varepsilon_{\theta\theta}^{0} = \frac{1}{R}\frac{\partial v_0}{\partial \theta} + \frac{w_0}{R} \tag{2.4b}$$

$$\gamma_{x\theta}^{0} = \frac{1}{R}\frac{\partial u_0}{\partial \theta} + \frac{\partial v_0}{\partial x} \tag{2.4c}$$

$$k_{xx} = -\frac{\partial^2 w_0}{\partial x^2} \tag{2.4d}$$

$$k_{\theta\theta} = \frac{1}{R^2}\frac{\partial v_0}{\partial \theta} - \frac{1}{R^2}\frac{\partial^2 w_0}{\partial \theta^2} \tag{2.4e}$$

$$k_{x\theta} = \frac{1}{R}\frac{\partial v_0}{\partial x} - \frac{2}{R}\frac{\partial^2 w_0}{\partial x \partial \theta} \tag{2.4f}$$

These equations are needed to arrive at the equations of motion which describe the dynamic behaviour of the shell.

2.4 Fundamental Equations of Elasticity

A constitutive model that describes how the elastic properties and the lamination parameters of the material relate to the inner stresses of the structure and its strains is described in this section. A first constitutive model is explained for the general case of a composite laminated shell, then a simplification is made for the case of a thin shell, where Love's first approximation hypotheses, described in section 2.2, are applied.

Regarding the laminae, the following assumptions are made:

1. The fibers are parallel to the inner and outer surfaces of the shell.
2. The fiber path angle remains constant throughout a layer's thickness.
3. Each layer of the shell is regarded as homogeneous along its thickness and orthotropic.

As a consequence of the third assumption, it is considered that the volumetric mass of the laminate is constant.

A composite laminated shell is composed by several layers, each one with its own fiber orientation. Constant stiffness composite laminates maintain a constant tow angle ψ, whereas variable stiffness composite laminates have tow angle variation along the spacial coordinates, as can be seen for a generic example in Figure 1.1. The fiber paths used in this dissertation are defined in section 1.2.2.2, and are considered as ideal and without imperfections in this mathematical model.

For an orthotropic layer, the stress-strain relations can be made using the elastic matrix $\mathbf{Q}$, presented in equation 2.5. The 1, 2 and 3 subscripts refer to the directions of the material's coordinate system, in which the direction 1 is parallel to the fiber path and the 2 and 3 directions are the in-plane and out-of-plane perpendicular directions to the fiber path, respectively. Coefficients Q_{ij} are represented in expression 2.6 where E_{11}, E_{22} and E_{33} are the moduli of elasticity in the 1, 2 and 3 directions; G_{ij} and v_{ij} $(i,j = 1,2,3;\ i \neq j)$ are shear moduli and Poisson's ratios in the indices' directions, respectively.

$$\begin{Bmatrix} \sigma 1 \\ \sigma 2 \\ \sigma 3 \\ \sigma 23 \\ \sigma 13 \\ \sigma 12 \end{Bmatrix} = \begin{bmatrix} Q_{11} & Q_{12} & Q_{13} & 0 & 0 & 0 \\ Q_{12} & Q_{22} & Q_{23} & 0 & 0 & 0 \\ Q_{13} & Q_{23} & Q_{33} & 0 & 0 & 0 \\ 0 & 0 & 0 & Q_{44} & 0 & 0 \\ 0 & 0 & 0 & 0 & Q_{55} & 0 \\ 0 & 0 & 0 & 0 & 0 & Q_{66} \end{bmatrix} \begin{Bmatrix} \varepsilon 1 \\ \varepsilon 2 \\ \varepsilon 3 \\ \gamma 23 \\ \gamma 13 \\ \gamma 12 \end{Bmatrix} \tag{2.5}$$

$$Q_{11} = E_{11}\frac{1-\nu_{23}\nu_{32}}{\nu} \tag{2.6a}$$
$$Q_{22} = E_{22}\frac{1-\nu_{31}\nu_{13}}{\nu} \tag{2.6b}$$
$$Q_{33} = E_{33}\frac{1-\nu_{12}\nu_{21}}{\nu} \tag{2.6c}$$
$$Q_{44} = G_{23} \tag{2.6d}$$
$$Q_{55} = G_{13} \tag{2.6e}$$
$$Q_{66} = G_{12} \tag{2.6f}$$
$$Q_{12} = E_{11}\frac{\nu_{21}+\nu_{31}\nu_{23}}{\nu} = E_{22}\frac{\nu_{12}+\nu_{32}\nu_{13}}{\nu} \tag{2.6g}$$
$$Q_{13} = E_{11}\frac{\nu_{31}+\nu_{21}\nu_{32}}{\nu} = E_{22}\frac{\nu_{13}+\nu_{12}\nu_{23}}{\nu} \tag{2.6h}$$
$$Q_{23} = E_{22}\frac{\nu_{32}+\nu_{12}\nu_{31}}{\nu} = E_{33}\frac{\nu_{23}+\nu_{21}\nu_{13}}{\nu} \tag{2.6i}$$
$$\nu = 1-\nu_{12}\nu_{21}-\nu_{23}\nu_{32}-\nu_{31}\nu_{13}-2\nu_{21}\nu_{32}\nu_{13} \tag{2.6j}$$

However, the material's coordinate system usually does not coincide with the cylindrical coordinate system. As a consequence, a relation can be made between these two coordinate systems, as shown in equations 2.7 and 2.8, where $m = cos(\psi)$ and $n = sin(\psi)$ [8] [52] .

$$\begin{Bmatrix} \sigma_{xx} \\ \sigma_{\theta\theta} \\ \sigma_{zz} \\ \sigma_{\theta z} \\ \sigma_{xz} \\ \sigma_{x\theta} \end{Bmatrix} = \begin{bmatrix} m^2 & n^2 & 0 & 0 & 0 & -2\cdot m\cdot n \\ n^2 & m^2 & 0 & 0 & 0 & -2\cdot m\cdot n \\ 0 & 0 & 1 & 0 & 0 & 0 \\ 0 & 0 & 0 & m & n & 0 \\ 0 & 0 & 0 & -n & m & 0 \\ m\cdot n & -m\cdot n & 0 & 0 & 0 & m^2-n^2 \end{bmatrix} \begin{Bmatrix} \sigma_1 \\ \sigma_2 \\ \sigma_3 \\ \sigma_{23} \\ \sigma_{13} \\ \sigma_{12} \end{Bmatrix} \tag{2.7}$$

$$\begin{Bmatrix} \varepsilon_1 \\ \varepsilon_2 \\ \varepsilon_3 \\ \gamma_{23} \\ \gamma_{13} \\ \gamma_{12} \end{Bmatrix} = \begin{bmatrix} m^2 & n^2 & 0 & 0 & 0 & m \cdot n \\ n^2 & m^2 & 0 & 0 & 0 & -m \cdot n \\ 0 & 0 & 1 & 0 & 0 & 0 \\ 0 & 0 & 0 & m & -n & 0 \\ 0 & 0 & 0 & n & m & 0 \\ -2 \cdot m \cdot n & 2 \cdot m \cdot n & 0 & 0 & 0 & m^2 - n^2 \end{bmatrix} \begin{Bmatrix} \varepsilon_{xx} \\ \varepsilon_{\theta\theta} \\ \varepsilon_{zz} \\ \gamma_{\theta z} \\ \gamma_{xz} \\ \gamma x\theta \end{Bmatrix} \tag{2.8}$$

Using the transformation matrices above, expression 2.5 is used to obtain the elastic matrix in the cylindrical coordinate system $\overline{\mathbf{Q}}$, represented in equation 2.9. Notice that the terms $\overline{Q}_{16}$, $\overline{Q}_{26}$, $\overline{Q}_{36}$ and $\overline{Q}_{45}$ appear only thanks to the matrix transformation process.

$$\overline{\mathbf{Q}} = \begin{bmatrix} \overline{Q}_{11} & \overline{Q}_{12} & \overline{Q}_{13} & 0 & 0 & \overline{Q}_{16} \\ \overline{Q}_{12} & \overline{Q}_{22} & \overline{Q}_{23} & 0 & 0 & \overline{Q}_{26} \\ \overline{Q}_{13} & \overline{Q}_{23} & \overline{Q}_{33} & 0 & 0 & \overline{Q}_{36} \\ 0 & 0 & 0 & \overline{Q}_{44} & \overline{Q}_{45} & 0 \\ 0 & 0 & 0 & \overline{Q}_{45} & \overline{Q}_{55} & 0 \\ \overline{Q}_{16} & \overline{Q}_{26} & \overline{Q}_{36} & 0 & 0 & \overline{Q}_{66} \end{bmatrix} \tag{2.9}$$

Now, applying Love's first approximation to the model, some terms are neglected, according to what has been described in section 2.2. In light of this, the model is simplified and the elastic properties are described by equations 2.10 and 2.11, where coefficients $\overline{Q}_{ij}$ are described by equations 2.12.

$$\begin{Bmatrix} \sigma_1 \\ \sigma_2 \\ \sigma_{12} \end{Bmatrix} = \begin{bmatrix} Q_{11} & Q_{12} & 0 \\ Q_{12} & Q_{22} & 0 \\ 0 & 0 & Q_{66} \end{bmatrix} \begin{Bmatrix} \varepsilon_1 \\ \varepsilon_2 \\ \gamma_{12} \end{Bmatrix} \tag{2.10}$$

$$\begin{Bmatrix} \sigma_{xx} \\ \sigma_{\theta\theta} \\ \sigma_{x\theta} \end{Bmatrix} = \begin{bmatrix} \overline{Q}_{11} & \overline{Q}_{12} & \overline{Q}_{16} \\ \overline{Q}_{12} & \overline{Q}_{22} & \overline{Q}_{26} \\ \overline{Q}_{16} & \overline{Q}_{26} & \overline{Q}_{66} \end{bmatrix} \begin{Bmatrix} \varepsilon_{xx} \\ \varepsilon_{\theta\theta} \\ \gamma_{x\theta} \end{Bmatrix} \tag{2.11}$$

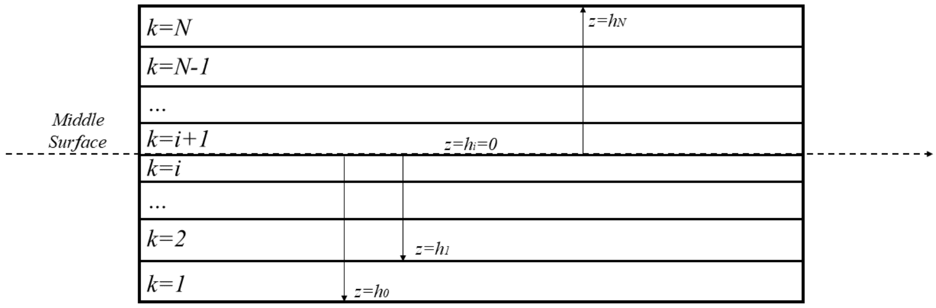

Figure 2.2: Laminae stacking sequence and nomenclature.

$$\overline{Q}_{11} = Q_{11}m^4 + 2(Q_{12} + 2Q_{66})m^2n^2 + Q_{22}n^4 \tag{2.12a}$$

$$\overline{Q}_{12} = (Q_{11} + Q_{22} - 4Q_{66})m^2n^2 + Q_{12}(m^4 + n^4) \tag{2.12b}$$

$$\overline{Q}_{16} = (Q_{11} - Q_{12} - 2Q_{66})m^3n + (Q_{12} - Q_{22} + 2Q_{66})mn^3 \tag{2.12c}$$

$$\overline{Q}_{22} = Q_{11}n^4 + 2(Q_{12} + 2Q_{66})m^2n^2 + Q_{22}m^4 \tag{2.12d}$$

$$\overline{Q}_{26} = (Q_{11} - Q_{12} - 2Q_{66})mn^3 + (Q_{12} - Q_{22} + 2Q_{66})m^3n \tag{2.12e}$$

$$\overline{Q}_{66} = (Q_{11} - 2Q_{12} + Q_{22} - 2Q_{66})m^2n^2 + Q_{66}(m^4 + n4) \tag{2.12f}$$

The described equations, however, apply only to a single layer of the shell, and when dealing with a laminated composite body, the influence of each lamina must be accounted for. The force and moment resultants N_{ij} and M_{ij} that arise from the shells inner stresses are described by equations 2.13 and 2.14 for a general case [10].

$$\begin{Bmatrix} N_{xx} \\ N_{\theta\theta} \\ N_{x\theta} \end{Bmatrix} = \int_{-h/2}^{h/2} \begin{Bmatrix} \sigma_{xx} \\ \sigma_{\theta\theta} \\ \sigma_{x\theta} \end{Bmatrix} dz \tag{2.13}$$

$$\begin{Bmatrix} M_{xx} \\ M_{\theta\theta} \\ M_{x\theta} \end{Bmatrix} = \int_{-h/2}^{h/2} \begin{Bmatrix} \sigma_{xx} \\ \sigma_{\theta\theta} \\ \sigma_{x\theta} \end{Bmatrix} zdz \tag{2.14}$$

Taking this into account, a relation between these resultants and the strain components can be established, which gives rise to expression 2.15, whose matrix coefficients are expressed in equations 2.16. The index k refers to each layer in the order that is established by the stacking sequence represented in Figure 2.2, where N is the total number of layers of the body.

$$\begin{Bmatrix} N_{xx} \\ N_{\theta\theta} \\ N_{x\theta} \\ M_{xx} \\ M_{\theta\theta} \\ M_{x\theta} \end{Bmatrix} = \begin{bmatrix} A_{11} & A_{12} & A_{16} & B_{11} & B_{12} & B_{16} \\ A_{12} & A_{22} & A_{26} & B_{12} & B_{22} & B_{26} \\ A_{16} & A_{26} & A_{66} & B_{16} & B_{26} & B_{66} \\ B_{11} & B_{12} & B_{16} & D_{11} & D_{12} & D_{16} \\ B_{12} & B_{22} & B_{26} & D_{12} & D_{22} & D_{26} \\ B_{16} & B_{26} & B_{66} & D_{16} & D_{26} & D_{66} \end{bmatrix} \begin{Bmatrix} \varepsilon_{xx} \\ \varepsilon_{\theta\theta} \\ \varepsilon_{x\theta} \\ k_{xx} \\ k_{\theta\theta} \\ k_{x\theta} \end{Bmatrix} \tag{2.15}$$

$$A_{ij} = \sum_{k=1}^{N} \overline{Q}_{ij}^{(k)} (h_k - h_{k-1}) \tag{2.16a}$$

$$B_{ij} = \frac{1}{2} \sum_{k=1}^{N} \overline{Q}_{ij}^{(k)} (h_k^2 - h_{k-1}^2) \tag{2.16b}$$

$$D_{ij} = \frac{1}{3} \sum_{k=1}^{N} \overline{Q}_{ij}^{(k)} (h_k^3 - h_{k-1}^3) \tag{2.16c}$$

Analysing equations 2.16, it is concluded that coefficients B_{ij} are null when there is lamination symmetry along the middle surface of the shell. This property is taken advantage of, since exploring the effects of asymmetry on a composite laminated shell is not the goal of this study and this assumption allows to simplify further calculations. Also, note that for balanced layer setups, like $[\psi, -\psi]_s$, the terms A_{16} and A_{26} are null, and in the cases of cross ply laminates, where each laminate tow angle is either 0º or 90º, coefficients A_{16}, A_{26}, D_{16} and D_{26} are also null.

Keep in mind that these equations are valid for constant stiffness composite laminate shells as well for variable stiffness cases. The main difference arises in the definition of the transformation matrices, where its tow angle variable ψ is a function of the spatial coordinates. For this study, it is only considered that, in variable stiffness cases, the coefficients A_{ij}, B_{ij} and D_{ij} are a function of only the axial coordinate.

2.5 Equations of Motion

The equations of motion allow for an analysis of the relation between the internal efforts, the body's inertia and the external forces.

These equations may be obtained directly from Newton's second law of motion, which states that the sum of the force vectors applied to a body is equal to the mass times the acceleration. Considering the body forces in the x, θ and z directions, equations 2.17 are obtained, according to Qatu [10]. p_x, p_θ and p_z are the external pressure components applied to the body in the x, θ and z directions, respectively.

$$\frac{\partial N_{xx}}{\partial x}+\frac{1}{R}\frac{\partial N_{x\theta}}{\partial \theta}+p_x=\rho h\frac{\partial^2 u_0}{\partial t^2} \tag{2.17a}$$

$$\frac{1}{R}\frac{\partial N_{\theta\theta}}{\partial \theta}+\frac{\partial N_{x\theta}}{\partial x}+\frac{1}{R^2}\frac{\partial M_{\theta\theta}}{\partial \theta}+\frac{1}{R}\frac{\partial M_{x\theta}}{\partial x}+p_\theta=\rho h\frac{\partial^2 v_0}{\partial t^2} \tag{2.17b}$$

$$-\frac{N_{\theta\theta}}{R}+\frac{\partial^2 M_{xx}}{\partial x^2}+\frac{2}{R}\frac{\partial^2 M_{x\theta}}{\partial \theta\partial x}+\frac{1}{R^2}\frac{\partial^2 M_{\theta\theta}}{\partial \theta^2}+p_z=\rho h\frac{\partial^2 w_0}{\partial t^2} \tag{2.17c}$$

Substituting the internal effort terms in 2.17 by the relations in equation 2.15, equations 2.18 are obtained. Note the absence of B_{ij} terms, consequence of considering a symmetrically laminated shell in relation to the middle surface, as is stated in section 2.4.

$$\begin{aligned}-A_{11}\frac{\partial^2 u_0}{\partial x^2}-\frac{2A_{16}}{R}\frac{\partial^2 u_0}{\partial x\partial \theta}-\frac{A_{66}}{R^2}\frac{\partial^2 u_0}{\partial \theta^2}-A_{16}\frac{\partial^2 v_0}{\partial x^2}-\frac{A_{12}+A_{66}}{R}\frac{\partial^2 v_0}{\partial x\partial \theta}&\\ -\frac{A_{26}}{R^2}\frac{\partial^2 v_0}{\partial \theta^2}-\frac{A_{12}}{R}\frac{\partial w_0}{\partial x}-\frac{A_{26}}{R^2}\frac{\partial w_0}{\partial \theta}+\rho h\frac{\partial^2 u_0}{\partial t^2}&=p_x\end{aligned} \tag{2.18a}$$

$$\begin{aligned}-A_{16}\frac{\partial^2 u_0}{\partial x^2}-\frac{A_{12}+A_{66}}{R}\frac{\partial^2 u_0}{\partial x\partial \theta}-\frac{A_{26}}{R^2}\frac{\partial^2 u_0}{\partial \theta^2}-A_{66}\frac{\partial^2 v_0}{\partial x^2}-\frac{2A_{26}}{R}\frac{\partial^2 v_0}{\partial x\partial \theta}-\frac{A_{22}}{R^2}\frac{\partial^2 v_0}{\partial \theta^2}&\\ -\frac{D_{66}}{R^2}\frac{\partial^2 v_0}{\partial x^2}-\frac{2D_{26}}{R^3}\frac{\partial^2 v_0}{\partial x\partial \theta}-\frac{D_{22}}{R^4}\frac{\partial^2 v_0}{\partial \theta^2}+\frac{D_{16}}{R}\frac{\partial^3 w_0}{\partial x^3}+\frac{D_{22}}{R^4}\frac{\partial^3 w_0}{\partial \theta^3}+\frac{3D_{26}}{R^3}\frac{\partial^3 w_0}{\partial x\partial \theta^2}&\\ +\frac{D_{12}+2D_{66}}{R^2}\frac{\partial^3 w_0}{\partial x^2\partial \theta}-\frac{A_{26}}{R}\frac{\partial w_0}{\partial x}-\frac{A_{22}}{R^2}\frac{\partial w_0}{\partial \theta}+\rho h\frac{\partial^2 v_0}{\partial t^2}&=p_\theta\end{aligned} \tag{2.18b}$$

$$\begin{aligned}\frac{A_{12}}{R}\frac{\partial u_0}{\partial x}+\frac{A_{26}}{R^2}\frac{\partial u_0}{\partial \theta}-\frac{D_{16}}{R}\frac{\partial^3 v_0}{\partial x^3}-\frac{D_{22}}{R^4}\frac{\partial^3 v_0}{\partial \theta^3}-\frac{3D_{26}}{R^3}\frac{\partial^3 v_0}{\partial x\partial \theta^2}-\frac{D_{12}+2D_{66}}{R^2}\frac{\partial^3 v_0}{\partial x^2\partial \theta}&\\ +\frac{A_{26}}{R}\frac{\partial v_0}{\partial x}+\frac{A_{22}}{R^2}\frac{\partial v_0}{\partial \theta}+D_{11}\frac{\partial^4 w_0}{\partial x^4}+\frac{4D_{16}}{R}\frac{\partial^4 w_0}{\partial x^3\partial \theta}+\frac{2(D_{12}+2D_{66})}{R^2}\frac{\partial^4 w_0}{\partial x^2\partial \theta^2}&\\ +\frac{4D_{26}}{R^3}\frac{\partial^4 w_0}{\partial x\partial \theta^3}+\frac{D_{22}}{R^4}\frac{\partial^4 w_0}{\partial \theta^4}+\frac{A_{22}}{R^2}w_0+\rho h\frac{\partial^2 w_0}{\partial t^2}&=p_z\end{aligned} \tag{2.18c}$$

2.6 Boundary Conditions

The considered boundary conditions of a model impact the dynamic properties of the studied structure. Therefore, a brief study of the impact of the changes in boundary conditions is made, and so, 2 different types of boundary conditions are applied to cylindrical shells: clamped edges and simply supported edges.

The mathematical considerations for each boundary condition are made according to common examples found in the literature [7, 10]. For convenience's sake, it is considered that both edges of the cylinder are always supported under equal conditions.

Clamped Edges

For the case of clamped edges, it is considered that the edges have all of their membrane displacements locked, as well as the out-of-plane displacement disabled. Additionally, this boundary condition does not allow for transversal displacement slope.

In other words, equation 2.19 is respected for $x=0$ and for $x=l$. Note that all of these equations are boundary conditions of the geometric nature. The used notation to refer to this setup in this document is **C-C**.

$$w_0 = v_0 = u_0 = \frac{\partial w_0}{\partial x} = 0 \tag{2.19}$$

Simply Supported Edges

Simply supported edges, also known as shear diaphragm edges, is the second setup considered in this study and it does not allow for angular membrane displacement in the edges, nor out-of-plane displacement. Contrary to the previous case, simply supported edges allow the shell to be axially displaced in its edges, as well as it allows for a non-zero slope of the out-of-plane displacement.

Considering this, equations 2.20 are respected at $x=0$ and $x=l$, where equation 2.20 a) represents the geometric boundary conditions and 2.20 b) represent the natural boundary conditions. Equations 2.20 b) arise from the shell's freedom to be axially displaced, and so the N_x and M_x terms can be mathematically developed as seen in equations 2.21 and 2.22 (remember that the mathematical expressions for the shell's internal efforts can be found in section 2.4).

$$w_0 = v_0 = 0 \tag{2.20a}$$

$$M_x = N_x = 0 \tag{2.20b}$$

$$\begin{gathered} N_x = A_{11}\frac{\partial u_0}{\partial x} + A_{12}\left(\frac{1}{R}\frac{\partial v_0}{\partial \theta} + \frac{w_0}{R}\right) + A_{16}\left(\frac{1}{R}\frac{\partial u_0}{\partial \theta} + \frac{\partial v_0}{\partial x}\right) = 0 \\ N_x = A_{11}\frac{\partial u_0}{\partial x} + A_{16}\left(\frac{1}{R}\frac{\partial u_0}{\partial \theta} + \frac{\partial v_0}{\partial x}\right) = 0 \end{gathered} \tag{2.21}$$

$$\begin{gathered} M_x = -D_{11}\frac{\partial^2 w_0}{\partial x^2} + D_{12}\left(\frac{1}{R^2}\frac{\partial v_0}{\partial \theta} - \frac{1}{R^2}\frac{\partial^2 w_0}{\partial \theta^2}\right) + D_{16}\left(\frac{1}{R}\frac{\partial v_0}{\partial x} - \frac{2}{R}\frac{\partial^2 w_0}{\partial x \partial \theta}\right) = 0 \\ M_x = -D_{11}\frac{\partial^2 w_0}{\partial x^2} + D_{16}\frac{1}{R}\frac{\partial v_0}{\partial x} = 0 \end{gathered} \tag{2.22}$$

For the natural boundary conditions to be consistently respected, $\frac{\partial^2 w_0}{\partial x^2} = \frac{\partial u_0}{\partial \theta} = \frac{\partial v_0}{\partial x} = \frac{\partial u_0}{\partial x} = 0$ is imposed at $x=0$ and $x=l$.

The used notation to refer to simply supported edges is **S-S**.

2.7 Aerodynamic Pressure

The studied cylindrical shell is submitted to external forces consequent of an axial supersonic flow of air, as it is schematically represented by Figure 2.3. The linear piston theory [6, 61, 69, 70] is implemented into the model, as it provides a quasi-steady, point-function relation between the surface's displacement and velocity and the aerodynamic pressure, which renders a computationally inexpensive aerodynamic model.

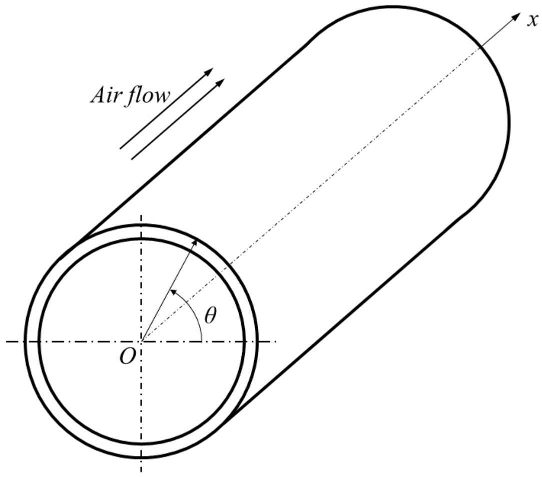

Figure 2.3: Schematic representation of a circular cylindrical shell subjected to the studied supersonic airflow.

The presented theory is valid for supersonic flow. Air is considered to flow on the outer surface of the shell with the flow velocity U_∞ along the x axis, while the inner surface is submitted to the undisturbed atmospheric pressure. No external force components in the x and θ direction are considered, so, the developed pressures only act on the radial direction. The aerodynamic pressure difference between the outer and inner surfaces at each point in space and time may be approximated by the linear equation 2.23 for $1.6 < M < 5$ [61, 62]. In this expression, γ stands for the air's specific heat ration, p_∞ is the free flow static pressure and a_∞ is the free flow speed of sound [61, 62, 71]. This is a local, zero memory relation, since the pressure at a given position and time does not depend upon the motion at other positions and previous times.

$$\Delta p_a = -\frac{\gamma p_\infty M^2}{\sqrt{M^2-1}}\left[\frac{\partial w}{\partial x} + \frac{1}{Ma_\infty}\left(\frac{M^2-2}{M^2-1}\right)\frac{\partial w}{\partial t} - \frac{w}{2R\sqrt{M^2-1}}\right] \tag{2.23}$$

2.8 The p-version Finite Element Method

In order to transform the partial differential equations of motion into ordinary differential equations, the finite element method is used, more specifically, a p-version finite element method (p-FEM), and its implementation is described in this section.

In contrast with the most typical and common h-version FEM, where solution convergence is obtained by refining the mesh or, in other words, increasing the number of elements, in the p-version FEM a low number of elements is used (in this case, only one element is modelled) and convergence is obtained by increasing the number of shape functions used as the mesh is not altered.

The p-version FEM is often called hierarchical FEM (HFEM) because the set of functions of a lower order approximation p is still used as a subset of functions on the better approximation of order $p+1$. This method has several advantages compared to h-FEM, as it maintains the versatility of the finite element method, while requiring a low number of elements and of degrees of freedom [72, 73]. In the h-FEM, the number of degrees of freedom has a big influence on the processing time, but in the p-FEM, the main influence is the number of calculated coefficients, which is the same as the number of shape functions used and can positively affect the processing time. Also, due to the lack of sub-domain separations, the obtained fields tend to be smoother and have a more consistent continuity throughout the domain. Additionally, if only one element is used, there is no need to incorporate a matrix assembly step into the method. Complex geometries tend to be more challenging to approximate with only one element. In these cases, several elements can be used to approximate the geometry while still maintaining most of the advantages of using the p-FEM. The p-version FEM and the h-version FEM can be combined into the h-p version of the finite element method, where the convergence of results to stable values is obtained by a refinement of the mesh as well as by an increase in the number of shape functions used. Babuška & Suri [74] present some of the main characteristics of both the p-FEM and the h-p FEM.

2.8.1 Shape Functions

As a first step on the implementation of a p-version of the finite element method, shape functions need to be chosen to approximate the solution.

The displacement field of the mid surface is a function dependent on 2 coordinates of space and it is therefore convenient to consider that each variable has an independent effect on the displacement field, or in other words, equation 2.24 is respected, where SF_i represents a generalized shape function.

$$SF_i(x,\theta) = SF_i(x) \cdot SF_i(\theta) \tag{2.24}$$

It is also convenient to adimensionalize the x coordinate into the ξ coordinate, that varies between -1 and 1. In this work, the relation between these two variables is as follows.

$$x = \frac{l}{2} \cdot (\xi + 1) \tag{2.25}$$

Let's first analyse the considered shape functions for the variations in the ξ direction. Two different sets are used: the f set of shape functions for the transverse displacement w_0 and the g set of shape functions for the membrane displacements u_0 and v_0.

The f set of shape functions is constituted by the Hermite cubics for the first four functions (equation 2.26) and by the so-called Rodrigues form of Legendre polynomials for the other functions (equation 2.27), where $r!! = r(r-2)...(2 \text{ or } 1)$, $0!! = (-1)!! = 1$ and $INT(r/2)$ denotes the integer part of $r/2$ [72,75]. As an additional note, the terms $(...)!!$ that are not considered as valid are not calculated.

This set allows for C^1 continuity and for an easy implementation of the geometrical boundary conditions. This is because only the f_1 and f_3 shape functions allow for a non zero displacement value in the ends of the element, and only the f_2 and f_4 shape functions allow for a non zero slope value at the boundary. Since all used shape functions, except the Hermite cubics, have zero amplitude and zero slope at $\xi = -1$ and $\xi = 1$, only the first four f shape functions have to be considered or disconsidered to match the geometrical boundary conditions. For example, in a simply supported cylinder at both ends, functions f_1 and f_3 are not used, and for a clamped cylinder at both ends, f_1, f_2, f_3 and f_4 are disregarded.

The first seven shape functions of the f set are graphically represented in Figure 2.4.

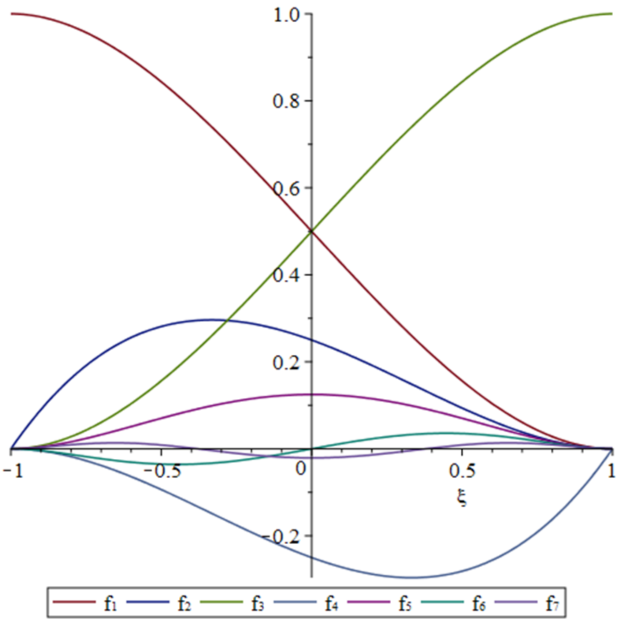

Figure 2.4: First seven shape functions of the f set.

$$f_1(\xi) = \frac{1}{2} - \frac{3}{4}\xi + \frac{1}{4}\xi^3 \tag{2.26a}$$

$$f_2(\xi) = \frac{1}{4} - \frac{1}{4}\xi - \frac{1}{4}\xi^2 + \frac{1}{4}\xi^3 \tag{2.26b}$$

$$f_3(\xi) = \frac{1}{2} + \frac{3}{4}\xi - \frac{1}{4}\xi^3 \tag{2.26c}$$

$$f_4(\xi) = -\frac{1}{4} - \frac{1}{4}\xi + \frac{1}{4}\xi^2 + \frac{1}{4}\xi^3 \tag{2.26d}$$

$$f_r(\xi) = \sum_{n=0}^{Int(r/2)} \frac{(-1)^n(2r-2n-7)!!}{2^n n!(r-2n-1)!}\xi^{r-2n-1}\ , r > 4 \tag{2.27}$$

The g set of shape functions is constituted by the linear shape functions represented in equation 2.28 for the first two functions and by the set represented in equation 2.29 for the following. With this set, C^0 continuity is ensured, and g_1 and g_2 are the only functions with a non zero amplitude at $\xi = -1$ and $\xi = 1$, so, only these functions need to be adjusted to respect the geometrical boundary conditions. Therefore, in clamped cylindrical shells g_1 and g_2 are not be used. In simply supported cylinders, g_1 and g_2 are disregarded for the v membrane displacement, but are used for the u membrane displacement, as this boundary condition allows for axial displacement of the shell [72,75,76].

The first seven shape functions of the g set are graphically represented in Figure 2.5.

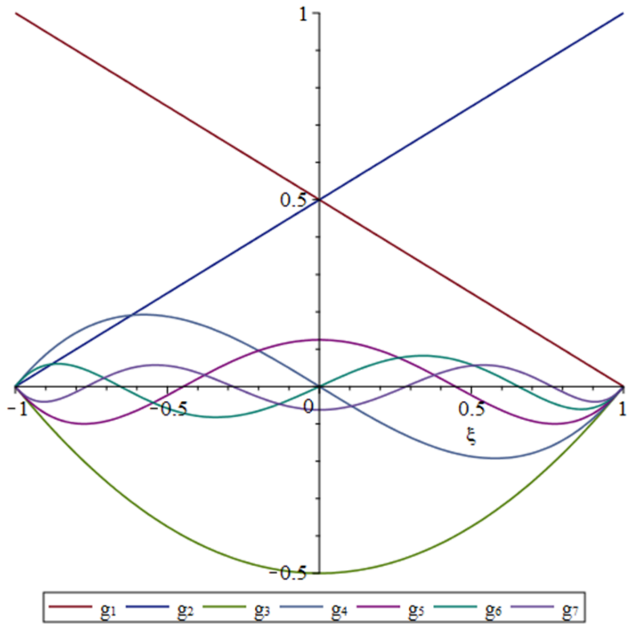

Figure 2.5: First seven shape functions of the g set.

$$g_1(\xi) = \frac{1}{2} - \frac{1}{2}\xi \tag{2.28a}$$

$$g_2(\xi) = \frac{1}{2} + \frac{1}{2}\xi \tag{2.28b}$$

$$g_r(\xi) = \sum_{n=0}^{Int(r/2)} \frac{(-1)^n(2r-2n-5)!!}{2^n n!(r-2n-1)!} \xi^{r-2n-1} \text{ , } r > 2 \tag{2.29}$$

As for the shape functions for the variation of the displacement field along the θ coordinate, a set of cosine functions are used for the u_0 and w_0 displacements (h_{ur} and h_{wr} functions, respectively) and a set of sine functions for the v_0 functions (h_{vr} functions). This set of functions is commonly used on the dynamic analysis of cylindrical shells along the θ coordinate, as it was done by Pellicano [13], Song et. al [17], Qin et. al [20] and Xie et. al [24], for example.

$$h_{ur}(\theta) = h_{wr}(\theta) = cos(r\theta) \tag{2.30a}$$

$$h_{vr}(\theta) = sin(r\theta) \tag{2.30b}$$

The h set of shape functions starts at a value of r that can be adjusted to the mode shapes that are intended to be studied. For example, if there is an intent on studying breathing modes, the corresponding shape functions to $r = 0$ should be included in the h set of shape functions. If there is no such goal, it can be disregarded, which enables to save processing time.

Considering this, the displacement vector $\mathbf{d}$ of a given mode shape is considered to be as seen in equation 2.31, where $\mathbf{N}$ is the shape function matrix, the generalized coordinates $\mathbf{q_t}(t)$ are time-dependent functions and $\delta_\mathbf{1}$, $\delta_\mathbf{2}$ and $\delta_\mathbf{3}$ are represented in equations 2.32 and are the shape functions vectors for the u_0, v_0 and w_0 displacement and the generalized coordinates, respectively. Consider that pt, pm and po are, respectively, the number of shape functions used from the h, g and f set of shape functions.

$$\mathbf{d} = \begin{Bmatrix} u_0 \\ v_0 \\ w_0 \end{Bmatrix} = \mathbf{N} \cdot \mathbf{q_t}(t) = \begin{bmatrix} \delta_\mathbf{1} & 0 & 0 \\ 0 & \delta_\mathbf{2} & 0 \\ 0 & 0 & \delta_\mathbf{3} \end{bmatrix} \cdot \mathbf{q_t}(t) \tag{2.31}$$

$$\delta\mathbf{1} = \{g_{u1}h_{u1}, g_{u1}h_{u2}, ..., g_{ui}h_{upt}, g_{u(i+1)}h_{u1}, g_{u(i+1)}h_{u2}, ..., g_{upm}h_{upt}\} \tag{2.32a}$$

$$\delta\mathbf{2} = \{g_{v1}h_{v1}, g_{v1}h_{v2}, ..., g_{vi}h_{vpt}, g_{v(i+1)}h_{v1}, g_{v(i+1)}h_{v2}, ..., g_{vpm}h_{vpt}\} \tag{2.32b}$$

$$\delta\mathbf{3} = \{f_1h_{w1}, f_1h_{w2}, ..., f_ih_{wpt}, f_{i+1}h_{w1}, f_{i+1}h_{w2}, ..., f_{po}h_{wpt}\} \tag{2.32c}$$

$$\tag{2.32d}$$

2.8.2 Stiffness and Mass Matrix Calculation

The equations of motion (equations 2.18) obtained previously need to be mathematically manipulated so the p-FEM may be implemented and the displacement field obtained. This way, the problem becomes of an algebraic nature, and its solution is easily computed.

Consider that the equations of motion are divided into different terms, so that each one may be worked on, as seen in equations 2.33.

$$\begin{aligned}
&\underbrace{-A_{11}\frac{\partial^2 u_0}{\partial x^2}}_{\text{term[1]}}-\underbrace{\frac{2A_{16}}{R}\frac{\partial^2 u_0}{\partial x\partial\theta}}_{\text{term[2]}}-\underbrace{\frac{A_{66}}{R^2}\frac{\partial^2 u_0}{\partial\theta^2}}_{\text{term[3]}}\underbrace{-A_{16}\frac{\partial^2 v_0}{\partial x^2}}_{\text{term[4])}}-\underbrace{\frac{A_{12}+A_{66}}{R}\frac{\partial^2 v_0}{\partial x\partial\theta}}_{\text{term[5]}}\\
&\qquad-\underbrace{\frac{A_{26}}{R^2}\frac{\partial^2 v_0}{\partial\theta^2}}_{\text{term[6]}}-\underbrace{\frac{A_{12}}{R}\frac{\partial w_0}{\partial x}}_{\text{term[7]}}-\underbrace{\frac{A_{26}}{R^2}\frac{\partial w_0}{\partial\theta}}_{\text{term[8]}}+\underbrace{\rho h\frac{\partial^2 u_0}{\partial t^2}}_{\text{term[9]}}=0
\end{aligned}\tag{2.33a}$$

$$\begin{aligned}
&\underbrace{-A_{16}\frac{\partial^2 u_0}{\partial x^2}}_{\text{term[10]}}-\underbrace{\frac{A_{12}+A_{66}}{R}\frac{\partial^2 u_0}{\partial x\partial\theta}}_{\text{term[11]}}-\underbrace{\frac{A_{26}}{R^2}\frac{\partial^2 u_0}{\partial\theta^2}}_{\text{term[12]}}\underbrace{-A_{66}\frac{\partial^2 v_0}{\partial x^2}}_{\text{term[13]}}-\underbrace{\frac{2A_{26}}{R}\frac{\partial^2 v_0}{\partial x\partial\theta}}_{\text{term[14]}}-\underbrace{\frac{A_{22}}{R^2}\frac{\partial^2 v_0}{\partial\theta^2}}_{\text{term[15]}}\\
&-\underbrace{\frac{D_{66}}{R^2}\frac{\partial^2 v_0}{\partial x^2}}_{\text{term[16]}}-\underbrace{\frac{2D_{26}}{R^3}\frac{\partial^2 v_0}{\partial x\partial\theta}}_{\text{term[17]}}-\underbrace{\frac{D_{22}}{R^4}\frac{\partial^2 v_0}{\partial\theta^2}}_{\text{term[18]}}+\underbrace{\frac{D_{16}}{R}\frac{\partial^3 w_0}{\partial x^3}}_{\text{term[19]}}+\underbrace{\frac{D_{22}}{R^4}\frac{\partial^3 w_0}{\partial\theta^3}}_{\text{term[20]}}+\underbrace{\frac{3D_{26}}{R^3}\frac{\partial^3 w_0}{\partial x\partial\theta^2}}_{\text{term[21]}}\\
&\qquad+\underbrace{\frac{D_{12}+2D_{66}}{R^2}\frac{\partial^3 w_0}{\partial x^2\partial\theta}}_{\text{term[22]}}-\underbrace{\frac{A_{26}}{R}\frac{\partial w_0}{\partial x}}_{\text{term[23]}}-\underbrace{\frac{A_{22}}{R^2}\frac{\partial w_0}{\partial\theta}}_{\text{term[24]}}+\underbrace{\rho h\frac{\partial^2 v_0}{\partial t^2}}_{\text{term[25]}}=0
\end{aligned}\tag{2.33b}$$

$$\begin{aligned}
&\underbrace{\frac{A_{12}}{R}\frac{\partial u_0}{\partial x}}_{\text{term[26]}}+\underbrace{\frac{A_{26}}{R^2}\frac{\partial u_0}{\partial\theta}}_{\text{term[27]}}-\underbrace{\frac{D_{16}}{R}\frac{\partial^3 v_0}{\partial x^3}}_{\text{term[28]}}-\underbrace{\frac{D_{22}}{R^4}\frac{\partial^3 v_0}{\partial\theta^3}}_{\text{term[29]}}-\underbrace{\frac{3D_{26}}{R^3}\frac{\partial^3 v_0}{\partial x\partial\theta^2}}_{\text{term[30]}}-\underbrace{\frac{D_{12}+2D_{66}}{R^2}\frac{\partial^3 v_0}{\partial x^2\partial\theta}}_{\text{term[31]}}\\
&+\underbrace{\frac{A_{26}}{R}\frac{\partial v_0}{\partial x}}_{\text{term[32]}}+\underbrace{\frac{A_{22}}{R^2}\frac{\partial v_0}{\partial\theta}}_{\text{term[33]}}+\underbrace{D_{11}\frac{\partial^4 w_0}{\partial x^4}}_{\text{term[34]}}+\underbrace{\frac{4D_{16}}{R}\frac{\partial^4 w_0}{\partial x^3\partial\theta}}_{\text{term[35]}}+\underbrace{\frac{2(D_{12}+2D_{66})}{R^2}\frac{\partial^4 w_0}{\partial x^2\partial\theta^2}}_{\text{term[36]}}\\
&\qquad+\underbrace{\frac{4D_{26}}{R^3}\frac{\partial^4 w_0}{\partial x\partial\theta^3}}_{\text{term[37]}}+\underbrace{\frac{D_{22}}{R^4}\frac{\partial^4 w_0}{\partial\theta^4}}_{\text{term[38]}}+\underbrace{\frac{A_{22}}{R^2}w_0}_{\text{term[39]}}+\underbrace{\rho h\frac{\partial^2 w_0}{\partial t^2}}_{\text{term[40]}}=p_a
\end{aligned}\tag{2.33c}$$

Keep in mind that u_0, v_0 and w_0 are considered to be linear combinations of their respective shape function set. The Galerkin method is implemented, and so, each equation is multiplied by its own shape function vector and integrated along its domain. Since the variable ξ substitutes the variable x in the shape functions, the following relation has to be made:

$$\iint_{\Omega}[....]\,\mathrm{d}A=\int_0^{2\pi}\int_{-1}^{1}[....]\frac{l}{2}\,\mathrm{d}\xi\,R\,\mathrm{d}\theta \tag{2.34a}$$

$$\frac{\partial[...]}{\partial x}=\frac{2}{l}\frac{\partial[...]}{\partial\xi} \tag{2.34b}$$

Considering this, the Galerkin method is implemented by integrating each shape function combination in each term and expanding it into matrix notation. The integration process of every term is represented in equations 2.35-2.74.

In these equations, coefficients A_{ij} and D_{ij} are also integrated along the ξ variable, as these terms vary when axial variable stiffness is considered.

It is also noteworthy that integration by parts is commonly applied in these expressions and, therefore, terms with the format $\left[\frac{\partial^k}{\partial\theta^k}(SF_{\theta i})\frac{\partial^l}{\partial\theta^l}(SF_{\theta j})\right]_0^{2\pi}$ and $\left[\frac{\partial^n}{\partial\xi^n}(SF_{\xi i})[...]\frac{\partial^m}{\partial\xi^m}(SF_{\xi j})\right]_{-1}^{1}$ appear. The first terms will always be equal to zero, since the shape functions that define the displacement field variation along the θ coordinate are periodic and repeat at $\theta = 0$ and at $\theta = 2\pi$. The second terms may be used to impose the natural boundary conditions, and will always be considered equal to zero for clamped edges (g_{ui},g_{vi}, f_{wi} and $\frac{\partial f_{wi}}{\partial\xi}$ are always null at the boundaries) and also for simply supported edges (g_{vi} and f_{wi} are always null at the boundaries and $\frac{\partial^2 f_{wi}}{\partial\xi^2}$, $\frac{\partial g_{vi}}{\partial\xi}$ and $\frac{\partial g_{ui}}{\partial\xi}$ are considered to be 0, as it is stated in section 2.6).

$$\begin{aligned} term[1] : \frac{lR}{2}\int_0^{2\pi}\int_{-1}^{1} g_{ui}h_{um}A_{11}\frac{4}{l^2}\frac{\partial^2}{\partial\xi^2}(g_{uj}h_{un})\,\mathrm{d}\xi\,\mathrm{d}\theta = \\ \frac{2R}{l}\left[\cancelto{0}{\left[g_{ui}A_{11}\frac{\partial g_{uj}}{\partial\xi}\right]_{-1}^{1}} - \int_{-1}^{1}\frac{\partial g_{ui}}{\partial\xi}A_{11}\frac{\partial g_{uj}}{\partial\xi}\,\mathrm{d}\xi\right]\int_0^{2\pi} h_{um}h_{un}\,\mathrm{d}\theta \end{aligned} \tag{2.35}$$

$$\begin{aligned} term[2] : \frac{lR}{2}\int_0^{2\pi}\int_{-1}^{1} g_{ui}h_{um}\frac{2A_{16}}{R}\frac{2}{l}\frac{\partial^2}{\partial\xi\partial\theta}(g_{uj}h_{un})\,\mathrm{d}\xi\,\mathrm{d}\theta = \\ 2\int_{-1}^{1} g_{ui}A_{16}\frac{\partial g_{uj}}{\partial\xi}\,\mathrm{d}\xi\int_0^{2\pi} h_{um}\frac{\partial h_{un}}{\partial\theta}\,\mathrm{d}\theta \end{aligned} \tag{2.36}$$

$$\begin{aligned} term[3] : \frac{lR}{2}\int_0^{2\pi}\int_{-1}^{1} g_{ui}h_{um}\frac{A_{66}}{R^2}\frac{\partial^2}{\partial\theta^2}(g_{uj}h_{un})\,\mathrm{d}\xi\,\mathrm{d}\theta = \\ \frac{l}{2R}\int_{-1}^{1} g_{ui}A_{66}g_{uj}\,\mathrm{d}\xi\left[\cancelto{0}{\left[h_{um}\frac{\partial h_{un}}{\partial\theta}\right]_0^{2\pi}} - \int_0^{2\pi}\frac{\partial h_{um}}{\partial\theta}\frac{\partial h_{un}}{\partial\theta}\,\mathrm{d}\theta\right] \end{aligned} \tag{2.37}$$

$$\begin{aligned} term[4] : \frac{lR}{2}\int_0^{2\pi}\int_{-1}^{1} g_{ui}h_{um}A_{16}\frac{4}{l^2}\frac{\partial^2}{\partial\xi^2}(g_{v}h_{vn})\,\mathrm{d}\xi\,\mathrm{d}\theta = \\ \frac{2R}{l}\left[\cancelto{0}{\left[g_{ui}A_{16}\frac{\partial g_{vj}}{\partial\xi}\right]_{-1}^{1}} - \int_{-1}^{1}\frac{\partial g_{ui}}{\partial\xi}A_{16}\frac{\partial g_{vj}}{\partial\xi}\,\mathrm{d}\xi\right]\int_0^{2\pi} h_{um}h_{vn}\,\mathrm{d}\theta \end{aligned} \tag{2.38}$$

$$
\begin{aligned}
term[5]: \frac{lR}{2}\int_0^{2\pi}\int_{-1}^{1} g_{ui}h_{um}\frac{A_{12}+A_{66}}{R}\frac{2}{l}\frac{\partial^2}{\partial\xi\partial\theta}(g_{vj}h_{vn})\,\mathrm{d}\xi\,\mathrm{d}\theta = \\
\int_{-1}^{1} g_{ui}(A_{12}+A_{66})\frac{\partial g_{vj}}{\partial\xi}\,\mathrm{d}\xi\int_0^{2\pi} h_{um}\frac{\partial h_{vn}}{\partial\theta}\,\mathrm{d}\theta
\end{aligned}
\tag{2.39}
$$

$$
\begin{aligned}
term[6]: \frac{lR}{2}\int_0^{2\pi}\int_{-1}^{1} g_{ui}h_{um}\frac{A_{26}}{R^2}\frac{\partial^2}{\partial\theta^2}(g_{vj}h_{vn})\,\mathrm{d}\xi\,\mathrm{d}\theta = \\
\frac{l}{2R}\int_{-1}^{1} g_{ui}A_{26}g_{vj}\,\mathrm{d}\xi\left[\overbrace{\cancel{\left[h_{um}\frac{\partial h_{vn}}{\partial\theta}\right]_0^{2\pi}}}^{0} - \int_0^{2\pi}\frac{\partial h_{um}}{\partial\theta}\frac{\partial h_{vn}}{\partial\theta}\,\mathrm{d}\theta\right]
\end{aligned}
\tag{2.40}
$$

$$
\begin{aligned}
term[7]: \frac{lR}{2}\int_0^{2\pi}\int_{-1}^{1} g_{ui}h_{um}\frac{A_{12}}{R}\frac{2}{l}\frac{\partial}{\partial\xi}(f_{wj}h_{wn})\,\mathrm{d}\xi\,\mathrm{d}\theta = \\
\int_{-1}^{1} g_{ui}A_{12}\frac{\partial f_{wj}}{\partial\xi}\,\mathrm{d}\xi\int_0^{2\pi} h_{um}h_{wn}\,\mathrm{d}\theta
\end{aligned}
\tag{2.41}
$$

$$
\begin{aligned}
term[8]: \frac{lR}{2}\int_0^{2\pi}\int_{-1}^{1} g_{ui}h_{um}\frac{A_{26}}{R^2}\frac{\partial}{\partial\theta}(f_{wj}h_{wn})\,\mathrm{d}\xi\,\mathrm{d}\theta = \\
\frac{l}{2R}\int_{-1}^{1} g_{ui}A_{26}f_{wj}\,\mathrm{d}\xi\int_0^{2\pi} h_{um}\frac{\partial h_{wn}}{\partial\theta}\,\mathrm{d}\theta
\end{aligned}
\tag{2.42}
$$

$$
\begin{aligned}
term[9]: \frac{lR}{2}\rho h\int_0^{2\pi}\int_{-1}^{1} g_{ui}h_{um}g_{uj}h_{un}\,\mathrm{d}\xi\,\mathrm{d}\theta = \\
\frac{lR}{2}\rho h\int_{-1}^{1} g_{ui}g_{uj}\,\mathrm{d}\xi\int_0^{2\pi} h_{um}h_{un}\,\mathrm{d}\theta
\end{aligned}
\tag{2.43}
$$

$$
\begin{aligned}
term[10]: \frac{lR}{2}\int_0^{2\pi}\int_{-1}^{1} g_{vi}h_{vm}A_{16}\frac{4}{l^2}\frac{\partial^2}{\partial\xi^2}(g_{uj}h_{un})\,\mathrm{d}\xi\,\mathrm{d}\theta = \\
\frac{2R}{l}\left[\overbrace{\cancel{\left[g_{vi}A_{16}\frac{\partial g_{uj}}{\partial\xi}\right]_{-1}^{1}}}^{0} - \int_{-1}^{1}\frac{\partial g_{vi}}{\partial\xi}A_{16}\frac{\partial g_{uj}}{\partial\xi}\,\mathrm{d}\xi\right]\int_0^{2\pi} h_{vm}h_{un}\,\mathrm{d}\theta
\end{aligned}
\tag{2.44}
$$

$$
\begin{aligned}
term[11]: \frac{lR}{2}\int_0^{2\pi}\int_{-1}^{1} g_{vi}h_{vm}\frac{A_{12}+A_{66}}{R}\frac{2}{l}\frac{\partial^2}{\partial\xi\partial\theta}(g_{uj}h_{un})\,\mathrm{d}\xi\,\mathrm{d}\theta = \\
\int_{-1}^{1} g_{vi}(A_{12}+A_{66})\frac{\partial g_{uj}}{\partial\xi}\,\mathrm{d}\xi\int_0^{2\pi} h_{vm}\frac{\partial h_{un}}{\partial\theta}\,\mathrm{d}\theta
\end{aligned}
\tag{2.45}
$$

$$
\begin{aligned}
&term[12] : \frac{lR}{2}\int_0^{2\pi}\int_{-1}^{1} g_{vi}h_{vm}\frac{A_{26}}{R^2}\frac{\partial^2}{\partial\theta^2}(g_{uj}h_{un})\,\mathrm{d}\xi\,\mathrm{d}\theta = \\
&\frac{l}{2R}\int_{-1}^{1} g_{vi}A_{26}g_{uj}\,\mathrm{d}\xi\left[\cancelto{0}{\left[h_{vm}\frac{\partial h_{un}}{\partial\theta}\right]_0^{2\pi}} - \int_0^{2\pi}\frac{\partial h_{vm}}{\partial\theta}\frac{\partial h_{un}}{\partial\theta}\,\mathrm{d}\theta\right]
\end{aligned}
\tag{2.46}
$$

$$
\begin{aligned}
&term[13] : \frac{lR}{2}\int_0^{2\pi}\int_{-1}^{1} g_{vi}h_{vm}A_{66}\frac{4}{l^2}\frac{\partial^2}{\partial\xi^2}(g_{vj}h_{vn})\,\mathrm{d}\xi\,\mathrm{d}\theta = \\
&\frac{2R}{l}\left[\cancelto{0}{\left[g_{vi}A_{66}\frac{\partial g_{vj}}{\partial\xi}\right]_{-1}^{1}} - \int_{-1}^{1}\frac{\partial g_{vi}}{\partial\xi}A_{66}\frac{\partial g_{vj}}{\partial\xi}\,\mathrm{d}\xi\right]\int_0^{2\pi} h_{vm}h_{vn}\,\mathrm{d}\theta
\end{aligned}
\tag{2.47}
$$

$$
\begin{aligned}
&term[14] : \frac{lR}{2}\int_0^{2\pi}\int_{-1}^{1} g_{vi}h_{vm}\frac{2A_{26}}{R}\frac{2}{l}\frac{\partial^2}{\partial\xi\partial\theta}(g_{vj}h_{vn})\,\mathrm{d}\xi\,\mathrm{d}\theta = \\
&\qquad 2\int_{-1}^{1} g_{vi}A_{26}\frac{\partial g_{vj}}{\partial\xi}\,\mathrm{d}\xi\int_0^{2\pi} h_{vm}\frac{\partial h_{vn}}{\partial\theta}\,\mathrm{d}\theta
\end{aligned}
\tag{2.48}
$$

$$
\begin{aligned}
&term[15] : \frac{lR}{2}\int_0^{2\pi}\int_{-1}^{1} g_{vi}h_{vm}\frac{A_{22}}{R^2}\frac{\partial^2}{\partial\theta^2}(g_{vj}h_{vn})\,\mathrm{d}\xi\,\mathrm{d}\theta = \\
&\frac{l}{2R}\int_{-1}^{1} g_{vi}A_{22}g_{vj}\,\mathrm{d}\xi\left[\cancelto{0}{\left[h_{vm}\frac{\partial h_{vn}}{\partial\theta}\right]_0^{2\pi}} - \int_0^{2\pi}\frac{\partial h_{vm}}{\partial\theta}\frac{\partial h_{vn}}{\partial\theta}\,\mathrm{d}\theta\right]
\end{aligned}
\tag{2.49}
$$

$$
\begin{aligned}
&term[16] : \frac{lR}{2}\int_0^{2\pi}\int_{-1}^{1} g_{vi}h_{vm}\frac{D_{66}}{R^2}\frac{4}{l^2}\frac{\partial^2}{\partial\xi^2}(g_{vj}h_{vn})\,\mathrm{d}\xi\,\mathrm{d}\theta = \\
&\frac{2}{lR}\left[\cancelto{0}{\left[g_{vi}D_{66}\frac{\partial g_{vj}}{\partial\xi}\right]_{-1}^{1}} - \int_{-1}^{1}\frac{\partial g_{vi}}{\partial\xi}D_{66}\frac{\partial g_{vj}}{\partial\xi}\,\mathrm{d}\xi\right]\int_0^{2\pi} h_{vm}h_{vn}\,\mathrm{d}\theta
\end{aligned}
\tag{2.50}
$$

$$
\begin{aligned}
&term[17] : \frac{lR}{2}\int_0^{2\pi}\int_{-1}^{1} g_{vi}h_{vm}\frac{2D_{26}}{R^3}\frac{2}{l}\frac{\partial^2}{\partial\xi\partial\theta}(g_{vj}h_{vn})\,\mathrm{d}\xi\,\mathrm{d}\theta = \\
&\qquad \frac{2}{R^2}\int_{-1}^{1} g_{vi}D_{26}\frac{\partial g_{vj}}{\partial\xi}\,\mathrm{d}\xi\int_0^{2\pi} h_{vm}\frac{\partial h_{vn}}{\partial\theta}\,\mathrm{d}\theta
\end{aligned}
\tag{2.51}
$$

$$
\begin{aligned}
&term[18]: \frac{lR}{2}\int_0^{2\pi}\int_{-1}^{1} g_{vi}h_{vm}\frac{D_{22}}{R^4}\frac{\partial^2}{\partial\theta^2}(g_{vj}h_{vn})\,\mathrm{d}\xi\,\mathrm{d}\theta = \\
&\frac{l}{2R^3}\int_{-1}^{1} g_{vi}D_{22}g_{vj}\,\mathrm{d}\xi\left[\cancelto{0}{\left[h_{vm}\frac{\partial h_{vn}}{\partial\theta}\right]_0^{2\pi}} - \int_0^{2\pi}\frac{\partial h_{vm}}{\partial\theta}\frac{\partial h_{vn}}{\partial\theta}\,\mathrm{d}\theta\right]
\end{aligned}
\tag{2.52}
$$

$$
\begin{aligned}
&term[19]: \frac{lR}{2}\int_0^{2\pi}\int_{-1}^{1} g_{vi}h_{vm}\frac{D_{16}}{R}\frac{8}{l^3}\frac{\partial^3}{\partial\xi^3}(f_{wj}h_{wn})\,\mathrm{d}\xi\,\mathrm{d}\theta = \\
&\frac{4}{l^2}\left[\cancelto{0}{\left[g_{vi}D_{16}\frac{\partial^2 f_{wj}}{\partial\xi^2}\right]_{-1}^{1}} - \int_{-1}^{1}\frac{\partial g_{vi}}{\partial\xi}D_{16}\frac{\partial^2 f_{wj}}{\partial\xi^2}\,\mathrm{d}\xi\right]\int_0^{2\pi} h_{vm}h_{wn}\,\mathrm{d}\theta
\end{aligned}
\tag{2.53}
$$

$$
\begin{aligned}
&term[20]: \frac{lR}{2}\int_0^{2\pi}\int_{-1}^{1} g_{vi}h_{vm}\frac{D_{22}}{R^4}\frac{\partial^3}{\partial\theta^3}(f_{wj}h_{wn})\,\mathrm{d}\xi\,\mathrm{d}\theta = \\
&\frac{l}{2R^3}\int_{-1}^{1} g_{vi}D_{22}f_{wj}\,\mathrm{d}\xi\left[\cancelto{0}{\left[h_{vm}\frac{\partial^2 h_{wn}}{\partial\theta^2}\right]_0^{2\pi}} - \int_0^{2\pi}\frac{\partial h_{vm}}{\partial\theta}\frac{\partial^2 h_{wn}}{\partial\theta^2}\,\mathrm{d}\theta\right]
\end{aligned}
\tag{2.54}
$$

$$
\begin{aligned}
&term[21]: \frac{lR}{2}\int_0^{2\pi}\int_{-1}^{1} g_{vi}h_{vm}\frac{3D_{26}}{R^3}\frac{2}{l}\frac{\partial^3}{\partial\xi\partial\theta^2}(f_{wj}h_{wn})\,\mathrm{d}\xi\,\mathrm{d}\theta = \\
&\frac{3}{R^2}\int_{-1}^{1} g_{vi}D_{26}\frac{\partial f_{wj}}{\partial\xi}\,\mathrm{d}\xi\left[\cancelto{0}{\left[h_{vm}\frac{\partial h_{wn}}{\partial\theta}\right]_0^{2\pi}} - \int_0^{2\pi}\frac{\partial h_{vm}}{\partial\theta}\frac{\partial h_{wn}}{\partial\theta}\,\mathrm{d}\theta\right]
\end{aligned}
\tag{2.55}
$$

$$
\begin{aligned}
&term[22]: \frac{lR}{2}\int_0^{2\pi}\int_{-1}^{1} g_{vi}h_{vm}\frac{D_{12}+2D_{66}}{R^2}\frac{4}{l^2}\frac{\partial^3}{\partial\xi^2\partial\theta}(f_{wj}h_{wn})\,\mathrm{d}\xi\,\mathrm{d}\theta = \\
&\frac{2}{lR}\left[\cancelto{0}{\left[g_{vi}(D_{12}+2D_{66})\frac{\partial f_{wj}}{\partial\xi}\right]_{-1}^{1}} - \int_{-1}^{1}\frac{\partial g_{vi}}{\partial\xi}(D_{12}+2D_{66})\frac{\partial f_{wj}}{\partial\xi}\,\mathrm{d}\xi\right]\int_0^{2\pi} h_{vm}\frac{\partial h_{wn}}{\partial\theta}\,\mathrm{d}\theta
\end{aligned}
\tag{2.56}
$$

$$
\begin{aligned}
&term[23]: \frac{lR}{2}\int_0^{2\pi}\int_{-1}^{1} g_{vi}h_{vm}\frac{A_{26}}{R}\frac{2}{l}\frac{\partial}{\partial\xi}(f_{wj}h_{wn})\,\mathrm{d}\xi\,\mathrm{d}\theta = \\
&\int_{-1}^{1} g_{vi}A_{26}\frac{\partial f_{wj}}{\partial\xi}\,\mathrm{d}\xi\int_0^{2\pi} h_{vm}h_{wn}\,\mathrm{d}\theta
\end{aligned}
\tag{2.57}
$$

$$
\begin{aligned}
term[24] : \frac{lR}{2}\int_0^{2\pi}\int_{-1}^{1} g_{vi}h_{vm}\frac{A_{22}}{R^2}\frac{\partial}{\partial\theta}(f_{wj}h_{wn})\,\mathrm{d}\xi\,\mathrm{d}\theta = \\
\frac{l}{2R}\int_{-1}^{1} g_{vi}A_{22}f_{wj}\,\mathrm{d}\xi\int_0^{2\pi} h_{vm}\frac{\partial h_{wn}}{\partial\theta}\,\mathrm{d}\theta
\end{aligned}
\tag{2.58}
$$

$$
\begin{aligned}
term[25] : \frac{lR}{2}\rho h\int_0^{2\pi}\int_{-1}^{1} g_{vi}h_{vm}g_{vj}h_{vn}\,\mathrm{d}\xi\,\mathrm{d}\theta = \\
\frac{lR}{2}\rho h\int_{-1}^{1} g_{vi}g_{vj}\,\mathrm{d}\xi\int_0^{2\pi} h_{vm}h_{vn}\,\mathrm{d}\theta
\end{aligned}
\tag{2.59}
$$

$$
\begin{aligned}
term[26] : \frac{lR}{2}\int_0^{2\pi}\int_{-1}^{1} f_{wi}h_{wm}\frac{A_{12}}{R}\frac{2}{l}\frac{\partial}{\partial\xi}(g_{uj}h_{un})\,\mathrm{d}\xi\,\mathrm{d}\theta = \\
\int_{-1}^{1} f_{wi}A_{12}\frac{\partial g_{uj}}{\partial\xi}\,\mathrm{d}\xi\int_0^{2\pi} h_{wm}h_{un}\,\mathrm{d}\theta
\end{aligned}
\tag{2.60}
$$

$$
\begin{aligned}
term[27] : \frac{lR}{2}\int_0^{2\pi}\int_{-1}^{1} f_{wi}h_{wm}\frac{A_{26}}{R^2}\frac{\partial}{\partial\theta}(g_{uj}h_{un})\,\mathrm{d}\xi\,\mathrm{d}\theta = \\
\frac{l}{2R}\int_{-1}^{1} f_{wi}A_{26}g_{uj}\,\mathrm{d}\xi\int_0^{2\pi} h_{wm}\frac{\partial h_{un}}{\partial\theta}\,\mathrm{d}\theta
\end{aligned}
\tag{2.61}
$$

$$
\begin{aligned}
term[28] : \frac{lR}{2}\int_0^{2\pi}\int_{-1}^{1} f_{wi}h_{wm}\frac{D_{16}}{R}\frac{8}{l^3}\frac{\partial^3}{\partial\xi^3}(g_{vj}h_{vn})\,\mathrm{d}\xi\,\mathrm{d}\theta = \\
\frac{4}{l^2}\left[\cancelto{0}{\left[f_{wi}D_{16}\frac{\partial^2 g_{vj}}{\partial\xi^2}\right]_{-1}^{1}} - \int_{-1}^{1}\frac{\partial f_{wi}}{\partial\xi}D_{16}\frac{\partial^2 g_{vj}}{\partial\xi^2}\,\mathrm{d}\xi\right]\int_0^{2\pi} h_{wm}h_{vn}\,\mathrm{d}\theta
\end{aligned}
\tag{2.62}
$$

$$
\begin{aligned}
term[29] : \frac{lR}{2}\int_0^{2\pi}\int_{-1}^{1} f_{wi}h_{wm}\frac{D_{22}}{R^4}\frac{\partial^3}{\partial\theta^3}(g_{vj}h_{vn})\,\mathrm{d}\xi\,\mathrm{d}\theta = \\
\frac{l}{2R^3}\int_{-1}^{1} f_{wi}D_{22}g_{vj}\,\mathrm{d}\xi\left[\cancelto{0}{\left[h_{wm}\frac{\partial^2 h_{vn}}{\partial\theta^2}\right]_{0}^{2\pi}} - \int_0^{2\pi}\frac{\partial h_{wm}}{\partial\theta}\frac{\partial^2 h_{vn}}{\partial\theta^2}\,\mathrm{d}\theta\right]
\end{aligned}
\tag{2.63}
$$

$$
\begin{aligned}
term[30] : \frac{lR}{2}\int_0^{2\pi}\int_{-1}^{1} f_{wi}h_{wm}\frac{3D_{26}}{R^3}\frac{2}{l}\frac{\partial^3}{\partial\xi\partial\theta^2}(g_{vj}h_{vn})\,\mathrm{d}\xi\,\mathrm{d}\theta = \\
\frac{3}{R^2}\int_{-1}^{1} f_{wi}D_{26}\frac{\partial g_{vj}}{\partial\xi}\,\mathrm{d}\xi\left[\cancelto{0}{\left[h_{wm}\frac{\partial h_{vn}}{\partial\theta}\right]_{0}^{2\pi}} - \int_0^{2\pi}\frac{\partial h_{wm}}{\partial\theta}\frac{\partial h_{vn}}{\partial\theta}\,\mathrm{d}\theta\right]
\end{aligned}
\tag{2.64}
$$

$$
\begin{aligned}
term[31]: \frac{lR}{2}\int_0^{2\pi}\int_{-1}^{1} f_{wi}h_{wm}\frac{D_{12}+2D_{66}}{R^2}\frac{4}{l^2}\frac{\partial^3}{\partial\xi^2\partial\theta}(g_{vj}h_{vn})\,\mathrm{d}\xi\,\mathrm{d}\theta = \\
\frac{2}{lR}\left[\cancelto{0}{\left[f_{wi}(D_{12}+2D_{66})\frac{\partial g_{vj}}{\partial\xi}\right]_{-1}^{1}} - \int_{-1}^{1}\frac{\partial f_{wi}}{\partial\xi}(D_{12}+2D_{66})\frac{\partial g_{vj}}{\partial\xi}\,\mathrm{d}\xi\right]\int_0^{2\pi} h_{wm}\frac{\partial h_{vn}}{\partial\theta}\,\mathrm{d}\theta
\end{aligned}
\tag{2.65}
$$

$$
\begin{aligned}
term[32]: \frac{lR}{2}\int_0^{2\pi}\int_{-1}^{1} f_{wi}h_{wm}\frac{A_{26}}{R}\frac{2}{l}\frac{\partial}{\partial\xi}(g_{vj}h_{vn})\,\mathrm{d}\xi\,\mathrm{d}\theta = \\
\int_{-1}^{1} f_{wi}A_{26}\frac{\partial g_{vj}}{\partial\xi}\,\mathrm{d}\xi\int_0^{2\pi} h_{wm}h_{vn}\,\mathrm{d}\theta
\end{aligned}
\tag{2.66}
$$

$$
\begin{aligned}
term[33]: \frac{lR}{2}\int_0^{2\pi}\int_{-1}^{1} f_{wi}h_{wm}\frac{A_{22}}{R^2}\frac{\partial}{\partial\theta}(g_{vj}h_{vn})\,\mathrm{d}\xi\,\mathrm{d}\theta = \\
\frac{l}{2R}\int_{-1}^{1} f_{wi}A_{22}g_{vj}\,\mathrm{d}\xi\int_0^{2\pi} h_{wm}\frac{\partial h_{vn}}{\partial\theta}\,\mathrm{d}\theta
\end{aligned}
\tag{2.67}
$$

$$
\begin{aligned}
term[34]: \frac{lR}{2}\int_0^{2\pi}\int_{-1}^{1} f_{wi}h_{wm}D_{11}\frac{16}{l^4}\frac{\partial^4}{\partial\xi^4}(f_{wj}h_{wn})\,\mathrm{d}\xi\,\mathrm{d}\theta = \\
\frac{8R}{l^3}\left[\left[f_{wi}D_{11}\frac{\partial^3 f_{wj}}{\partial\xi^3}\right]_{-1}^{1} - \int_{-1}^{1}\frac{\partial f_{wi}}{\partial\xi}D_{11}\frac{\partial^3 f_{wj}}{\partial\xi^3}\,\mathrm{d}\xi\right]\int_0^{2\pi} h_{wm}h_{wn}\,\mathrm{d}\theta = \\
\frac{8R}{l^3}\left[\cancelto{0}{\left[f_{wi}D_{11}\frac{\partial^3 f_{wj}}{\partial\xi^3}\right]_{-1}^{1}} - \cancelto{0}{\left[\frac{\partial f_{wj}}{\partial\xi}D_{11}\frac{\partial^2 f_{wj}}{\partial\xi^2}\right]_{-1}^{1}} + \int_{-1}^{1}\frac{\partial^2 f_{wi}}{\partial\xi^2}D_{11}\frac{\partial^2 f_{wj}}{\partial\xi^2}\,\mathrm{d}\xi\right]\int_0^{2\pi} h_{wm}h_{wn}\,\mathrm{d}\theta
\end{aligned}
\tag{2.68}
$$

$$
\begin{aligned}
term[35]: \frac{lR}{2}\int_0^{2\pi}\int_{-1}^{1} f_{wi}h_{wm}\frac{4D_{16}}{R}\frac{8}{l^3}\frac{\partial^4}{\partial\xi^3\partial\theta}(f_{wj}h_{wn})\,\mathrm{d}\xi\,\mathrm{d}\theta = \\
\frac{16}{l^2}\left[\cancelto{0}{\left[f_{wi}D_{16}\frac{\partial^2 f_{wj}}{\partial\xi^2}\right]_{-1}^{1}} - \int_{-1}^{1}\frac{\partial f_{wi}}{\partial\xi}D_{16}\frac{\partial^2 f_{wj}}{\partial\xi^2}\,\mathrm{d}\xi\right]\int_0^{2\pi} h_{wm}\frac{\partial h_{wn}}{\partial\theta}\,\mathrm{d}\theta
\end{aligned}
\tag{2.69}
$$

$$
\begin{aligned}
term[36]: \frac{lR}{2}\int_0^{2\pi}\int_{-1}^{1} f_{wi}h_{wm}\frac{2(D_{12}+2D_{66})}{R^2}\frac{4}{l^2}\frac{\partial^4}{\partial\xi^2\partial\theta^2}(f_{wj}h_{wn})\,\mathrm{d}\xi\,\mathrm{d}\theta = \\
\frac{4}{lR}\left[\cancelto{0}{\left[f_{wi}(D_{12}+2D_{66})\frac{\partial f_{wj}}{\partial\xi}\right]_{-1}^{1}} - \int_{-1}^{1}\frac{\partial f_{wi}}{\partial\xi}(D_{12}+2D_{66})\frac{\partial f_{wj}}{\partial\xi}\,\mathrm{d}\xi\right]\cdot \\
\cdot\left[\cancelto{0}{\left[h_{wm}\frac{\partial h_{wn}}{\partial\theta}\right]_{0}^{2\pi}} - \int_0^{2\pi}\frac{\partial h_{wm}}{\partial\theta}\frac{\partial h_{wn}}{\partial\theta}\,\mathrm{d}\theta\right]
\end{aligned}
\tag{2.70}
$$

$$
\begin{aligned}
&term[37] : \frac{lR}{2}\int_0^{2\pi}\int_{-1}^{1} f_{wi}h_{wm}\frac{4D_{26}}{R^3}\frac{2}{l}\frac{\partial^4}{\partial\xi\partial\theta^3}(f_{wj}h_{wn})\,\mathrm{d}\xi\,\mathrm{d}\theta = \\
&\frac{4}{R^2}\int_{-1}^{1} f_{wi}D_{26}\frac{\partial f_{wj}}{\partial\xi}\,\mathrm{d}\xi\left[\cancelto{0}{\left[h_{wm}\frac{\partial^2 h_{wn}}{\partial\theta^2}\right]_0^{2\pi}} - \int_0^{2\pi}\frac{\partial h_{wm}}{\partial\theta}\frac{\partial^2 h_{wn}}{\partial\theta^2}\,\mathrm{d}\theta\right]
\end{aligned}
\tag{2.71}
$$

$$
\begin{aligned}
&term[38] : \frac{lR}{2}\int_0^{2\pi}\int_{-1}^{1} f_{wi}h_{wm}\frac{D_{22}}{R^4}\frac{\partial^4}{\partial\theta^4}(f_{wj}h_{wn})\,\mathrm{d}\xi\,\mathrm{d}\theta = \\
&\frac{l}{2R^3}\int_{-1}^{1} f_{wi}D_{22}f_{wj}\,\mathrm{d}\xi\left[\left[h_{wm}\frac{\partial^3 h_{wn}}{\partial\theta^3}\right]_0^{2\pi} - \int_0^{2\pi}\frac{\partial h_{wm}}{\partial\theta}\frac{\partial^3 h_{wn}}{\partial\theta^3}\,\mathrm{d}\theta\right] = \\
&\frac{l}{2R^3}\int_{-1}^{1} f_{wi}D_{22}f_{wj}\,\mathrm{d}\xi\left[\cancelto{0}{\left[h_{wm}\frac{\partial^3 h_{wn}}{\partial\theta^3}\right]_0^{2\pi}} - \cancelto{0}{\left[\frac{\partial h_{wm}}{\partial\theta}\frac{\partial^2 h_{wn}}{\partial\theta^2}\right]_0^{2\pi}} + \int_0^{2\pi}\frac{\partial^2 h_{wm}}{\partial\theta^2}\frac{\partial^2 h_{wn}}{\partial\theta^2}\,\mathrm{d}\theta\right]
\end{aligned}
\tag{2.72}
$$

$$
\begin{aligned}
&term[39] : \frac{lR}{2}\int_0^{2\pi}\int_{-1}^{1} f_{wi}h_{wm}\frac{A_{22}}{R^2}f_{wj}h_{wn}\,\mathrm{d}\xi\,\mathrm{d}\theta = \\
&\frac{l}{2R}\int_{-1}^{1} f_{wi}A_{22}f_{wj}\,\mathrm{d}\xi\int_0^{2\pi} h_{wm}h_{wn}\,\mathrm{d}\theta
\end{aligned}
\tag{2.73}
$$

$$
\begin{aligned}
&term[40] : \frac{lR}{2}\rho h\int_0^{2\pi}\int_{-1}^{1} f_{wi}h_{wm}f_{wj}h_{wn}\,\mathrm{d}\xi\,\mathrm{d}\theta = \\
&\frac{lR}{2}\rho h\int_{-1}^{1} f_{wi}f_{wj}\,\mathrm{d}\xi\int_0^{2\pi} h_{wm}h_{wn}\,\mathrm{d}\theta
\end{aligned}
\tag{2.74}
$$

After each term is integrated and expanded into matrix notation, the stiffness and mass matrices (**K** and **M**) can be obtained. These matrices can be thought as an assembly of the sub-matrices $\mathbf{K_{ij}}$ and $\mathbf{M_{ij}}$, as seen in equations 2.75 and 2.76.

$$
\mathbf{K} = \begin{bmatrix} \mathbf{K_{uu}} & \mathbf{K_{uv}} & \mathbf{K_{uw}} \\ \mathbf{K_{vu}} & \mathbf{K_{vv}} & \mathbf{K_{vw}} \\ \mathbf{K_{wu}} & \mathbf{K_{wv}} & \mathbf{K_{ww}} \end{bmatrix}
\tag{2.75}
$$

$$
\mathbf{M} = \begin{bmatrix} \mathbf{M_{uu}} & 0 & 0 \\ 0 & \mathbf{M_{vv}} & 0 \\ 0 & 0 & \mathbf{M_{ww}} \end{bmatrix}
\tag{2.76}
$$

Each sub-matrix can be obtained by combining the influence of each term (expanded into matrix notation) as follows:

- $\mathbf{K_{uu}} \longleftarrow -[term[1]] - [term[2]] - [term[3]]$
- $\mathbf{K_{uv}} \longleftarrow -[term[4]] - [term[5]] - [term[6]]$
- $\mathbf{K_{uw}} \longleftarrow -[term[7]] - [term[8]]$
- $\mathbf{K_{vu}} \longleftarrow -[term[10]] - [term[11]] - [term[12]]$
- $\mathbf{K_{vv}} \longleftarrow -[term[13]] - [term[14]] - [term[15]] - [term[16]] - [term[17]] - [term[18]]$
- $\mathbf{K_{vw}} \longleftarrow [term[19]] + [term[20]] + [term[21]] + [term[22]] - [term[23]] - [term[24]]$
- $\mathbf{K_{wu}} \longleftarrow [term[26]] + [term[27]]$
- $\mathbf{K_{wv}} \longleftarrow -[term[28]] - [term[29]] - [term[30]] - [term[31]] + [term[32]] + [term[33]]$
- $\mathbf{K_{ww}} \longleftarrow [term[34]] + [term[35]] + [term[36]] + [term[37]] + [term[38]] + [term[39]]$
- $\mathbf{M_{uu}} \longleftarrow [term[9]]$
- $\mathbf{M_{vv}} \longleftarrow [term[25]]$
- $\mathbf{M_{ww}} \longleftarrow [term[40]]$

After the Galerkin method is applied, the equations of motion become equation 2.77. Consider that $\dot{\mathbf{q}}_{\mathbf{t}}(t)$ and $\ddot{\mathbf{q}}_{\mathbf{t}}(t)$ are the first and second time derivatives of $\mathbf{q_t}(t)$, respectively. Note that matrices $\mathbf{K}$ and $\mathbf{M}$ are square symmetrical matrices, with the same number of rows and columns as the number of total shape functions $SF_{\xi\theta}$ used. This value is equal to $pt \cdot (2 \cdot pm + po)$.

$$\mathbf{M} \cdot \ddot{\mathbf{q}}_{\mathbf{t}}(t) + \mathbf{K} \cdot \mathbf{q_t}(t) = \mathbf{p} \tag{2.77}$$

2.8.3 Natural Frequencies and Natural Mode Shapes

Before studying how the cylindrical shell acts on supersonic flutter conditions, the natural mode shapes and natural frequencies of vibration are calculated. This step is useful to understand the body's dynamic properties and to validate the model, by comparing it to results found in other literature.

Under free vibration conditions, no external loads are applied to the shell and, therefore, vector $\mathbf{p}$ is neglected in equation 2.77. The generalized coordinates of a shell under free vibration are often considered to be $\mathbf{q_t}(t) = \mathbf{q} \cdot cos(\omega \cdot t)$, and, by doing this, equation 2.77 turns into expression 2.78, which can be further developed into equation 2.79.

$$-\omega^2 \cdot \mathbf{M} \cdot \mathbf{q} \cdot cos(\omega \cdot t) + \mathbf{K} \cdot \mathbf{q} \cdot cos(\omega \cdot t) = 0 \tag{2.78}$$

$$\mathbf{K} \cdot \mathbf{q} = \omega^2 \cdot \mathbf{M} \cdot \mathbf{q} \tag{2.79}$$

Notice that this expression defines a generalized eigenvalue problem. The obtained eigenvalues correspond to the squared natural frequencies ω_i^2 of the system, and each obtained eigenvector multiplied by the shape function matrix defines the correspondent natural mode shape. Therefore, the motion under free vibration of a given natural mode is equal to $\mathbf{N} \cdot \mathbf{q} \cdot cos(\omega \cdot t)$.

2.9 Implementing Viscous Damping

In practical cases, a dynamic system may not be only a function of the applied external forces and its stiffness and mass properties, but also of its damping properties.

Therefore, a damping matrix $\mathbf{C}$ can be added into the equations of motion as seen in equation 2.80. This is known as proportional damping, or Rayleigh-type damping [12]. This matrix may be obtained for a given structure with a specific material and viscous damping through an experimental procedure. One way of mathematically describing $\mathbf{C}$ is as a linear combination of the stiffness and mass matrices, as seen in expression 2.81, where α and β are parameters obtained through experimental means.

$$\mathbf{M} \cdot \ddot{\mathbf{q}}_\mathbf{t}(t) + \mathbf{C} \cdot \dot{\mathbf{q}}_\mathbf{t}(t) + \mathbf{K} \cdot \mathbf{q}_\mathbf{t}(t) = \mathbf{p} \tag{2.80}$$

$$\mathbf{C} = \alpha \cdot \mathbf{M} + \beta \cdot \mathbf{K} \tag{2.81}$$

This dissertation does not focus on the analysis of cylindrical shells with structural damping due to the lack of resources to experimentally find real values of α and β, however, the means of implementing viscous damping on the model is included to increase its versatility.

2.10 Supersonic Flutter

The goal of this study is to understand how VSCL can be used to increase the values of static pressure at which supersonic flutter occurs, in comparison to conventional CSCL. Therefore, this phenomenon must be modelled and implemented into the finite element model.

It has been established in section 2.7 that the aerodynamic pressure experienced by the cylindrical shell may be modeled recurring to the first order piston theory, as seen in expression 2.23. This equation is a function of the shell's radial displacement w, slope $\frac{\partial w}{\partial x}$ and velocity $\frac{\partial w}{\partial t}$, as well as a function of constants dependent of the flow characteristics and the cylinder geometry. These variables may be divided into the steady terms, which are related to the aerodynamic stiffness and influence the stiffness matrix on the FEM model, and into the unsteady term, which is related to the aerodynamic damping and affects the damping matrix on the FEM model. This division is explicit in equation 2.82.

$$\Delta p_a = \underbrace{-\frac{\gamma p_\infty M^2}{\sqrt{M^2-1}} \cdot \left[\underbrace{\frac{\partial w}{\partial x}}_{\text{term 41}} - \frac{1}{2R\sqrt{M^2-1}} \cdot \underbrace{w}_{\text{term42}} \right]}_{\text{steady terms}} \underbrace{- \frac{\gamma p_\infty M^2}{\sqrt{M^2-1}} \cdot \frac{1}{Ma_\infty} \left(\frac{M^2-2}{M^2-1} \right) \cdot \underbrace{\frac{\partial w}{\partial t}}_{\text{term42}}}_{\text{unsteady terms}} \tag{2.82}$$

The Galerkin method is applied, and a similar procedure to that seen in section 2.8.2 is performed to turn terms 41 and 42 (present in expression 2.82) into matrix notation, as it is seen in equations 2.83 and 2.84.

$$\begin{aligned} term[41] : \frac{lR}{2} \int_0^{2\pi} \int_{-1}^{1} f_{wi} h_{wm} \frac{2}{l} \frac{\partial}{\partial \xi} (f_{wj} h_{wn}) \, d\xi \, d\theta = \\ R \int_{-1}^{1} f_{wi} \frac{\partial f_{wj}}{\partial \xi} \, d\xi \int_0^{2\pi} h_{wm} h_{wn} \, d\theta \end{aligned} \tag{2.83}$$

$$\begin{aligned} term[42] : \frac{lR}{2} \int_0^{2\pi} \int_{-1}^{1} f_{wi} h_{wm} f_{wj} h_{wn} \, d\xi \, d\theta = \\ \frac{lR}{2} \int_{-1}^{1} f_{wi} f_{wj} \, d\xi \int_0^{2\pi} h_{wm} h_{wn} \, d\theta \end{aligned} \tag{2.84}$$

These terms can be arranged into the sub-matrices $\mathbf{F_s}$ and $\mathbf{F_u}$, as follows:

- $\mathbf{F_s} \longleftarrow + \frac{\gamma p_\infty M^2}{\sqrt{M^2-1}} \cdot \left([term[41]] - \frac{1}{2R\sqrt{M^2-1}} \cdot [term[42]] \right)$
- $\mathbf{F_u} \longleftarrow + \frac{\gamma p_\infty M^2}{\sqrt{M^2-1}} \cdot \frac{1}{Ma_\infty} \cdot \left(\frac{M^2-2}{M^2-1} \right) \cdot [term[42]]$

Then, the aerodynamic stiffness and damping matrices $\mathbf{F_{steady}}$ and $\mathbf{F_{unsteady}}$ can be obtained by arranging the sub-matrices $\mathbf{F_s}$ and $\mathbf{F_u}$ as follows:

$$\mathbf{F_{steady}} = \begin{bmatrix} 0 & 0 & 0 \\ 0 & 0 & 0 \\ 0 & 0 & \mathbf{F_s} \end{bmatrix}, \mathbf{F_{unsteady}} = \begin{bmatrix} 0 & 0 & 0 \\ 0 & 0 & 0 \\ 0 & 0 & \mathbf{F_u} \end{bmatrix} \tag{2.85}$$

Considering this, the equations of motion can be expressed as seen in equation 2.86.

$$\mathbf{M} \cdot \ddot{\mathbf{q}}_{\mathbf{t}}(t) + (\mathbf{C} + \mathbf{F}_{\mathbf{unsteady}}) \cdot \dot{\mathbf{q}}_{\mathbf{t}}(t) + (\mathbf{K} + \mathbf{F}_{\mathbf{steady}}) \cdot \mathbf{q}_{\mathbf{t}}(t) = 0 \tag{2.86}$$

By introducing the vector of state space coordinates composed by vectors $\dot{\mathbf{q}}_{\mathbf{t}}(t)$ and $\mathbf{q}_{\mathbf{t}}(t)$ that represent the velocity and displacement fields, respectively, the latter equation is rearranged into equation 2.87.

$$\begin{bmatrix} \mathbf{M} & 0 \\ 0 & -\mathbf{M} \end{bmatrix} \begin{Bmatrix} \ddot{\mathbf{q}}_{\mathbf{t}}(t) \\ \dot{\mathbf{q}}_{\mathbf{t}}(t) \end{Bmatrix} + \begin{bmatrix} \mathbf{C} + \mathbf{F}_{\mathbf{unsteady}} & \mathbf{K} + \mathbf{F}_{\mathbf{steady}} \\ \mathbf{M} & 0 \end{bmatrix} \begin{Bmatrix} \dot{\mathbf{q}}_{\mathbf{t}}(t) \\ \mathbf{q}_{\mathbf{t}}(t) \end{Bmatrix} = \begin{Bmatrix} 0 \\ 0 \end{Bmatrix} \tag{2.87}$$

By considering that $\mathbf{q}_{\mathbf{t}} = \mathbf{q} \cdot e^{\Omega \cdot t}$ and that $\ddot{\mathbf{q}}_{\mathbf{t}} = \Omega \cdot \dot{\mathbf{q}}_{\mathbf{t}}$ and $\dot{\mathbf{q}}_{\mathbf{t}} = \Omega \cdot \mathbf{q}_{\mathbf{t}}$ a generic eigenvalue problem can be obtained, as seen in equation 2.88. In equation 2.87, the matrices are multiplied by the phase space coordinate vector and in equation 2.88 they are multiplied by a vector obtained by the mathematical manipulation of the phase state vector, where $\mathbf{y} = \dot{\mathbf{q}}_{\mathbf{t}}/e^{\Omega t}$. Even though this arrangement doubles the dimension of the involved matrices, it is useful to linearize the system of equations.

$$\Omega \begin{bmatrix} -\mathbf{M} & 0 \\ 0 & \mathbf{M} \end{bmatrix} \begin{Bmatrix} \mathbf{y} \\ \mathbf{q} \end{Bmatrix} = \begin{bmatrix} \mathbf{C} + \mathbf{F}_{\mathbf{unsteady}} & \mathbf{K} + \mathbf{F}_{\mathbf{steady}} \\ \mathbf{M} & 0 \end{bmatrix} \begin{Bmatrix} \mathbf{y} \\ \mathbf{q} \end{Bmatrix} \tag{2.88}$$

The obtained eigenvalues Ω are complex conjugate pairs that contain a real component $\mathfrak{Re}(\Omega)$, as well as an imaginary part $\mathfrak{Im}(\Omega)$. Consequently, the eigenvectors are also complex conjugate pairs. So, the dynamic response of these shells to the axial airflow can be defined by the expression 2.89, where **d** corresponds to the displacement vector and **v** to the velocity vector. Consider that q_i is one of the terms of the **q** vector, that $e^{\pm\Omega t} = e^{\mathfrak{Re}(\Omega)} \cdot (cos(\mathfrak{Im}(\Omega) \cdot t) \pm i \cdot sin(\mathfrak{Im}(\Omega) \cdot t))$ and that $\overline{q_i}$ is the conjugate pair of q_i. By considering the influence of the term q_i and $\overline{q_i}$ on the dynamic response of the system, equation 2.90 is obtained. Notice that, even though the eigenvalues and the eigenvectors are complex conjugate pairs, once the dynamic response is mathematically manipulated it only presents a real component. This function of time is graphically represented in Figure 2.6 for both a positive and negative value of $\mathfrak{Re}(\Omega)$.

$$\mathbf{d} = \begin{bmatrix} \delta_1 & 0 & 0 \\ 0 & \delta_2 & 0 \\ 0 & 0 & \delta_3 \end{bmatrix} \mathbf{q} \cdot e^{t \cdot \Omega}, \mathbf{v} = \begin{bmatrix} \delta_1 & 0 & 0 \\ 0 & \delta_2 & 0 \\ 0 & 0 & \delta_3 \end{bmatrix} \mathbf{y} \cdot e^{t \cdot \Omega} \tag{2.89}$$

$$\begin{aligned}
\frac{1}{2}q_i \cdot e^{t\cdot[\mathfrak{Re}(\Omega)+\mathfrak{Im}(\Omega)]} + \frac{1}{2}\overline{q_i} \cdot e^{t\cdot[\mathfrak{Re}(\Omega)-\mathfrak{Im}(\Omega)]} &= \\
= \frac{1}{2}e^{t\cdot\mathfrak{Re}(\Omega)}\left[\mathfrak{Re}(q_i)\cdot e^{i\cdot\mathfrak{Im}(\Omega)\cdot t} + i\cdot\mathfrak{Im}(q_i)\cdot e^{i\cdot\mathfrak{Im}(\Omega)\cdot t}\right] &+ \\
+\frac{1}{2}e^{t\cdot\mathfrak{Re}(\Omega)}\left[\mathfrak{Re}(q_i)\cdot e^{-i\cdot\mathfrak{Im}(\Omega)\cdot t} - i\cdot\mathfrak{Im}(q_i)\cdot e^{-i\cdot\mathfrak{Im}(\Omega)\cdot t}\right] &= \\
= e^{t\cdot\mathfrak{Re}(\Omega)}\left[\mathfrak{Re}(q_i)\cdot cos(\mathfrak{Im}(\Omega)\cdot t) - \mathfrak{Im}(q_i)\cdot sin(\mathfrak{Im}(\Omega)\cdot t)\right] &= \\
= e^{t\cdot\mathfrak{Re}(\Omega)}\left[\sqrt{(\mathfrak{Re}(q_i))^2+(\mathfrak{Im}(q_i))^2}\cdot cos\left(\mathfrak{Im}(\Omega)\cdot t + arctan\left(\frac{\mathfrak{Im}(q_i)}{\mathfrak{Re}(q_i)}\right)\right)\right]&
\end{aligned} \tag{2.90}$$

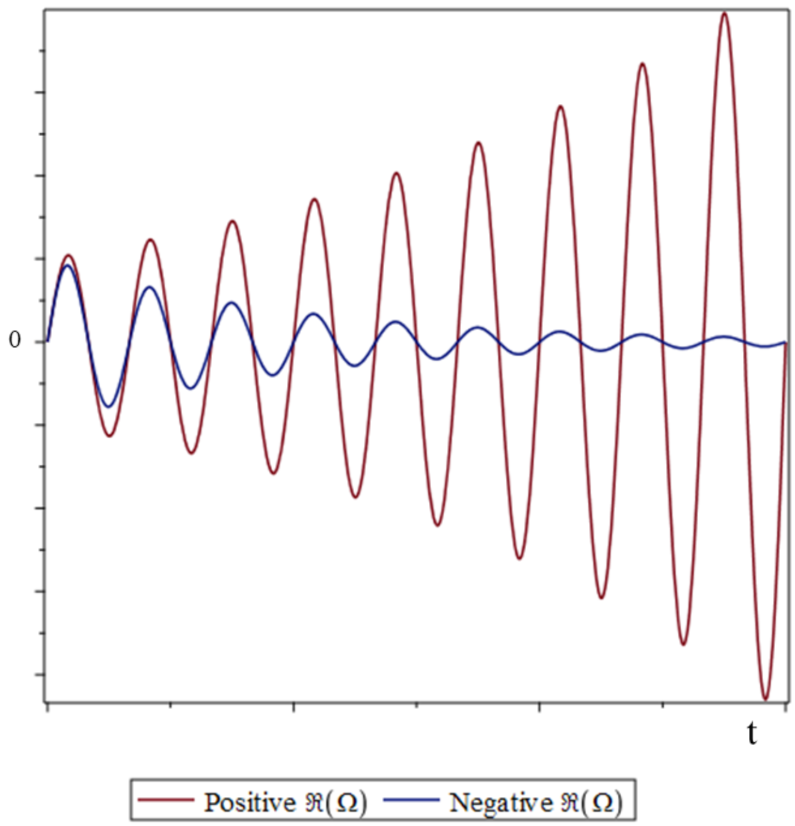

Figure 2.6: Plot of the $e^{t\cdot\mathfrak{Re}(\Omega)}\left[\sqrt{(\mathfrak{Re}(q_i))^2+(\mathfrak{Im}(q_i))^2}\cdot cos\left(\mathfrak{Im}(\Omega)\cdot t + arctan\left(\frac{\mathfrak{Im}(q_i)}{\mathfrak{Re}(q_i)}\right)\right)\right]$ function, for a positive $\mathfrak{Re}(\Omega)$ and for a negative $\mathfrak{Re}(\Omega)$.

It is concluded that the real part of the eigenvalues affects the damping of the system and the dynamic response is stable as long as this value is negative. The imaginary part represents the frequency of the oscillating movement. Flutter occurs for flow conditions where the real component of at least one eigenvalue ω changes to a positive value. If the latter coincides with a zero frequency eigenvalue, the structure becomes statically unstable. This phenomenon is called divergence [69].

A numerical analysis is done on the critical free flow static pressure state for the occurrence of flutter for various fiber paths of VSCL cylindrical shells. Still, a relation between the free flow stream pressure and flow velocity U can be established, as a consequence of $U = M \cdot a_\infty$ and $a_\infty = \sqrt{\gamma \cdot p_\infty / \rho_{fluid}}$. The term ρ_{fluid} corresponds to the specific mass of the fluid [61].

2.11 Conclusion

In this section, a linear mathematical model for thin circular cylindrical shells is developed, and then implemented on the software *Maple* recurring to a p-version FEM.

Firstly, the kinematic assumptions and relations are described. The constitutive model for a composite laminate is defined, where the coefficients A_{ij}, B_{ij} and D_{ij} arise and describe the elastic properties of the structure. For variable stiffness laminates, these coefficients become a function of the spacial axial variable. With these defined, the equations of motion which relate the internal forces of the structure, the body's inertia and the applied external forces are obtained. Clamped edges and simply supported edges are considered as the two alternatives for the sets of boundary conditions.

A p-version of the finite element method is implemented. The Galerkin method is used to obtain the needed matrices and the used shaped functions are obtained by the combination of 3 sets of shape functions.

The external aerodynamic forces applied to the cylindrical shell are modelled recurring to the piston theory. Supersonic airflow is considered. Implementing these forces on the FEM model, two matrices arise - the matrix of aerodynamic stiffness and the matrix of aerodynamic damping that, as the name implies, affect the system's stiffness and damping.

With the FEM matrices defined, the eigenvalue problem to determine the natural frequencies and mode shapes of the structure in free vibration is explained, which is useful to understand the dynamic properties of the shells and to validate the model.

Then, the eigenvalue problem of flutter is also described. The obtained eigenvalues present a real part that relates to the dynamic response's damping and an imaginary part that corresponds to the frequency. The flutter condition is found by varying free stream static pressure p_∞ until one of the eigenvalues obtained possess a positive real part of the eigenvalue. A relation between the critical free stream static pressure for the occurrence of flutter and the critical airflow speed can be made.

Thus, the model is defined and needs to be validated by comparing obtained results with those found in the literature.

Chapter 3

Model Validation

3.1 Introduction

In this chapter, the previously developed model is tested and compared to results found in the literature under different conditions and scenarios. The mathematical model was implemented on the software *Maple*.

Firstly, convergence test results are analyzed. Then an analysis of the obtained values for the natural frequencies and mode shapes under free vibration is done, as the comparison of these values with the vast set of options found in the literature presents a convenient method to validate the built FEM matrices. Only CSCL shells were analyzed in this process. Secondly, flutter results are compared with those in the literature.

Having the free vibration and the flutter phenomena tested individually allows to certify that the FEM matrices are reliably built and that the effect of the supersonic airflow on VSCL shells can be studied.

3.2 Convergence Test

As it is a standard operation for any FEM application, a convergence test is made with the intention of understanding the needed number of shape functions on the process so the results converge to a stable solution. This is a good practice that also avoids using an excessive number of shape functions, which in this case is additionally important, as when dealing with VSCL structures, the processing time of the FEM process becomes significantly bigger. For these tests, the fundamental frequency for the free vibration of a three layered cross ply [0º/90º/0] cylindrical shell is studied with C-C boundary conditions and the following parameters: $R = 1$ m, $l/R = 5$, $h/R = 0.002$, $E_{22} = 7.6$ GPa, $E_{11}/E_{22} = 2.5$, $G_{12} = 4.1$ GPa, $\nu_{12} = 0.26$, $\rho = 1643$ kg/m^3.

Different sets of shape functions are used and then combined: the g set, which approximates the axial variation of the membrane displacement u_0 and v_0; the f set, which represents the axial variation of the out-of-plane displacement w_0; and the h set which represents the angular variation of the displacements and is subdivided into $h_u = h_w$ (cosine functions for the u_0 and the w_0 displacement) and into h_v (sine functions for the v_0 displacement). For each FEM process, the number of used shape functions of each set is independently chosen. The number of shape functions used from the g set is pm, from the f set is po and from the h set is pt.

Table 3.1: Convergence study of the lowest natural frequency ω_1 for a three layered, cross-ply [0º/90º/0º] circular cylindrical shell with C-C boundary conditions ($R = 1$ m, $l/R = 5$, $h/R = 0.002$, $E_{22} = 7.6$ GPa, $E_{11}/E_{22} = 2.5$, $G_{12} = 4.1$ GPa, $\nu_{12} = 0.26$, $\rho = 1643$ kg/m^3).

pm	*po*	*pt*	ω_1 [Hz]	*DIF%*
4	4	4	34.8120	170.9
7	7	7	13.0928	1.841
10	10	10	12.8672	0.086
13	13	13	12.8583	0.017
16	16	16	12.8561	0
pm	*po*	*pt*	ω_1 [Hz]	*DIF%*
4	14	14	12.8661	0.078
7	14	14	12.8600	0.030
10	14	14	12.8593	0.025
14	14	14	12.8583	0.017
pm	*po*	*pt*	ω_1 [Hz]	*DIF%*
14	4	14	12.8914	0.275
14	7	14	12.8701	0.109
14	10	14	12.8643	0.064
14	14	14	12.8583	0.017
pm	*po*	*pt*	ω_1 [Hz]	*DIF%*
14	14	4	22.0536	71.54
14	14	7	12.8584	0.018
14	14	10	12.8584	0.018
14	14	14	12.8583	0.017

Several convergence test results can be seen in Table 3.1. For the first convergence test it is considered that $pm = po = pt$. This value gradually increases until a small enough difference for the registered value of the fundamental frequency is achieved. Note that the relative difference between the values registered for $pm = po = pt = 13$ and $pm = po = pt = 16$ is of 0.0175%, so it is considered that the results have converged. The values of relative difference *DIF%* seen in the table are relative to the value corresponding to $pm = po = pt = 16$.

After this first test, the individual influence of the number of shape functions used from each set is studied. This is done by assuming a constant number of used shape functions for 2 sets and by varying the third, as to understand the minimum value needed from that set for results to converge. The calculated relative differences for each test are in comparison with the reference value for $pm = po = pt = 16$.

It is observed that for $pm = 10$ and $po = pt = 14$, a difference of 0.0249% is achieved, and for $pm = 7$ and $po = pt = 14$ it is of 0.0303%. These values are low and it is concluded that the influence of varying *pm* is not big on the final result, for this particular mode.

As for varying the number of *po*, a bigger influence is noted. For $po = 14$ and $pm = pt = 14$, the difference is of 0.0171%, and for $po = 10$ and $pm = pt = 14$ it is of 0.0638%. It is concluded that results converge for bigger values of *po* than for *pm*.

Lastly, the influence of the value of *pt* is different than the other shape functions. Note that for $pt = 4$ and $pm = po = 14$, the obtained value is drastically different than those obtained in the other tests. Furthermore, a low difference in the natural frequency is observed for $pt = 7$, $pt = 10$ and $pt = 14$. This is because the fundamental natural frequency corresponds to a natural mode shape with 7 circumferential waves. Therefore, since the h set of shape functions consists on a set of cosine or sine functions, less than 7 shape functions are not enough to reliably approximate this mode shape and, thus, a high enough value for *pt* must be chosen to allow the natural mode shapes that are intended to be studied.

The previously showed results apply to shells with C-C boundary conditions. A similar procedure is done on a shell with the same parameters, but with S-S boundary conditions. Only the variation of *pm* and *po* is tested, since, only the g and f sets of shape functions present differences between C-C and S-S boundary conditions. The results can be seen in Table 3.2, where the values of relative difference *DIF%* are relative to the value of the fundamental natural frequency corresponding to $pm = po = pt = 13$.

Table 3.2: Convergence study of the lowest natural frequency ω_1 for a three layered, cross-ply [0º/90º/0º] circular cylindrical shell with S-S boundary conditions ($R = 1$ m, $l/R = 5$, $h/R = 0.002$, $E_{22} = 7.6$ GPa, $E_{11}/E_{22} = 2.5$, $G_{12} = 4.1$ GPa, $\nu_{12} = 0.26$, $\rho = 1643$ kg/m^3).

pm	*po*	*pt*	ω_1 [Hz]	*DIF%*
4	4	4	11.5694	31.04
7	7	7	8.8292	0.001
10	10	10	8.8291	0
13	13	13	8.8291	0
pm	*po*	*pt*	ω_1 [Hz]	*DIF%*
4	14	14	8.8309	0.020
7	14	14	8.8292	0.001
10	14	14	8.8291	0
14	14	14	8.8291	0
pm	*po*	*pt*	ω_1 [Hz]	*DIF%*
14	4	14	8.8296	0.006
14	7	14	8.8291	0
14	10	14	8.8291	0
14	14	14	8.8291	0

Comparing the convergence test results of the shell with S-S boundary conditions with the previous one, it can be seen that the results converge with a lower number of shape functions with S-S boundary conditions than with C-C boundary conditions.

The rest of the values obtained for this document take these convergence test results into consideration, and are obtained by choosing a number of shape functions that balances result accuracy and processing time.

3.3 Natural Frequencies and Mode Shapes of Vibration

In this section, values obtained for the free vibration of circular cylindrical shells by the implementation of the mathematical model described in this document are compared with values found in literature.

Both the natural frequencies and the natural mode shapes are obtained recurring to the p-FEM. In the following tests, m corresponds to the number of axial waves of a given natural mode shape, and n corresponds to the number of circumferential waves.

Table 3.3: Frequency parameters $\Omega = \omega R\sqrt{\rho/E_{22}}$ for a three layered, cross-ply [0º/90º/0º] circular cylindrical shell with C-C and S-S boundary conditions ($l/R = 5$, $h/R = 0.002$, $E_{22} = 7.6$ GPa, $E_{11}/E_{22} = 2.5$, $G_{12} = 4.1$ GPa, $\nu_{12} = 0.26$, $\rho = 1643$ kg/m^3, $m = 1$).

n	C-C Boundary Conditions			S-S Boundary Conditions			
	Present Work	Ref. [24]	Ref. [28]	Present Work	Ref. [24]	Ref. [19]	Ref. [16]
1	0.303168	0.303318	0.303609	0.248635	0.248637	0.248635	0.248634
2	0.166909	0.167166	0.167527	0.107203	0.107206	0.107203	0.107202
3	0.099194	0.099440	0.099667	0.055087	0.055090	0.055087	0.055085
4	0.064400	0.064607	0.064699	0.033790	0.033793	0.033790	0.033788
5	0.046171	0.046322	0.046345	0.025794	0.025796	0.025794	0.025790
6	0.038128	0.038233	0.038222	0.025877	0.025878	0.025877	0.025873

Table 3.3 compares the adimensional frequency parameter $\Omega = \omega R\sqrt{\rho/E_{22}}$ for a constant stiffness, cross ply shell with clamped edges and with simply supported edges with the values seen in references [16,19,24,28]. The natural mode shapes corresponding to that test are plotted in Figure 3.1, for the clamped edges case. In this dissertation, the shells' mode shapes are graphically represented in a Cartesian system of coordinates, where the vertical axis corresponds to the ξ coordinate of the cylindrical coordinate system. Note that, comparing with Xie et. al [24], the biggest relative difference obtained in this study is of -0.3260% for $n = 5$ in a clamped shell. The difference in plots for the natural mode shapes with $m = 1$ and $n = 6$ with C-C boundary conditions and S-S boundary conditions can be seen in Figure 3.2. As it is expected, it is noticeable the absence of slope at the edges when these are clamped.

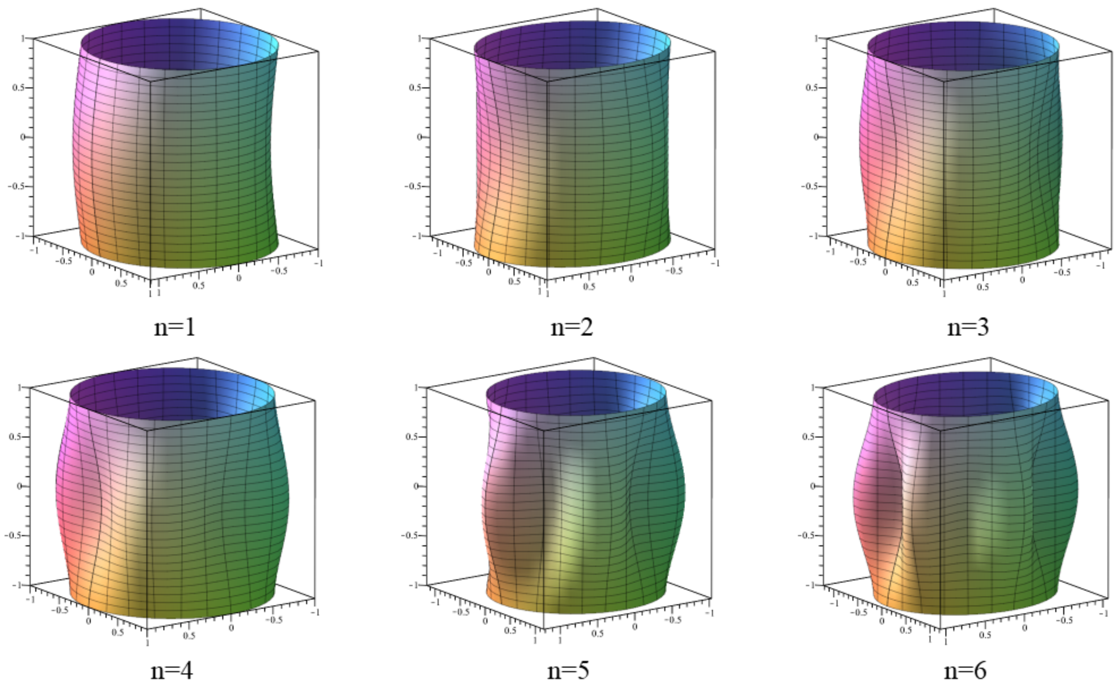

Figure 3.1: Natural mode shapes of a three layered, cross-ply [0º/90º/0º] circular cylindrical shell with C-C boundary conditions ($R = 1$, $l/R = 5$, $h/R = 0.002$, $E_{22} = 7.6$ GPa, $E_{11}/E_{22} = 2.5$, $G_{12} = 4.1$ GPa, $\nu_{12} = 0.26$, $\rho = 1643$ kg/m^3, $m = 1$).

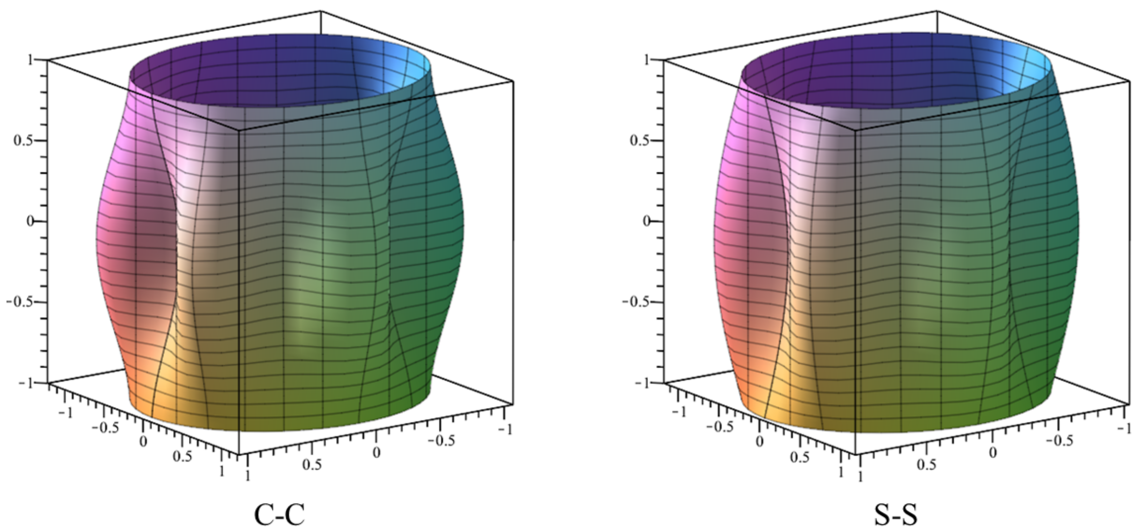

Figure 3.2: Comparison of the plot of the mode shapes with $m = 1$ and $n = 6$ for a cross ply [0º/90º/0º] circular cylindrical shell with C-C and S-S boundary conditions ($R = 1$ m, $l/R = 5$, $h/R = 0.002$, $E_{22} = 7.6$ GPa, $E_{11}/E_{22} = 2.5$, $G_{12} = 4.1$ GPa, $\nu_{12} = 0.26$, $\rho = 1643$ kg/m^3).

Table 3.4: Frequency parameters $\Omega = \omega R\sqrt{\rho/E_{22}}$ of the fundamental natural frequency for a four layered, angle-ply circular cylindrical shell with C-C and S-S boundary conditions ($l/R = 4$, $h/R = 0.01$, $E_{11}/E_{22} = 20$, $G_{12}/E_{22} = 0.65$, $\nu_{12} = 0.25$).

Lamination	C-C Boundary Conditions			S-S Boundary Conditions		
	Present Work	Ref. [14]	Ref. [77]	Present Work	Ref. [14]	Ref. [77]
$[+30^o/-30^o]_s$	0.1827	0.1818	0.1827	0.1237	0.1233	0.1232
$[+45^o/-45^o]_s$	0.1768	0.1760	0.1789	0.1196	0.1195	0.1193
$[+60^o/-60^o]_s$	0.1801	0.1780	0.1796	0.1097	0.1094	0.1093

Results obtained in these tests are in accordance with those found in the bibliographic references and therefore the model is validated for constant stiffness cross ply laminates. However, in this kind of structure, the material coefficients A_{16}, A_{26}, , D_{16} and D_{26} (these coefficients are explained in section 2.4) are equal to 0 and, for a generic balanced, symmetric, angle ply laminate these terms might not be 0. Considering this, tests are made for this kind of structure and the results are in Table 3.4 for both cases of clamped and simply supported shells, compared with the values seen in the work of Timarci & Soldatos [14] and Narita et. al [77]. The frequency parameters Ω are calculated for the the first natural mode of three cases of four layered angle ply cylindrical shells: $[+30^o/-30^o]_s$, $[+45^o/-45^o]_s$ and $[+60^o/-60^o]_s$; with the following parameters: $l/R = 4$, $h/R = 0.01$, $E_{11}/E_{22} = 20$, $G_{12}/E_{22} = 0.65$, $\nu_{12} = 0.25$.

Comparing the values obtained in this study seen in Table 3.4 with those obtained by Narita et. al [77], the biggest difference in fundamental frequency obtained is of -1.17%. Therefore, satisfactory results have been achieved for both boundary conditions and it is possible to proceed to the validation of the flutter implementation on the model.

It should, however, be noted that the variable stiffness properties have not been compared with other works, since articles that displayed the results of the natural frequencies of cylindrical shells under the same geometric conditions of variable stiffness and with boundary conditions that the developed model could reliably represent were not found.

3.4 Supersonic Flutter

In this section, multiple FEM tests are performed on cylindrical shells under an axial supersonic flow of air. The goal is to compare the critical values of free stream static pressure p_{crit} that result in the occurrence of aerodynamic flutter with those found in the works of other authors.

Table 3.5: Critical free stream pressure p_{crit} (Pa) for the occurrence of flutter for S-S boundary conditions of circular cylindrical shells with the following parameters: $G_{12} = E_{11}/[2 \cdot (1+\nu_{12})]$, $h = 0.0001015$ m, $R = 0.203$ m, $\rho = 8900$ kg/m^3, $M = 3$, $a_\infty = 213$ m/s, $\gamma = 1.4$.

1^{st} test

$l = 0.381$ m, $\nu_{12} = 0.35$, $E_{11} = E_{22} = 110 \cdot 10^9$ GPa

Present Work		Ref. [59]		Ref. [55]		Ref. [78]	
p_{crit} [Pa]	n_{crit}	p_{crit} [Pa]	n_{crit}	p_{crit} [Pa]	n_{crit}	p_{crit} [Pa]	n_{crit}
3867	25	3875	26	3599	26	3792	25

2^{nd} test

$l = 0.406$ m, $\nu_{12} = 0.33$, $E_{11} = E_{22} = 89 \cdot 10^9$ GPa

Present Work		Ref. [58]		Ref. [55]	
p_{crit} [Pa]	n_{crit}	p_{crit} [Pa]	n_{crit}	p_{crit} [Pa]	n_{crit}
2727	25	2896	24	2633	25

Two tests are performed. For the first one, a comparison is done with the numerical tests found in references [55,59,78] for an isotropic shell with the following parameters: $E_{11} = E_{22} = 110 \cdot 10^9$ Pa, $\nu_{12} = 0.35$, $G_{12} = \frac{E_{11}}{2(1+\nu_{12})}$, $h = 0.0001015$ m, $l = 0.381$ m, $R = 0.203$ m, $\rho = 8900$ kg/m^3, $M = 3$, $a_\infty = 213$ m/s, $\gamma = 1.4$. Simply supported boundary conditions were considered, there is no structural damping and the number of used shape functions allowed up to $n = 27$ circumferential waves to be obtained on the flutter mode shapes. For the second test, the following parameters were considered: $E_{11} = E_{22} = 89 \cdot 10^9$ Pa, $\nu_{12} = 0.33$, $G_{12} = \frac{E_{11}}{2(1+\nu_{12})}$, $h = 0.0001015$ m, $l = 0.406$ m, $R = 0.203$ m, $\rho = 8900$ kg/m^3, $M = 3$, $a_\infty = 213$ m/s, $\gamma = 1.4$. Simply supported boundary conditions were used again and the results were compared with Sabri & Lakis [55] and Carter & Stearman [58]. Notice that the difference in parameters between the first and second test only affects l, ν_{12} and E_{11}. The flutter test results can be seen in Table 3.5, where the values of the critical free stream pressure p_{crit} are expressed, as well as the number of circumferential waves n_{crit} of the mode that first achieves flutter.

Analysing the results of Table 3.5 it can be seen that regarding the flutter results obtained by various authors, even though they are similar, some discrepancies usually exist between them. Not only the values of p_{crit} themselves do not tend to be exactly equal, the numbers of circumferential waves n_{crit} of the corresponding mode shapes also do not. However, the results obtained in this work are close with those found in the literature and with similar values of n_{crit}. The obtained maximum relative difference of p_{crit} is 7.4%. It can be seen that flutter tends to occur for mode shapes with a high number of circumferential waves, and that is kept in mind for the tests performed for this dissertation.

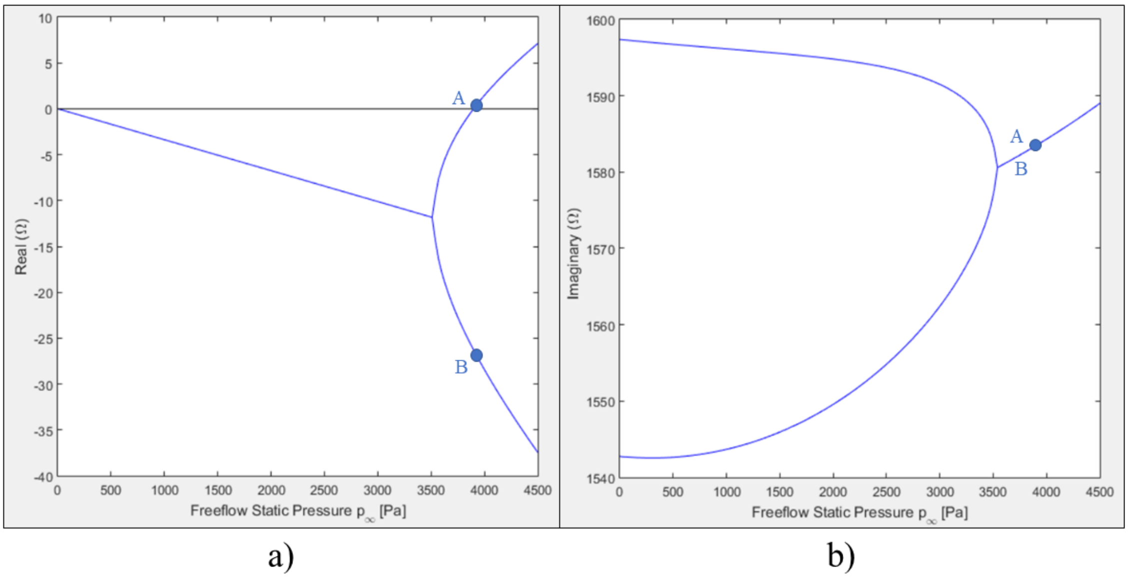

Figure 3.3: a) $\mathfrak{Re}(\Omega)$ and b) $\mathfrak{Im}(\Omega)$ variation along p_∞ of 2 modes of the first test.

It is relevant to analyse the variation of Ω with p_∞. Figures 3.3 a) and b) contain the the plots for $\mathfrak{Re}(\Omega)$ and $\mathfrak{Im}(\Omega)$, both obtained for the first performed test and are in relation to the variable p_∞, where two of the eigenvalues obtained by solving the eigenvalue problem are displayed. It is seen that one of the eigenvalues Ω has its real part $\mathfrak{Re}(\Omega)$ become positive after a certain value of p_∞, which corresponds to the critical free stream pressure of flutter p_{crit}. This happens for various modes at different values of p_∞, but the first mode to achieve flutter or divergence is the most important to analyse, since it brings instability to the system first.

It is observed that, for the flutter modes, there is a bifurcation in the $\mathfrak{Re}(\Omega)$ plot. In contrast, the values for $\mathfrak{Im}(\Omega)$ are distinct for low values of p_∞ and then converge at higher p_∞. The value of p_∞ at which this occurs corresponds to the value at which the values of $\mathfrak{Re}(\Omega)$ bifurcate. For convenience, the mode that results from the bifurcation of $\mathfrak{Re}(\Omega)$ of the critical flutter mode is referred to in this work as its corresponding coupled mode.

It should also be noted that, while analyzing the imaginary parts of all the eigenvalues, the generated plot (not shown here) is symmetric in relation to the p_∞ axis, as it should, since that for every eigenvalue exists its complex conjugate counterpart. Consequently, while analyzing the real part of the eigenvalues, for each value of $\mathfrak{Re}(\Omega)$ there exists another one with the exact same value.

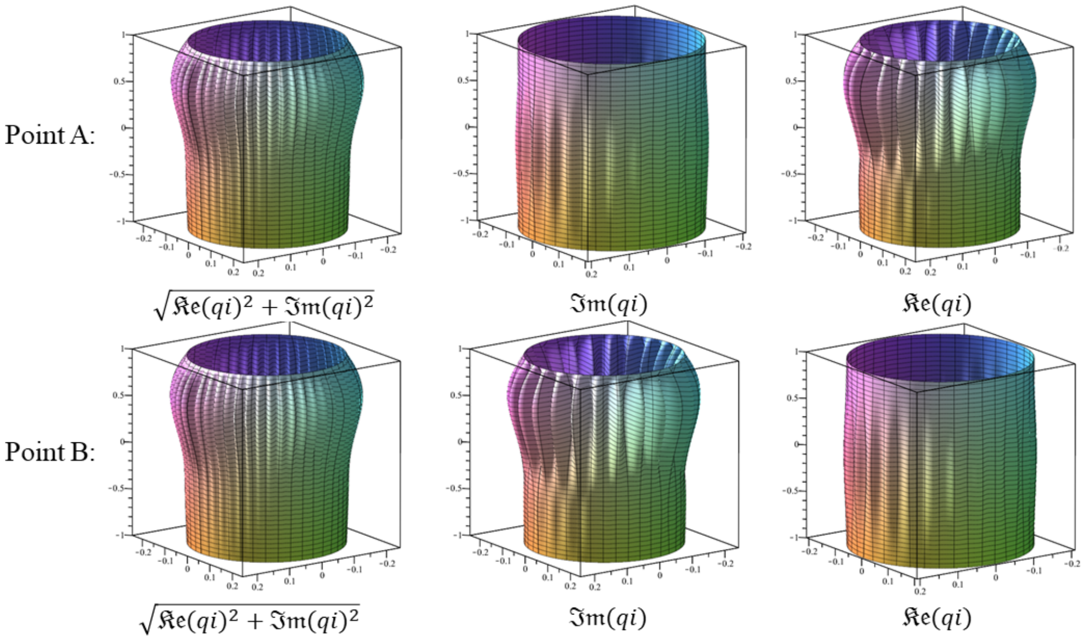

Figure 3.4: Flutter mode shapes corresponding to points A and B of the plot of the first flutter test ($n_{crit} = 25$).

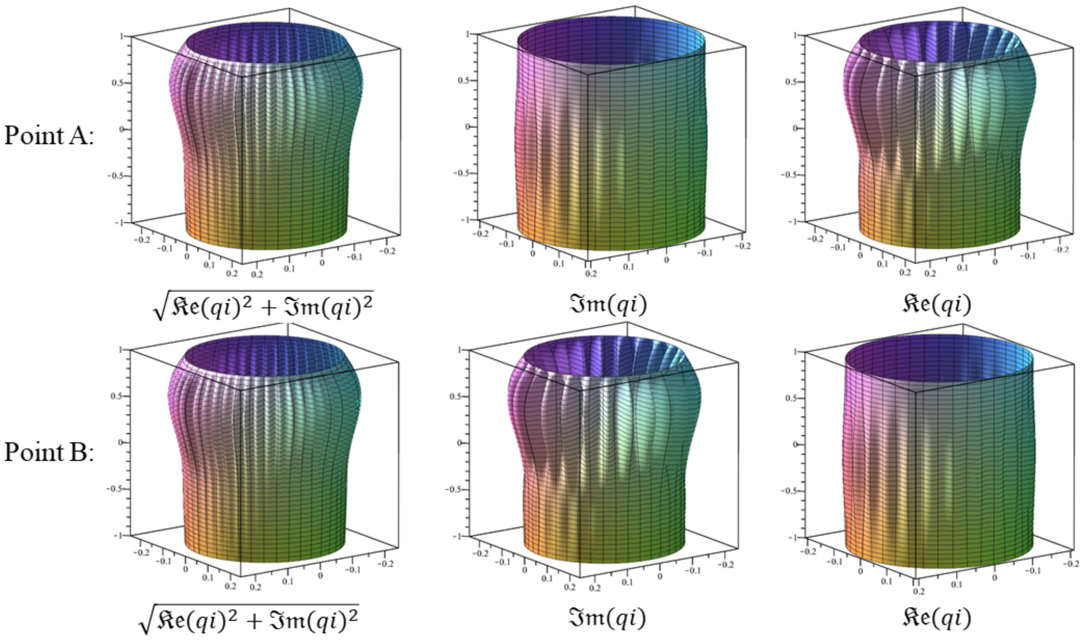

Figure 3.5: Flutter mode shapes corresponding to the complex conjugates of points A and B of the plot of the first flutter test ($n_{crit} = 25$).

Figure 3.3 contains two highlighted points: A and B that correspond to two different modes, at a free stream pressure of 3900 Pa. The real part $\mathfrak{Re}(q_i)$, the imaginary part $\mathfrak{Im}(q_i)$ and the amplitude $|q_i| = \sqrt{\mathfrak{Re}(q_i)^2 + \mathfrak{Im}(q_i)^2}$ (review equation 2.90) of both of these mode shapes are graphically represented for these two points in Figure 3.4. Figure 3.5 contains the same, but for the complex conjugates of the modes represented in Figure 3.4. In this dissertation, the parameter n_{crit} refers to the number of circumferential waves of the shape of the critical flutter mode shape, corresponding to the graphical representation of either its imaginary part or its real part.

In both points, and in both conjugate pairs of the eigenvectors, the graphical representation of the amplitude is similar. The main difference comes when analyzing the real part and the imaginary part of the eigenvectors. The shape of the real part of the eigenvector corresponding to point A is similar to the shape of the imaginary part of the eigenvector corresponding to point B, and vice-versa. Both the imaginary parts and the real parts of these mode shapes contain a wavy pattern, with n=25 waves in this case. The amplitude presents itself as a combination of the other 2 shapes, with axial asymmetry. Naturally, for the same point, the real part of the eigenvector is the same for both conjugate modes, and the imaginary part has the same shape, but with its displacement multiplied by -1.

Considering all this, the flutter phenomenon is behaving as expected and the implementation of the aerodynamic force in the model is validated.

3.5 Conclusions

In this chapter, convergence test results of the natural frequencies of cylindrical shells are displayed and a comparison of the natural frequencies between those obtained in this work and those found in literature is done. Finally, the critical free stream pressure for the occurrence of flutter is calculated and compared with those obtained by other authors. The obtained eigenvalues and eigenvectors that emerge from solving the mathematical equation that describes the dynamic response of a cylindrical shell to supersonic airflow are analyzed.

Regarding the convergence test, it is found that the p-FEM presents a quick conversion of values and the number of shape functions for which stable values are obtained is found. Attention must be payed to the number of used shape functions of the h set that corresponds to the variations of the u_0, v_0 and w_0 along the angular direction, since the number of circumferential waves that a vibration mode can have is dependent on this set. If it is intended to study a mode shape with $n = x$ circumferential waves and $pm < x$, then that mode is not reliably obtained. Additionally, it is found that shells with simply supported edges tend to converge to stable results with a fewer number of shape functions than shells with clamped edges, due to the differences in the used shape functions of the g and f set.

Regarding the comparison of fundamental frequencies, satisfactory results have been achieved. The main goal of these tests is to ensure that the stiffness and mass matrices are reliably calculated. Cross-ply and angle-ply laminates, both with C-C and S-S boundary conditions are validated. The main expected geometrical differences between shells with these different edge supports is seen in the natural mode shapes, as the shell with C-C boundary conditions does not present slope at the edges, and the one with S-S boundary conditions does.

Finally, the application of aerodynamic force modelled by the piston theory is tested, and the values at which flutter occurs are compared to those obtained by other authors. Results between authors present bigger differences than those found in the comparison of natural frequencies, however, close results to those found in the literature were obtained in these flutter tests. Furthermore, the obtained eigenvalues and eigenvectors present the expected properties. It is found that the critical flutter modes may correspond to mode shapes with a high number of circumferential waves and, therefore, this should be considered when choosing the number of shape functions used from the h set.

With all this in mind, it is concluded that the model is validated and that flutter on VSCL circular cylindrical shells can be tested and analyzed.

Chapter 4

Supersonic Flutter of Fiber Reinforced Composite Laminate Cylindrical Shells

4.1 Introduction

For this chapter, various fiber paths were tested, with the objective of finding curvilinear paths that enable an increase of the critical free stream static pressure p_{crit} associated with flutter.

Unless stated otherwise, it is considered that the circular cylindrical composite shell and the airflow have the properties stated in Table 4.1. These parameters were chosen to be similar to those found in references [55, 69]. There is no viscous or structural damping and the shell is composed by 12 balanced and symmetric layers $[\pm\psi]_s$, where the tow angle ψ might be constant or a function of the axial coordinate. These results are obtained recurring to the mathematical model described in chapter 2, where no manufacturing defects and material imperfections are considered.

Table 4.1: Shell and airflow parameters for the performed tests.

Young's Modulus E_{11}	126.3 GPa
Young's Modulus E_{22}	8.765 GPa
Shear Modulus G_{12}	4.92 GPa
Poisson's Ratio ν_{12}	0.334
Shell's Volumetric Mass ρ	1557 kg/m^3
Shell's Thickness h	0.0001015 m
Shell's Axial Length l	0.406 m
Shell's Radius R	0.203 m
Mach M	3.5
Air's Adiabatic Exponent γ	1.4
Air's Speed of Sound a_∞	213 m/s

4.2 Shells with Clamped Boundary Conditions

In this section, tests were performed to find lamination parameters for each fiber path that increased the value of p_{crit}, as to understand the advantage in the use of curved fiber paths on laminate structures exposed to supersonic airflow. C-C boundary conditions are considered.

Five fiber paths were tested: constant angle, linear variation of fiber orientation (with 1 and 2 segments) and constant in-plane curvature (with 1 and 2 segments). All these paths are mathematically defined in section 1.2.2.2.

As it is stated in section 1.2.2.1, fiber paths must have a turning radius r_ψ that respects a minimum value. This is important because it ensures that manufacturable structures can be produced and that manufacturing defects and mechanical properties deterioration are avoided. Therefore, in the performed tests, a minimum turning radius of 635 mm is considered (which is a typical value for the minimum turning radius of a 32 tow course with 3.175 mm wide tows [1]). In addition to that, to avoid problematic scenarios in manufacturing of the cylindrical shells with curvilinear fibers, the tow angle ψ at any point of the structure respects the condition $\psi \in$ [0º, 85º].

Also, as seen in section 3.4, flutter occurs for mode shapes with high numbers of circumferential waves, and, therefore, tests are performed with a number of shape functions that allow up to $n = 25$ circumferential waves. Furthermore, the number of shape functions used from the g and f set are, respectively, $pm = 8$ and $po = 8$. Considering the high number of tests performed for this work, these parameters were chosen to achieve an acceptable balance between processing time and result accuracy. It should, however, be noted that mode shapes with extremely high number of circumferential waves (more than 25) and of axial waves ($pm = po = 8$ allows significantly more than 8 axial waves) are not reliably represented.

Lastly, to calculate the critical free stream pressure p_{crit} at which flutter occurs, plots are developed where the eigenvalues Ω of the problem are calculated for various values of p_∞. The eigenvalue problem is solved for values of p_∞ with a resolution of 20 Pa. Therefore, calculations are made for the set of $p_\infty \in \{0$ Pa, 20 Pa, 40 Pa, 60 Pa, 80 Pa, 100 Pa, ...$\}$. Then a linear interpolation is made between the calculated values to find Ω for any p_∞.

The process adopted to find fiber paths that increase the value of p_{crit} consists on an iterative one. Fiber path parameters T_0 and T_1 are progressively tweaked in search of increasing the values of p_{crit}. So, it should be kept in mind that, even though higher results of p_{crit} are obtained in this work, they are probably not the highest, and in the future an optimization process can be an interesting way to further improve the knowledge on the topic of this dissertation.

4.2.1 Constant Stiffness Composite Laminates

Firstly, the tow angle of a constant angle path that enables the biggest increase of p_{crit} was searched for. For these paths, the only parameter that exists is T_0. Various values of T_0 were tested, by varying it by 10º each time, and then, around the maximum values of p_{crit} obtained, T_0 was varied by 5º. The obtained results can be seen in Figure 4.1

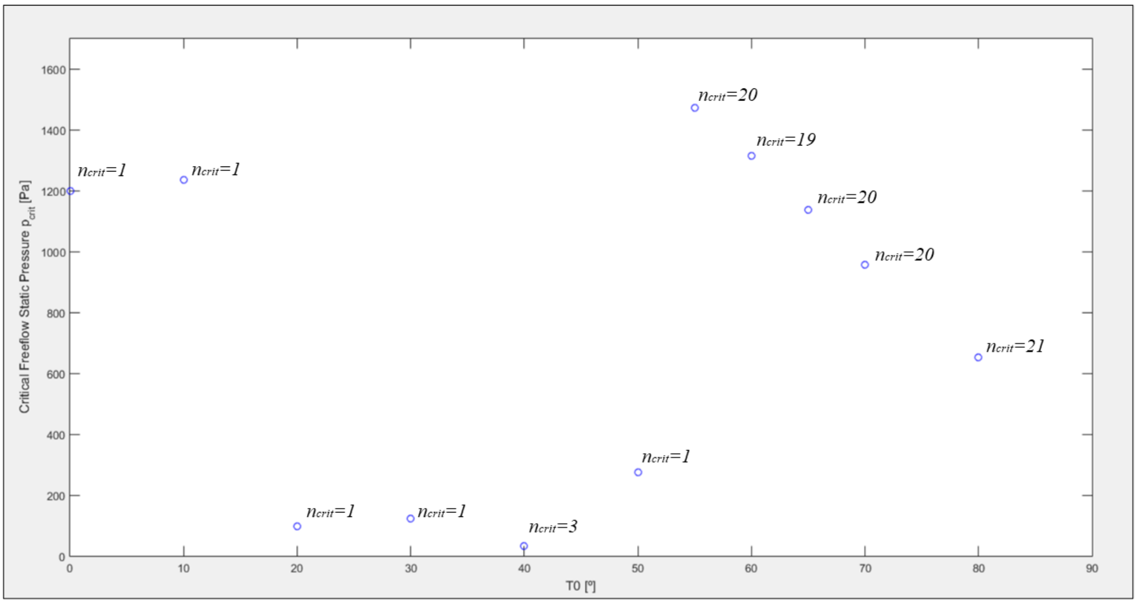

Figure 4.1: p_{crit} and n_{crit} for various values of T_0 of a CSCL cylindrical shell.

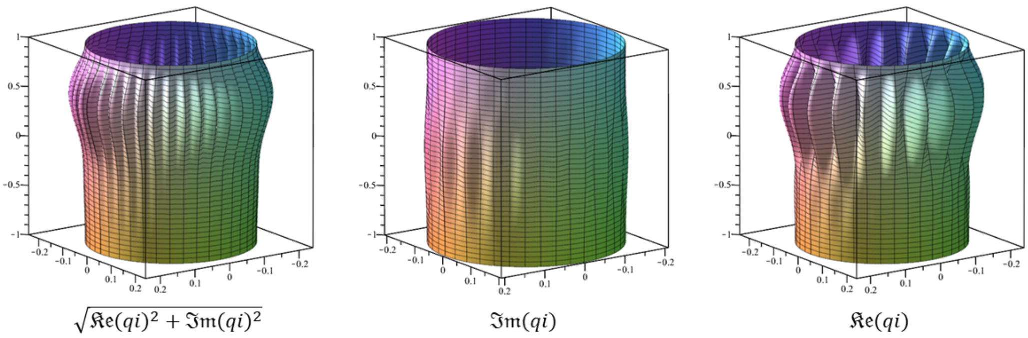

Figure 4.2: Critical flutter mode shape of a CSCL shell with $T_0 = 55^{\circ}$ ($n_{crit} = 20$).

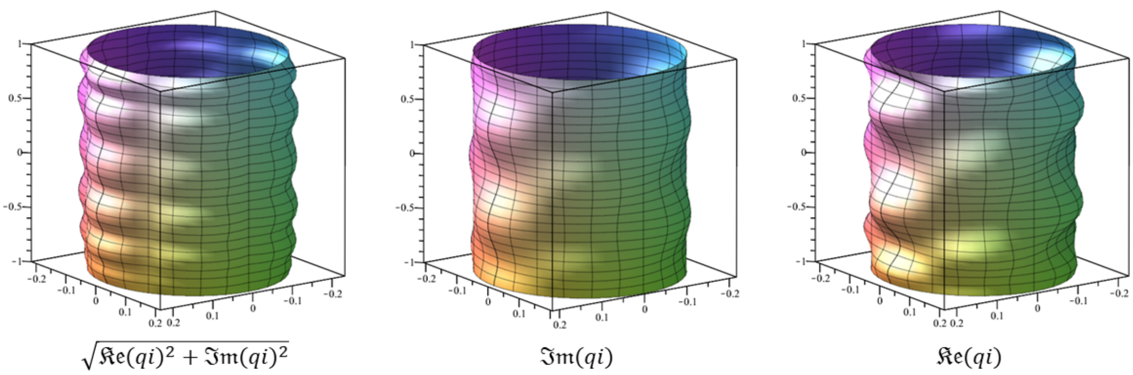

Figure 4.3: Critical flutter mode shape of a CSCL shell with $T_0 = 40^{\circ}$ ($n_{crit} = 3$).

A maximum value of $p_{crit} = 1474$ Pa was obtained for $T_0 = 55^{\circ}$. The corresponding flutter mode shape is graphically represented in Figure 4.2 and has a number of circumferential waves equal to $n_{crit} = 20$. On the other hand, the minimum value of pressure obtained is $p_{crit} = 32$ Pa for $T_0 = 40^{\circ}$, corresponding to a mode shape with a number of circumferential waves equal to $n_{crit} = 3$. This mode shape can be seen in Figure 4.3.

It is noticeable that a small change in tow angle can originate a significant difference in p_{crit}, which further illustrates how fiber reinforced composites give the designer more flexibility by allowing the tailoring of a structure's mechanical properties to the expected conditions. Additionally, it is seen that for different values of T_0, flutter can be achieved by modes with different numbers of circumferential and axial waves and with different shapes in general.

When dealing with curvilinear fiber paths, the value of $p_{crit} = 1474$ Pa is used as a benchmark, with the goal of finding tow paths that can surpass this value.

4.2.2 VSCL with Linear Angle Variation Paths: 1 Segment

The process of finding parameters for a curvilinear fiber path was an iterative one. Firstly, the linear angle variation type of fiber path is analyzed. A schematic representation of this type of path is seen in Figure 4.4.

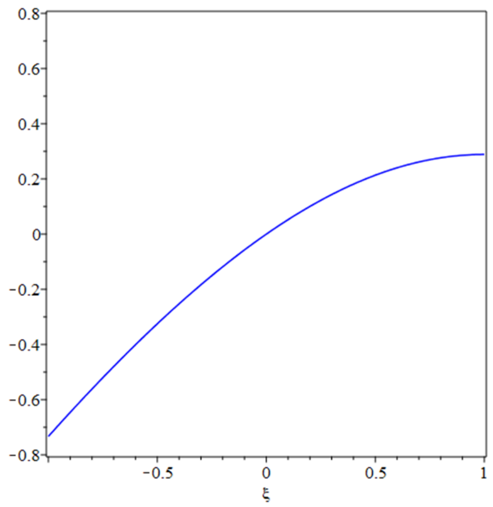

Figure 4.4: Linear angle variation path with 1 segment for $T_0 = 70^{\circ}$ and $T_1 = 0^{\circ}$.

Considering that the highest result found for a constant angle path corresponds to $T_0 = 55^{\circ}$, the starting parameters for the iteration process were <55º,55º> (which still corresponds to a constant angle fiber path). From there, parameter tweaks were progressively made in search for an increase of the value of p_{crit}. The results of the performed tests are in Table 4.2, along with the minimum turning radius r_{ψ} of each path.

Table 4.2: Critical free stream pressure p_{crit} for shells with linear angle variation fiber paths $<T_0,T_1>$.

$<T_0,T_1>$			
T_0[º]	T_1[º]	r_ψ[m]	p_{crit}[Pa]
55	55	———	1474
60	50	3.6189	1697
50	60	3.6189	1697
50	80	1.2063	1922
40	80	0.7592	**2368**
40	75	0.8676	2328
40	85	0.6748	2280
Inadmissible Paths ($r_\psi < 635$ mm):			
T_0[º]	T_1[º]	r_ψ[m]	p_{crit}[Pa]
30	80	0.5372	2805
20	80	0.4126	3237

Curvilinear fibers enabled an increase of p_{crit}. It is seen in Table 4.2 that the values of p_{crit} can be significantly affected by using curvilinear fibers. The biggest value is highlighted and corresponds to the <40º,80º> fiber path. Comparing the obtained value of $p_{crit} = 2368$ Pa to the biggest one obtained with a constant angle fiber path of 1474 Pa, a relative increase of 60.7% of the p_{crit} value is observed. The mode shape corresponding to the <40º,80º> fiber path is plotted in Figure 4.5. This mode shape contains $n_{crit} = 16$ circumferential waves.

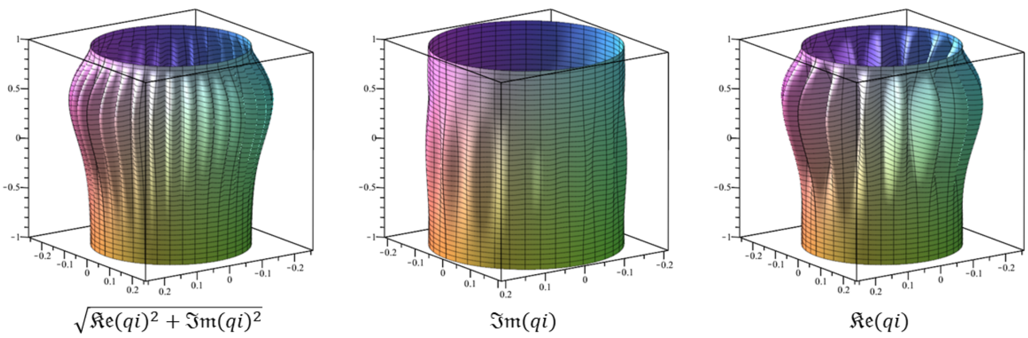

Figure 4.5: Critical flutter mode shape of a VSCL shell with a <40º,80º> fiber path ($n_{crit} = 16$).

As a test, the values of p_{crit} for <60º,50º> and <50º,60º> were calculated and the same result of $p_{crit} = 1697$ Pa was obtained. This is as expected, since the paths are equal, but symmetric.

Additionally, Table 4.2 also contains invalid paths that do not respect the minimum turning radius manufacturing constraint. From these paths, the biggest obtained value is $p_{crit} = 3287$ Pa, which further shows the potential of the variable stiffness concept on the improvement of the mechanical properties of laminates, even if it is from a theoretical perspective.

4.2.3 VSCL with Constant in-Plane Curvature Paths: 1 Segment

An increase in p_{crit} results has been achieved for the linear angle variation fiber paths and so, these results can be compared with those obtained by the constant in-plane curvature fiber paths. An example of this type of path is present in Figure 4.6.

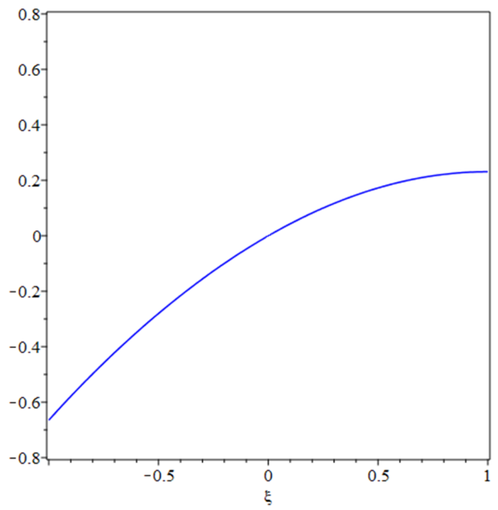

Figure 4.6: Constant curvature path with 1 segment for $T_0 = 70$º and $T_1 = 0$º.

The path parameters corresponding to the highest value of p_{crit} obtained for a linear angle variation fiber path was used as a starting point for the iterative procedure. The results obtained in these tests are in Table 4.3.

Table 4.3: Critical free stream pressure p_{crit} for shells with constant in-plane curvature paths $<T_0,T_1>_c$.

$<T_0,T_1>_c$			
T_0[º]	T_1[º]	r_ψ[m]	p_{crit}[Pa]
40	80	1.1871	2149
30	85	0.8182	2909
25	85	0.7078	**3164**
25	80	0.7222	3134

In Table 4.3, the value of p_{crit} for a $<40º,80º>_c$ tow path is present and equal to 2149 Pa. It is interesting to compare this value with the corresponding to a shell with the linear angle variation path of <40º,80º>, which is equal to $p_{crit} = 2368$ Pa. Naturally, even though the paths present the same T_0 and T_1 parameters, both have differences in their geometry which results in a relative difference of -8.8% in the achieved p_{crit}.

Analyzing Table 4.3, it can be seen that higher values were found for the constant in-plane curvature tow paths than for the linear angle variation paths. One factor that allows this is the fact that a bigger difference between T_0 and T_1 can be achieved using the constant in-plane curvature tow paths, since the manufacturing constraint less severely restricts this type of path. Therefore, for the same minimum turning radius allowed, these paths have more freedom on the parameter choices.

The highest value of p_{crit} obtained is highlighted and corresponds to the <25º,85º>$_c$ path. A value of $p_{crit} = 3164$ Pa was obtained, which corresponds to an increase of 114.7% of the biggest value obtained for a constant angle path. The flutter mode shape is graphically represented in Figure 4.7, which corresponds to a mode shape with $n_{crit} = 16$ circumferential waves, similarly to the one obtained in the <40º,80º> tow path.

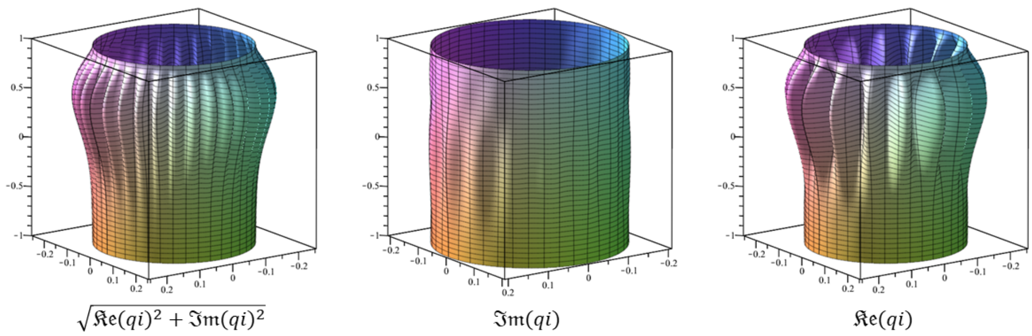

Figure 4.7: Critical flutter mode shape of a VSCL shell with a <25º,85º>$_c$ fiber path ($n_{crit} = 16$).

4.2.4 VSCL with Linear Angle Variation Paths: 2 Segments

Results were achieved for both linear angle variation paths and constant in-plane curvature fiber paths. However, the design flexibility of VSCL shells can be further improved by dividing the fiber path into different sections, each with its own shape and T_0 and T_1 parameters, as long as the continuity of the fiber is ensured. This concept is tested in this section, with paths with two anti-symmetric segments, as defined in section 1.2.2.2.

Firstly, tests were performed for fiber paths with two segments with linear angle variation $<T_1,T_0,T_1>$. An example of this type of path is seen in Figure 4.8. The obtained results are expressed in Table 4.4.

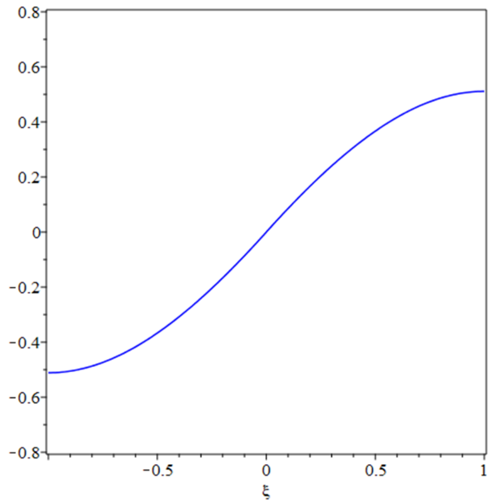

Figure 4.8: Linear angle variation path with 2 segments for $T_0 = 70°$ and $T_1 = 0°$.

Higher values of p_{crit} were achieved with the linear angle variation fiber paths with 1 segment. This is due to that fact that, while the fiber path allows to create more complex paths, the minimum turning radius manufacturing constraint further restricts the difference that the parameters T_0 and T_1 can have between them, which may not be beneficial to the structure's mechanical properties. For instance, for the parameters of $T_0 = 30°$ and $T_1 = 80°$, the fiber path with 1 segment has a minimum turning radius of $r_\psi = 537.2$ mm, while the path with 2 segments has a minimum turning radius of $r_\psi = 268.6$ mm, which is considerably lower.

Table 4.4: Critical free stream pressure p_{crit} for shells with linear angle variation fiber paths <T_1,T_0,T_1>.

<T_1,T_0,T_1>			
T_0[°]	T_1[°]	r_ψ[m]	p_{crit}[Pa]
30	50	0.6715	323
55	80	0.8111	1803
55	85	0.6759	**1816**
60	85	0.9305	1659
Inadmissible Paths ($r_\psi < 635$ mm):			
T_0[°]	T_1[°]	r_ψ[m]	p_{crit}[Pa]
80	30	0.2686	119
30	80	0.2686	2896

Table 4.4 contains inadmissible paths, due to their turning radius, that further illustrate this point. It is seen that for the path <80°,30°,80°> a value of $p_{crit} = 2896$ Pa was obtained, which is a higher result than those found for the paths with 1 segment. Unfortunately, as it was stated, the manufacturing of this path would likely result in defects, like tow out-of-plane buckling, that would harm the mechanical performance of the structure.

Analyzing the inadmissible paths, it is seen that different values of p_{crit} are obtained by swapping the values between T_0 and T_1, as it would be expected. In contrast with the fiber paths with 1 segment, fiber paths with 2 segments with swapped T_0 and T_1 parameters are not symmetric and, therefore, the obtained value of p_{crit} should not be the same.

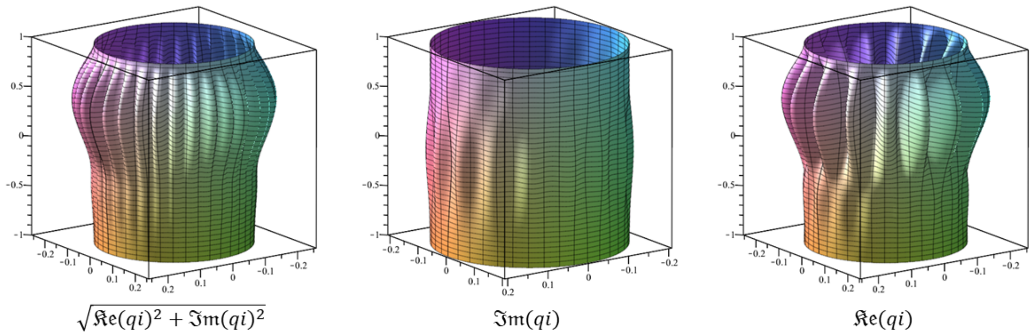

Figure 4.9: Critical flutter mode shape of a VSCL shell with a <85º,55º,85º> fiber path ($n_{crit} = 16$).

Regarding the admissible paths, the biggest value of p_{crit} was obtained for the <85º,55º,85º> fiber path, which is highlighted and corresponds to $p_{crit} = 1816$ Pa. This is equal to a relative increase of 23.2% regarding the highest obtained value of p_{crit} for the constant angle paths. The corresponding flutter mode shape is graphically represented in Figure 4.9, and it has $n_{crit} = 16$ circumferential waves.

4.2.5 VSCL with Constant in-Plane Curvature Paths: 2 Segments

Similarly to the previously tested fiber path, the constant in-plane curvature path can also be divided into 2 segments, as seen in Figure 4.10.

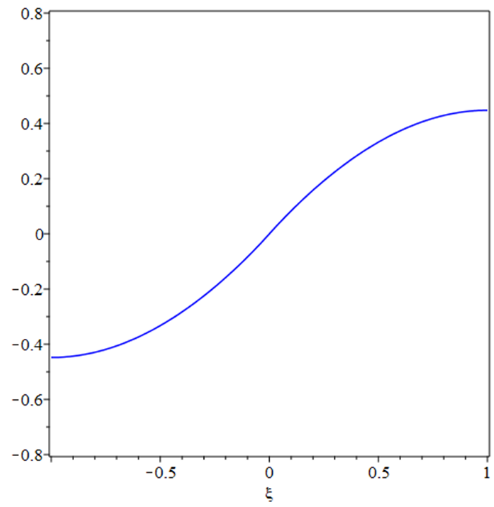

Figure 4.10: Constant curvature path with 2 segments for $T_0 = 70º$ and $T_1 = 0º$.

Table 4.5: Critical free stream pressure p_{crit} for shells with constant in-plane curvature fiber paths $<T_1,T_0,T_1>_c$.

$<T_1,T_0,T_1>_c$			
T_0[º]	T_1[º]	r_ψ[m]	p_{crit}[Pa]
55	85	1.1466	1779
45	85	0.7022	**2146**
45	80	0.7310	2136
50	85	0.8820	1953

The obtained results are present in Table 4.5, where the pattern observed in previous tests repeats itself. Comparing the constant in-plane curvature path with 1 and 2 segments, the one with 1 segment tends to yield higher values, due to the fact that the manufacturing constraint of the minimum turning radius, in the case of the path with 2 segments, restricts more severely the values that the T_0 and T_1 parameters can have. It is noticed that, in these cases, a bigger difference between the T_0 and T_1 parameters tends to increase the value of p_{crit}.

The values of p_{crit} of the $<85^\circ,55^\circ,85^\circ>_c$ fiber path and the $<85^\circ,55^\circ,85^\circ>$ path were calculated and compared. For the constant curvature one, the value of $p_{crit} = 1779$ Pa was obtained, which corresponds to a relative difference of -2.0% in relation to the one obtained for the linear angle variation path with 2 segments.

Even though the obtained value for the same parameters of T_0 and T_1 is lower for the constant in-plane curvature path than for the linear angle variation path (both with 2 segments), this type of path has a bigger flexibility in the definition of T_0 and T_1, which allowed to higher better overall results.

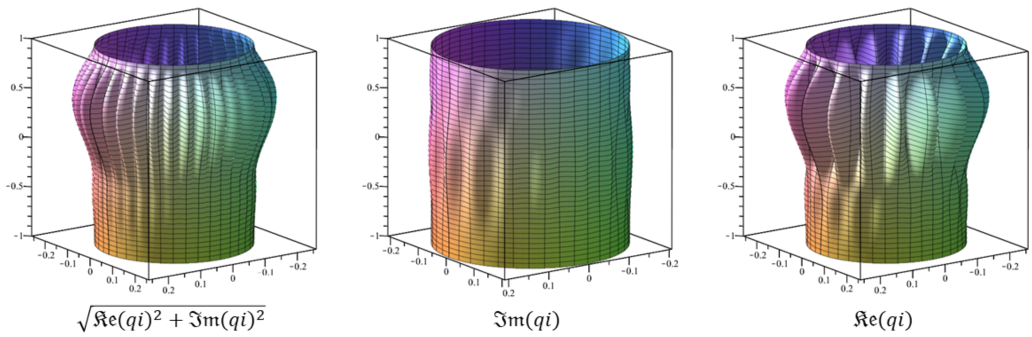

Figure 4.11: Critical flutter mode shape of a VSCL shell with a $<85^\circ,45^\circ,85^\circ>_c$ fiber path ($n_{crit} = 17$).

The biggest value of p_{crit} obtained for this type of path is highlighted in the Table and is equal to 2146 Pa. This value corresponds to the $<85^\circ,45^\circ,85^\circ>_c$ path, and its critical flutter mode shape has $n_{crit} = 17$ circumferential waves and is graphically represented in Figure 4.11.

4.2.6 Frequency Analysis

In the performed tests for clamped shells, a significant increase on the value of p_{crit} was achieved by the use of curvilinear fibers. In this section, the relation between the increase of p_{crit} and the imaginary part of the eigenvalues $\mathfrak{Im}(\Omega)$ for different paths is analyzed.

Ψ=55º:

<25º,85º>c :

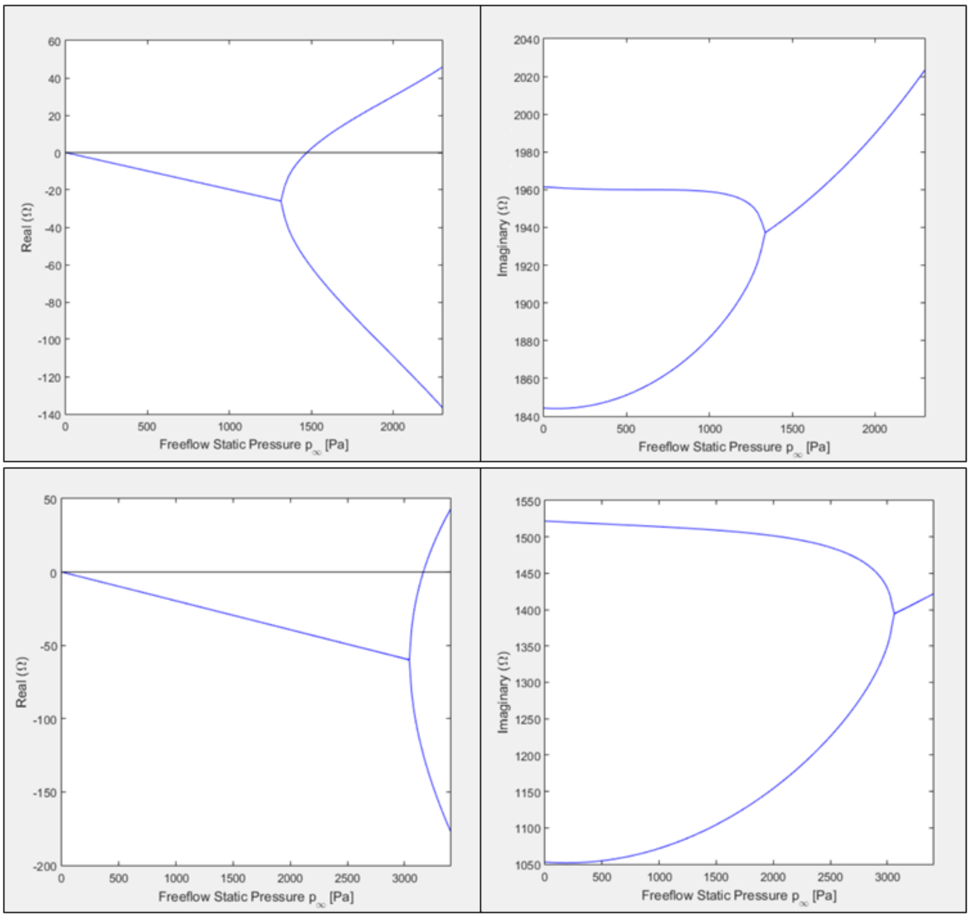

Figure 4.12: $\mathfrak{Re}(\Omega)$ and $\mathfrak{Im}(\Omega)$ variation along p_∞ of the critical flutter mode and its corresponding coupled mode for a shell $\psi = 55º$ tow path and a <25º,85º>$_c$ fiber path.

The highest obtained value of p_{crit} for a constant angle fiber path is $p_{crit} = 1474$ Pa and corresponds to the $\psi = 55º$ path. In all of the performed tests with curvilinear fibers, the one to obtain the biggest value of p_{crit} corresponds to the <25º,85º>$_c$ fiber path, with a value of $p_{crit} = 3164$ Pa and a relative increase of 114.7% in relation to the highest value obtained for a constant stiffness shell. These two fiber paths are chosen for the comparison of mode frequencies.

Figure 4.12 contains the $\mathfrak{Re}(\Omega)$ and $\mathfrak{Im}(\Omega)$ plots along p_∞ of the critical flutter mode and its corresponding coupled mode of the shells with these two paths. In the $\mathfrak{Im}(\Omega)$ plot, the evolution of the frequency of the modes with p_∞ can be analyzed. As expected, the frequencies of the modes start at different values and, at a higher value of p_∞, they converge. For $p_\infty = 0$ Pa, the value of $\mathfrak{Im}(\Omega)$ corresponds to the value of the natural frequencies of the shell under free vibration, since, for this value of free stream static pressure, the aerodynamic pressure that externally acts on the shell is null.

The natural frequencies of these modes are equal to 1844 rad/s and 1961 rad/s for the CSCL shell, and they are equal to 1052 rad/s and 1522 rad/s on the VSCL shell. It is noticeable that the difference of these values is significantly higher for the VSCL shell. This higher difference results in higher values of p_{crit}, since, in the $\mathfrak{Im}(\Omega)$ plot, the values start further apart and, therefore, require a higher value of p_∞ to converge. The natural mode shapes under free vibration of all these cases are represented in Figures 4.13-4.16.

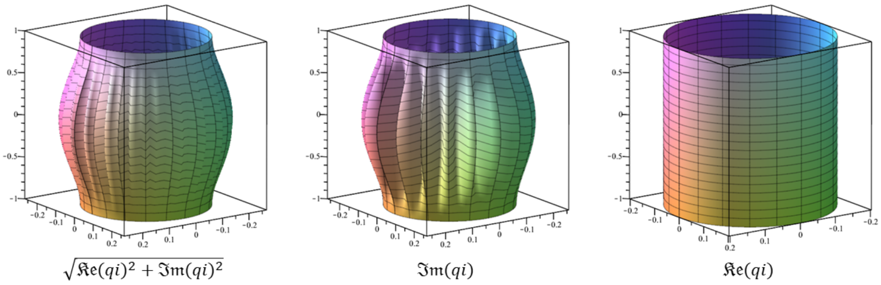

Figure 4.13: Natural mode shape of free vibration corresponding to $\omega = 1844$ rad/s of a CSCL shell with $\psi = 55^o$.

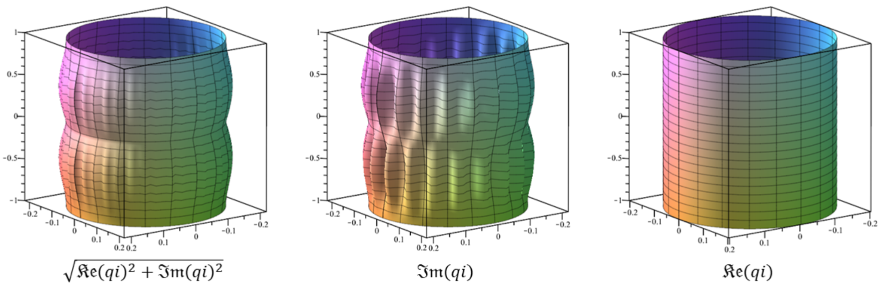

Figure 4.14: Natural mode shape of free vibration corresponding to $\omega = 1961$ rad/s of a CSCL shell with $\psi = 55^o$.

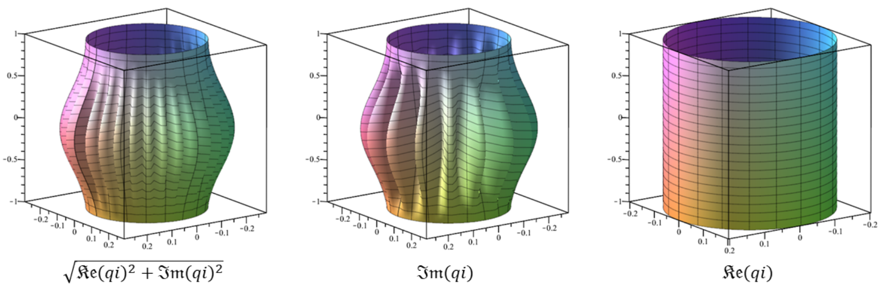

Figure 4.15: Natural mode shape of free vibration corresponding to $\omega = 1052$ rad/s of a VSCL shell with the <25º,85º>$_c$.

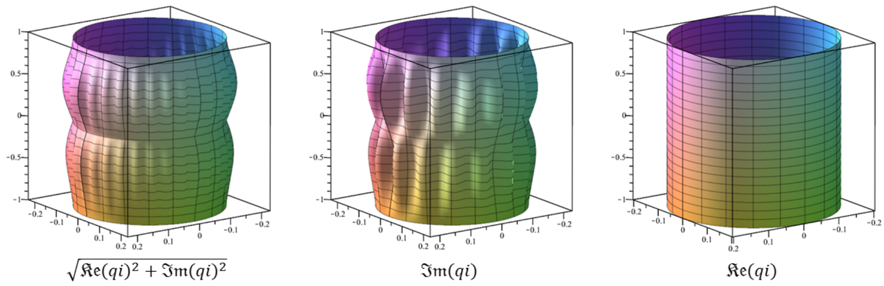

Figure 4.16: Natural mode shape of free vibration corresponding to $\omega = 1522$ rad/s of a VSCL shell with the <25º,85º>$_c$.

The analyzed natural mode shapes under free vibration present differences between them. Therefore, the fiber paths can be adjusted to differently influence the frequencies of these modes, enabling an increase of difference of the natural frequencies of vibration of the modes that are involved in the flutter phenomenon.

4.3 Simply Supported Boundary Conditions Comparison

In this section, the highest values of p_{crit} obtained for each type of fiber path with clamped edges are compared to the same paths with the same parameters, but with simply supported edges. The goal is not to find the fiber paths with the highest possible values of p_{crit} with these boundary conditions, but to understand how the difference in boundary conditions affects the values of p_{crit} and the associated graphical representation of the flutter mode shapes.

Tests were performed for the same shell and airflow parameters and only the boundary conditions were changed. Regarding the number of shape functions used, up to $n = 25$ circumferential waves are allowed and $pm = po = 8$. The obtained results can be seen in Table 4.6.

Table 4.6: Critical free stream pressure p_{crit} and number of circumferential waves of the corresponding mode n_{crit} for shells with C-C and S-S boundary conditions.

Fiber Path	C-C Boundary Conditions		S-S Boundary Conditions	
	n_{crit}	p_{crit} [Pa]	n_{crit}	p_{crit} [Pa]
$\psi = 55º$	20	1474	18	1065
<40º,80º>	16	2368	14	2111
<25º,85º>$_c$	16	3164	14	2870
<85º,55º,85º>	16	1816	15	1426
<85º,45º,85º>$_c$	17	2146	15	1708

It is generally seen that the values of p_{crit}, for the same fiber path, tend to decrease in shells with simply supported edges, and it is seen that the critical flutter mode shape tends to be different shape, with a distinct number of circumferential waves. Figures 4.17, 4.18, 4.19, 4.20 and 4.21 contain the graphical representation of the critical flutter mode shapes of the shells with S-S boundary conditions and with the $\psi = 55º$, the <40º,80º>, the <25º,85º>$_c$, the <85º,55º,85º> and the <85º,45º,85º>$_c$ paths, and they can be compared with Figures 4.2, 4.5, 4.7, 4.9 and 4.11 for their shell counterpart with C-C boundary conditions, respectively.

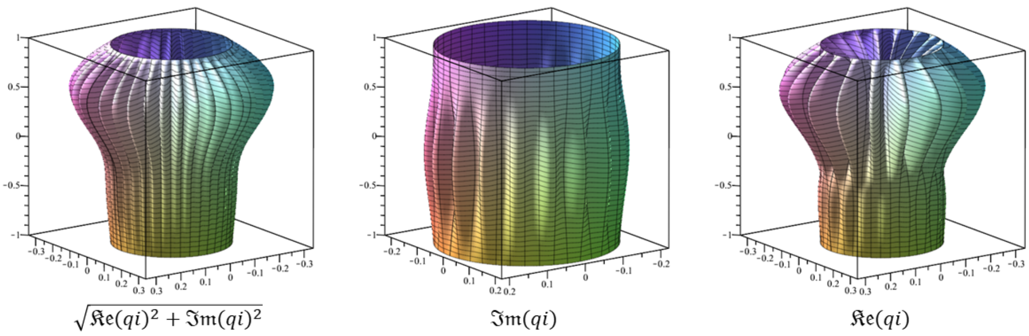

Figure 4.17: Critical flutter mode shape of a CSCL shell with $T_0 = 55º$ and S-S boundary conditions ($n_{crit} = 18$).

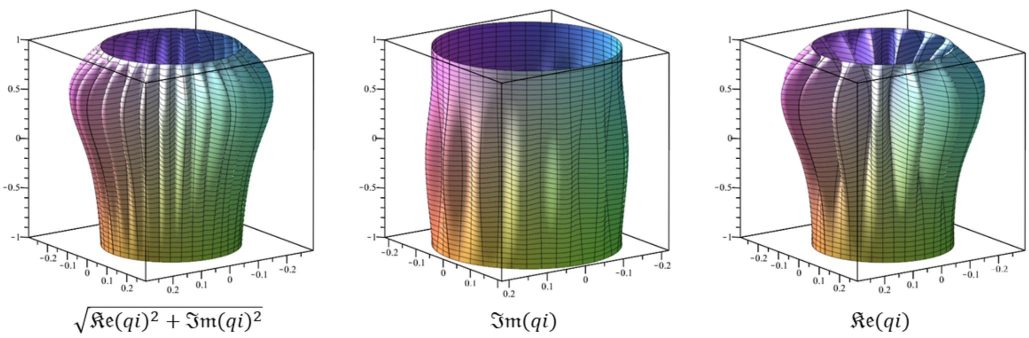

Figure 4.18: Critical flutter mode shape of a VSCL shell with a <40º,80º> tow path and S-S boundary conditions ($n_{crit} = 14$).

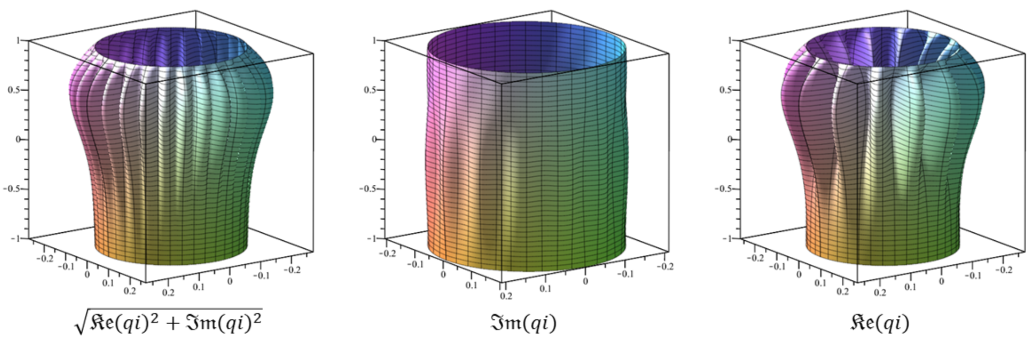

Figure 4.19: Critical flutter mode shape of a VSCL shell with a <25º,85º>$_c$ tow path and S-S boundary conditions ($n_{crit} = 14$).

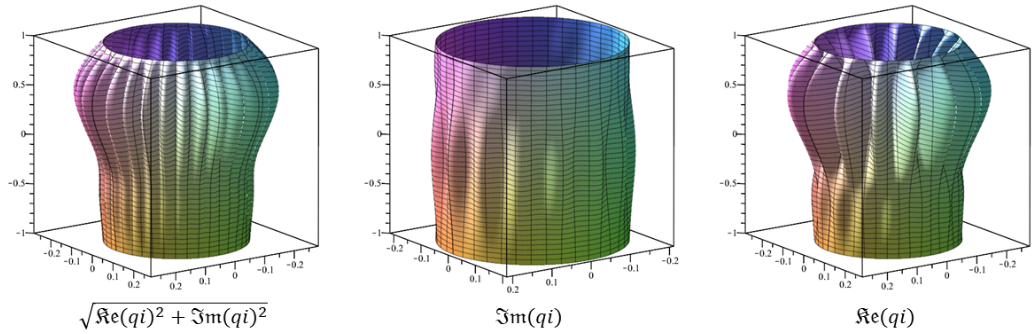

Figure 4.20: Critical flutter mode shape of a VSCL shell with a <85º,55º,85º> tow path and S-S boundary conditions ($n_{crit} = 15$).

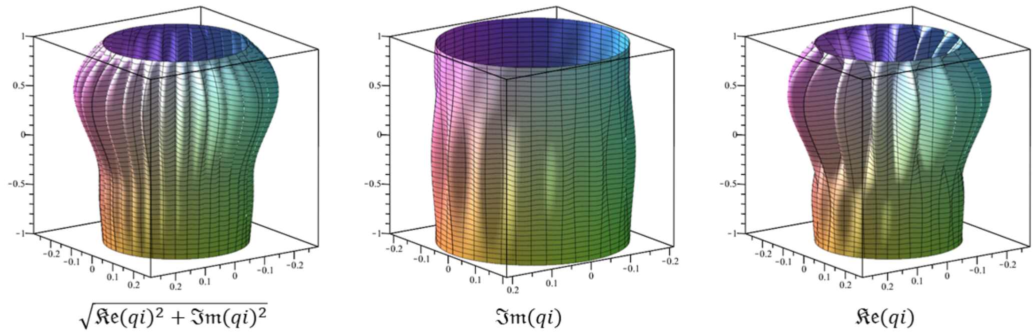

Figure 4.21: Critical flutter mode shape of a VSCL shell with a <85º,45º,85º>$_c$ tow path and S-S boundary conditions ($n_{crit} = 15$).

By comparing the flutter mode shapes of each path, it is concluded that they are geometrically different not only for having a different number of circumferential waves, but also because the deformation at the edge is different, as the cylinders with simply supported edges have slope at their extremities, as it would be expected.

Furthermore, as an example, the $\mathfrak{Re}(\Omega)$ and $\mathfrak{Im}(\Omega)$ plot in relation to p_∞ for the <40º,80º> path was obtained to compare the differences between a shell with C-C boundary conditions and S-S boundary conditions. The plots are present in Figure 4.22. As it was previously stated, it is seen that, in this case, $\mathfrak{Re}(\Omega)$ becomes positive for a lower value of p_∞ for a shell with simply supported edges. Analyzing the variation of $\mathfrak{Im}(\Omega)$, it is seen that lower values for the vibration frequency under flutter were obtained for the shell with S-S boundary conditions.

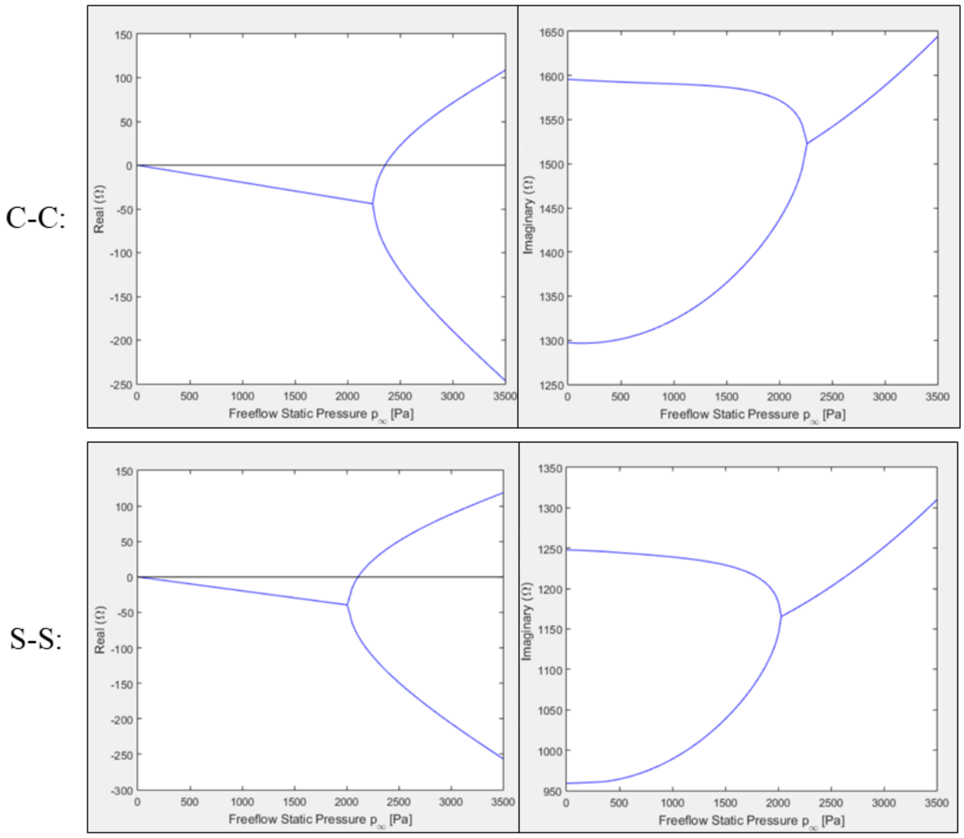

Figure 4.22: $\mathfrak{Re}(\Omega)$ and $\mathfrak{Im}(\Omega)$ variation along p_∞ of the critical flutter mode and its corresponding coupled mode for a shell with C-C and S-S boundary conditions and a <40º,80º> tow path.

Reviewing Table 4.6, it is seen that, even though there is a general decrease in the values of p_{crit} for the S-S boundary conditions, the curvilinear fiber paths still result in higher values of p_{crit} than the calculated constant angle path. However, the true potential of the variable stiffness concept is not well represented, because, while a certain fiber path might be the ideal for a shell with C-C boundary conditions, it is not necessarily ideal path for a shell with S-S boundary conditions.

Table 4.7: Critical free stream pressure p_{crit} for shells with C-C and S-S boundary conditions and linear angle variation paths.

	$<T_0,T_1>$	
Fiber Path	C-C Boundary Conditions	S-S Boundary Conditions
	p_{crit} [Pa]	p_{crit} [Pa]
<40º,80º>	**2368**	2111
<40º,85º>	2280	**2177**
<40º,75º>	2328	2060

Table 4.7 contains the values of p_{crit} for 3 different linear angle variation paths of shells with C-C boundary conditions and S-S boundary conditions. These 3 paths have the same value for the

T_0 parameter, but the T_1 parameter was slightly tweaked.

Of the 3 tested paths, the biggest value of p_{crit} was obtained with the <40º,80º> tow path in the case of the shell with C-C boundary conditions, and it was obtained with the <40º,85º> tow path in the case of the shell with S-S boundary conditions, thus concluding that the ideal path to increase the value of p_{crit} is not the same for shells with different boundary conditions.

4.4 Conclusions

In this chapter, the critical values of free stream static pressure for the occurrence of flutter on variable stiffness composite shells were tested and compared to the values obtained for conventional constant stiffness shells.

The shell and airflow parameters were fixed, C-C boundary conditions were considered, the same lamination setup was always used and only the fiber path properties were changed from case to case. An iterative procedure was used to find fiber path parameters that would result in an increase of p_{crit}, for each type of fiber path. The minimum turning radius manufacturing constraint was considered, and the minimum value of $r_\psi = 635$ mm was set.

Firstly, CSCL shells were analyzed. The biggest value of $p_{crit} = 1474$ Pa was obtained for a tow angle of $\psi = 55$º and it was used as a benchmark to surpass in shells with curvilinear fibers. It is also concluded that, even in CSCL shells, a small variation of tow angle can have a big impact on the value of p_{crit}.

Then, curvilinear fiber paths with 1 segment were tested. With the linear angle variation path an increase in results was achieved. The highest value of $p_{crit} = 2386$ Pa was obtained for a <40º,80º> fiber path. For the constant in-plane curvature path, even higher results were obtained. The biggest one is $p_{crit} = 3164$ Pa for the <25º,85º>$_c$ path.

After these tests, the same types of path were tested again, but repeated in 2 anti-symmetrical segments. For the linear angle variation paths, the highest value of $p_{crit} = 1816$ Pa was obtained for the <85º,55º,85º> path. For the constant in-plane curvature path, the biggest value obtained is $p_{crit} = 2146$ Pa, corresponding to the <85º,45º,85º>$_c$ fiber path.

From these tests, various conclusions are taken. Firstly, it is proven that the values of p_{crit} are significantly sensitive to fiber path variations, and considerable increases of these values were obtained by the use of curvilinear fibers. Comparing to the biggest value obtained for a VSCL shell to the biggest value obtained for a CSCL shell, a relative increase of 114.7% was observed. This value was obtained for the <25º,85º>$_c$ fiber path.

The manufacturing curvature constraint proved to influence significantly the possible increase of p_{crit}. It is observed that higher results were obtained for fiber paths that tend to have big differences between the fiber path parameters T_0 and T_1. The manufacturing constraint limits this difference, and so, while ignoring this constraints, even higher results of p_{crit} can be obtained.

The manufacturing curvature constraint restricted more severely the choice of fiber path parameters in the two segment tow paths. Even though these paths possess more complex geometries and can be more specifically tailored to the shells expected external loads, lower results were obtained for the tow paths with 2 segments than for the ones with 1 segment, due to the decreased flexibility on the choice of T_0 and T_1 parameters.

It is also observed that, for both 1 segment and 2 segment paths, higher results were obtained for the constant in-plane curvature paths, rather than for the linear angle variation ones. Even though that for the same values of T_0 and T_1 the calculated values for the constant curvature paths are lower than the ones for linear angle variation paths, the turning radius for the linear angle variation path is smaller. Therefore, this type of path is more restricted by the curvature constraint and the constant in-plane curvature paths allow to choose values for T_0 and T_1 that result in an increased value of p_{crit} and that are inadmissible for linear angle variation paths.

The critical flutter modes of the shells with the fiber path parameters that yielded the highest values of p_{crit} for each type of path are also graphically represented in this chapter. It is concluded that the tweaking of fiber path parameters differently affects each mode, and therefore, for different fiber paths, the critical flutter mode shapes present different geometries.

The mode frequencies of the CSCL shell with the highest value of p_{crit} are compared with mode frequencies of the VSCL shell with the curvilinear fiber path that results in a higher value of p_{crit}. It is concluded that the shell with a curvilinear fiber path and a higher p_{crit} has a higher difference between the values of the natural frequencies of the critical flutter mode and the corresponding coupled mode. This higher difference in values results in the convergence of $\mathfrak{Im}(\Omega)$ at higher values of p_∞ and, therefore, the value of p_{crit} is increased.

Finally, the fiber paths with the highest values of p_{crit} found for each type of path were tested again, but for shells with simply supported edges. The results obtained for both boundary conditions were compared.

It is seen that the values of p_{crit} obtained in these paths for shells with S-S boundary conditions are lower than those obtained for C-C boundary conditions. The vibration frequencies associated with these flutter modes were also compared, and it is seen that these values tend to also be lower for S-S boundary conditions. More importantly, it is concluded that the ideal fiber path for a shell with C-C boundary conditions may not be ideal for a shell with S-S boundary conditions. The critical flutter mode shapes were also compared between these two boundary conditions and it is found that their geometries differ, not only at the edge, but also on other details like the number of circumferential waves that each has.

Considering all this, the goal of this dissertation is achieved. It is concluded that variable stiffness composite laminate shells present, from a theoretical point of view, a way to significantly increase the critical free stream static pressure at which flutter occurs.

Chapter 5

Conclusions and Future Work

5.1 Summary

In the present dissertation, a linear mathematical model for the dynamic response of a VSCL thin circular cylindrical shell to supersonic airflow was developed and tested to find fiber paths that enabled the increase of the free stream static pressure at which flutter occurs.

Love's first approximation laid the key foundations of the model. The constitutive model for a thin fiber-reinforced composite laminate was used and the elastic matrix defined by this model is a function of the spatial variables to account for the variable stiffness properties of the shell. The equations of motion were obtained through the use of Newton's second law of motion, and the external aerodynamic load was modelled resorting to the linearized piston theory. Both clamped and simply supported boundary conditions were used. The p-version of the finite element method was implemented, where 3 different sets of unidimensional shape functions were combined to obtain the used set of bi-dimensional shape functions. The shell's stiffness and mass matrices were calculated, as well as the aerodynamic stiffness and aerodynamic damping matrices. The developed model has the versatility of representing cylindrical shells with different boundary conditions, geometries and material properties (from isotropic shells to VSCL shells with different lamination setups). However, for the sake of convenience, the model does not represent cases with material or lamination asymmetry along the thickness of the shell.

A convergence test was performed to understand the needed number of shape functions to obtain converged and stable results. For these tests, the natural frequencies of a shell were calculated. It was concluded that the number of shape functions used should take into account the type of studied vibration modes. This is mainly relevant in cases where it is necessary to obtain a vibration mode shape with n circumferential waves, since, if the sinusoidal shape functions $h_u = h_w = cos(n \cdot \theta)$ and $h_v = sin(n \cdot \theta)$ are not a part of the used set, then that mode shape is not reliably obtained in the final results. In addition to that, the number of shape functions that allows for a close approximation of the shape of the shell's displacement field was also found.

The model was then validated by calculating the shell's natural frequencies and natural mode shapes under different parameters and comparing the obtained values with those obtained by other authors. Finally, the free stream static pressure at which flutter occurs was calculated and also compared, where the other airflow's parameters were set as constant. The results obtained by the solution of both the free vibration eigenvalue problem and the flutter eigenvalue problem yielded similar results to those found in the literature. The eigenvalues and the eigenvectors obtained by the solution of the flutter problem are complex conjugates. The real part of one flutter mode's eigenvalues has the same value of the real part of other mode's conjugate pair for low values of free flow pressure and they bifurcate at a higher value of pressure. In contrast, the imaginary part of those modes is different for low values of pressure and then converge into the same value at the same point that the real part bifurcates. Flutter occurs for the pressure value at which the real part of one complex eigenvalue becomes positive and, therefore, the dynamic response of the system becomes unstable. This is the expected behaviour of a shell in response to supersonic airflow and, therefore, the model was considered validated.

With the model developed, tested and validated, various curvilinear fiber paths were tested with the intent of increasing the critical free stream static pressure at which aeroelastic flutter occurs, comparing to conventional constant stiffness shells. Five types of fiber paths were considered for the tests: the constant angle path (which corresponds to the conventional unidirectional fibers), the linear angle variation path (with 1 and 2 segments) and the constant in-plane curvature path (also with 1 and 2 segments). These paths are defined by mathematical expressions, which was useful as it allowed to control the path's shape by tweaking its parameters. The paths were considered to be ideal and no manufacturing defects and imperfections were modelled. However, the minimum turning radius constraint was taken into account as to ensure that manufacturable paths were tested. To find the fiber paths with the highest possible value of critical free stream pressure p_{crit}, an iterative method was used, where the fiber path parameters were progressively tweaked in the direction of an increasing p_{crit}. Furthermore, the number of shape functions was chosen so that mode shapes with up to $n = 25$ circumferential waves could be obtained, since it was found that flutter modes tend to present shapes with a high number of waves.

Firstly, an analysis of a shell with clamped boundary conditions was performed. The values for p_{crit} of conventional constant stiffness laminate shells were calculated and the highest obtained value was used as a benchmark to surpass with the use of curvilinear fiber paths. Each defined type of fiber path was tested in shells with the same parameters and lamination setup, where only the fiber path parameters was altered. The biggest overall result was obtained for a constant in-plane curvature path, where a relative increase of 114.7% of p_{crit} was achieved in relation to the highest value obtained for the constant stiffness shell. By neglecting the maximum curvature manufacturing constraint, even higher values of p_{crit} can be achieved.

It was proven that the values of p_{crit} are significantly sensitive to variations in fiber angles, which shows the great potential of the use of the variable stiffness concept in shells submitted to supersonic airflow where light weight design is key. The tweaking of fiber parameters is, nevertheless, a complex process, since the critical flutter mode shape for a given fiber path may be geometrically different than the critical flutter mode shape for a different path. This means that, while a fiber path may increase the pressure value at which a given mode achieves flutter, it may decrease that value for a different mode.

It was also found by analyzing the critical mode frequency variations with the free steam pressure variable that the difference between the mode's natural frequency and the corresponding coupled mode's natural frequency is higher for fiber paths with higher values of p_{crit}, since these frequencies start further apart in the pressure plot and, therefore, require higher values of pressure to converge and then finally achieve flutter.

Finally, the fiber paths that obtained the highest values of p_{crit} were tested again on shells with the same parameters, but with simply supported boundary conditions. A general decrease in critical pressure values was observed and it was found that the ideal fiber path to increase p_{crit} is different for different boundary conditions. As expected, different flutter mode shapes were also achieved by changing the boundary conditions, due to differences in both the displacement in the edge of the shell, as well as in the number of circumferential waves.

Concluding, this work allowed to understand the potential of VSCL structures in the prevention of supersonic flutter. A significant sensitivity of critical free stream pressure results to changes in fiber paths were recorded, and this type of design is therefore proven to have great potential to improve the mechanical performance of shells in this type of application.

5.2 Future Work

This work has proven that variable stiffness composite laminates present a great capacity of prevention of aeroelastic supersonic flutter. However, this works presents some simplifications that, in one hand, allowed to get a more clear vision of the raw potential of these structures, but on the other does not take into account some mechanics that would distance the results obtained in this theoretical work with those that would be obtained in real life applications. Thus, this section presents some suggestions for ways to improve the knowledge of the topics addressed in this dissertation.

The used procedure for searching fiber paths to prevent aeroelastic flutter was repetitive and was not able to acquire the exact optimal fiber path parameters for this context. The implementation of an optimization algorithm would be interesting to truly understand what are the highest values of critical flutter pressure that VSCL can achieve, as well as to facilitate the process of finding said paths.

The model developed for this work has various theoretical assumptions and so, increasing the model's complexity in a way that brings the obtained results closer to reality is extremely relevant. The modelling of manufacturing defects, such as gaps and overlaps is a potential way of doing this, considering that these imperfections might have a considerable impact on the mechanical performance of the structure.

Furthermore, performing experimental tests to study both the free vibrations and the flutter phenomenon of VSCL shells would allow to understand how well the developed finite element method represents real life cases.

Shells are commonly used structures in engineering and can acquire many geometries. It would be interesting to test VSCL in shells with other geometries, like cylinders with variable radius and thickness and other more complex shells. In addition to that, a model for a thick shell could be developed, since the developed mathematical model considered thin cylindrical shells that do not consider the effect of shear deformation along the shell's thickness.

Lastly, the development of a non-linear mathematical model would allow to better understand how a VSCL dynamically reacts under flutter conditions, since, in reality, the structure's vibration amplitude does not exponentially grow forever.

References

[1] Blom AW. Structural performance of fiber-placed, variable-stiffness composite conical and cylindrical shells. 2010.

[2] Aragh BS, Farahani EB, Xu B, Ghasemnejad H, Mansur W. Manufacturable insight into modelling and design considerations in fibre-steered composite laminates: State of the art and perspective. Computer Methods in Applied Mechanics and Engineering. 2021;379:113752.

[3] Evans DO. Fiber placement. Springer; 1998.

[4] Tatting BF. Analysis and design of variable stiffness composite cylinders. Virginia Tech; Doctoral's degree dissertation, 1998.

[5] Waldhart C. Analysis of tow-placed, variable-stiffness laminates; Master's degree dissertation, 1996.

[6] Dowell EH, Curtiss H, Scanlan RH, Sisto F. A modern course in aeroelasticity. Springer; Linköping, Sweden, 2021.

[7] Leissa AW. Vibration of shells. vol. 288. Scientific and Technical Information Office, National Aeronautics and Space Administration; 1973.

[8] Reddy JN. Mechanics of laminated composite plates and shells: theory and analysis. CRC press; 2003.

[9] Amabili M. Nonlinear Vibrations and Stability of Shells and Plates. Cambridge University Press; 2008.

[10] Qatu MS. Vibration of laminated shells and plates. Elsevier; 2004.

[11] Kaw AK. Mechanics of composite materials. CRC press; 2005.

[12] Petyt M. Introduction to finite element vibration analysis. Cambridge university press; 2010.

[13] Pellicano F. Vibrations of circular cylindrical shells: theory and experiments. Journal of Sound and Vibration. 2007;303(1-2):154-70.

[14] Timarci T, Soldatos K. Vibrations of angle-ply laminated circular cylindrical shells subjected to different sets of edge boundary conditions. Journal of Engineering Mathematics. 2000;37(1):211-30.

[15] Loy C, Lam K, Hua L, Liu G. Vibration of antisymmetric angle-ply laminated cylindrical panels with different boundary conditions. The Quarterly Journal of Mechanics and Applied Mathematics. 1999;52(1):55-71.

[16] Zhang X. Vibration analysis of cross-ply laminated composite cylindrical shells using the wave propagation approach. Applied Acoustics. 2001;62(11):1221-8.

[17] Song X, Han Q, Zhai J. Vibration analyses of symmetrically laminated composite cylindrical shells with arbitrary boundaries conditions via Rayleigh–Ritz method. Composite Structures. 2015;134:820-30.

[18] Lam K, Loy C. Influence of boundary conditions for a thin laminated rotating cylindrical shell. Composite structures. 1998;41(3-4):215-28.

[19] Lam K, Loy C. Analysis of rotating laminated cylindrical shells by different thin shell theories. Journal of Sound and Vibration. 1995;186(1):23-35.

[20] Qin Z, Chu F, Zu J. Free vibrations of cylindrical shells with arbitrary boundary conditions: a comparison study. International Journal of Mechanical Sciences. 2017;133:91-9.

[21] Zhao J, Choe K, Shuai C, Wang A, Wang Q. Free vibration analysis of laminated composite elliptic cylinders with general boundary conditions. Composites Part B: Engineering. 2019;158:55-66.

[22] Khalili S, Davar A, Fard KM. Free vibration analysis of homogeneous isotropic circular cylindrical shells based on a new three-dimensional refined higher-order theory. International journal of Mechanical sciences. 2012;56(1):1-25.

[23] Haddadpour H, Mahmoudkhani S, Navazi H. Free vibration analysis of functionally graded cylindrical shells including thermal effects. Thin-walled Structures. 2007;45(6):591-9.

[24] Xie X, Jin G, Yan Y, Shi S, Liu Z. Free vibration analysis of composite laminated cylindrical shells using the Haar wavelet method. Composite Structures. 2014;109:169-77.

[25] Hosokawa K, Murayama M, Sakata T. Free vibration analysis of angle-ply laminated shallow cylindrical shell with clamped edges. J Vib Acoust. 2001;123(2):188-97.

[26] Lakis AA, Paidoussis M. Dynamic analysis of axially non-uniform thin cylindrical shells. Journal of Mechanical Engineering Science. 1972;14(1):49-71.

[27] Serhat G. Design of Circular Composite Cylinders for Optimal Natural Frequencies. Materials. 2021;14(12):3203.

[28] Jin G, Ye T, Chen Y, Su Z, Yan Y. An exact solution for the free vibration analysis of laminated composite cylindrical shells with general elastic boundary conditions. Composite Structures. 2013;106:114-27.

[29] Lozano GG, Tiwari A, Turner C, Astwood S. A review on design for manufacture of variable stiffness composite laminates. Proceedings of the Institution of Mechanical Engineers, Part B: Journal of Engineering Manufacture. 2016;230(6):981-92.

[30] Heinecke F, Willberg C. Manufacturing-induced imperfections in composite parts manufactured via automated fiber placement. Journal of Composites Science. 2019;3(2):56.

[31] Fayazbakhsh K, Nik MA, Pasini D, Lessard L. Defect layer method to capture effect of gaps and overlaps in variable stiffness laminates made by Automated Fiber Placement. Composite Structures. 2013;97:245-51.

[32] Blom AW, Lopes CS, Kromwijk PJ, Gurdal Z, Camanho PP. A theoretical model to study the influence of tow-drop areas on the stiffness and strength of variable-stiffness laminates. Journal of Composite Materials. 2009.

[33] Labans E, Bisagni C. Buckling and free vibration study of variable and constant-stiffness cylindrical shells. Composite Structures. 2019;210:446-57.

[34] Rouhi M, Ghayoor H, Fortin-Simpson J, Zacchia TT, Hoa SV, Hojjati M. Design, manufacturing, and testing of a variable stiffness composite cylinder. Composite Structures. 2018;184:146-52.

[35] Wu Z, Weaver PM, Raju G, Kim BC. Buckling analysis and optimisation of variable angle tow composite plates. Thin-walled structures. 2012;60:163-72.

[36] Tian Y, Pu S, Zong Z, Shi T, Xia Q. Optimization of variable stiffness laminates with gap-overlap and curvature constraints. Composite Structures. 2019;230:111494.

[37] Carvalho J, Sohouli A, Suleman A. Fundamental Frequency Optimization of Variable Angle Tow Laminates with Embedded Gap Defects. Journal of Composites Science. 2022;6(2):64.

[38] Fayazbakhsh K. The impact of gaps and overlaps on variable stiffness composites manufactured by automated fiber placement; Doctoral's degree dissertation, 2014.

[39] Marouene A, Boukhili R, Chen J, Yousefpour A. Effects of gaps and overlaps on the buckling behavior of an optimally designed variable-stiffness composite laminates–A numerical and experimental study. Composite Structures. 2016;140:556-66.

[40] Blom AW, Abdalla MM, Gürdal Z. Optimization of course locations in fiber-placed panels for general fiber angle distributions. Composites Science and Technology. 2010;70(4):564-70.

[41] Nik MA. Surrogate-based multi-objective optimization of variable stiffness composites with embedded defects induced by Automated Fiber Placement. McGill University (Canada); 2014.

[42] Wu KC, Stanford BK, Hrinda GA, Wang Z, Martin RA, Kim HA. Structural assessment of advanced tow-steered shells. In: 54th AIAA/ASME/ASCE/AHS/ASC structures, structural dynamics, and materials conference; 2013. p. 1769.

[43] Khani A, IJsselmuiden ST, Abdalla MM, Gürdal Z. Design of variable stiffness panels for maximum strength using lamination parameters. Composites Part B: Engineering. 2011;42(3):546-52.

[44] Falcó O, Mayugo J, Lopes C, Gascons N, Turon A, Costa J. Variable-stiffness composite panels: As-manufactured modeling and its influence on the failure behavior. Composites Part B: Engineering. 2014;56:660-9.

[45] Cairns DS, Ilcewicz LB, Walker T. Response of automated tow placed laminates to stress concentrations. In: NASA. Langley Research Center, Third NASA Advanced Composites Technology Conference, Volume 1, Part 2; 1993. .

[46] Dang TD, Hallet SR, Kim BC, Cahain YL, Butler R, Liu W. Modelling of as manufactured geometry for prediction of impact and compression after impact behaviour of variable angle tow laminates. Journal of Composite Materials. 2015;49(12):1423-38.

[47] Pan H, Qu W, Yang D, Huang Q, Li J, Ke Y. Design and Optimization of Variable Stiffness Composite Cylinders With the Consideration of Manufacturing Interaction. Applied Composite Materials. 2022:1-25.

[48] Wu KC. Design and analysis of tow-steered composite shells using fiber placement. 2008.

[49] Wu K, Tatting B, Smith B, Stevens R, Occhipinti G, Swift J, et al. Design and manufacturing of tow-steered composite shells using fiber placement. In: 50th AIAA/ASME/ASCE/AHS/ASC Structures, Structural Dynamics, and Materials Conference 17th AIAA/ASME/AHS Adaptive Structures Conference 11th AIAA No; 2009. p. 2700.

[50] Lopes CS. Damage and failure of non-conventional composite laminates. TU Delft, Faculteit Luchtvaart-en Ruimtevaarttechniek, 2009.

[51] Ribeiro P. Linear modes of vibration of cylindrical shells in composite laminates reinforced by curvilinear fibres. Journal of Vibration and Control. 2016;22(20):4141-58.

[52] Akhavan H. Non-linear vibrations of tow placed variable stiffness composite laminates. Universidade do Porto (Portugal); Doctoral's degree dissertation, 2015.

[53] Antunes AM, Ribeiro P, Rodrigues JD, Akhavan H. Modal analysis of a variable stiffness composite laminated plate with diverse boundary conditions: experiments and modelling. Composite Structures. 2020;239:111974.

[54] Rodrigues JD, Ribeiro P, Akhavan H. Experimental and finite element modal analysis of variable stiffness composite laminated plates. In: Proceedings of the 11th Biennial International Conference on Vibration Problems (ICOVP-2013); 2013. p. 30.

[55] Sabri F, Lakis AA. Finite element method applied to supersonic flutter of circular cylindrical shells. AIAA journal. 2010;48(1):73-81.

[56] Bismarck-Nasr MN. Finite element method applied to the supersonic flutter of circular cylindrical shells. International Journal for Numerical Methods in Engineering. 1976;10(2):423-35.

[57] Olson MD. Supersonic flutter of circular cylindrical shells. California Institute of Technology; Doctoral's degree dissertation, 1966.

[58] Carter L, Stearman R. Some aspects of cylindrical shell panel flutter. AIAA Journal. 1968;6(1):37-43.

[59] Ganapathi M, Varadan T, Jijen J. Field-consistent element applied to flutter analysis of circular cylindrical shells. Journal of Sound and Vibration. 1994;171(4):509-27.

[60] Evensen DA, Olson MD. Nonlinear flutter of a circular cylindrical shell in supersonic flow; No. NASA-TN-D-4265; 1967.

[61] Amabili M, Pellicano F. Multimode approach to nonlinear supersonic flutter of imperfect circular cylindrical shells. J Appl Mech. 2002;69(2):117-29.

[62] Chen J, Li QS. Nonlinear aeroelastic flutter and dynamic response of composite laminated cylindrical shell in supersonic air flow. Composite Structures. 2017;168:474-84.

[63] Avramov K, Chernobryvko M, Uspensky B, Seitkazenova K, Myrzaliyev D. Self-sustained vibrations of functionally graded carbon nanotubes-reinforced composite cylindrical shells in supersonic flow. Nonlinear Dynamics. 2019;98(3):1853-76.

[64] Brouwer KR, Perez RA, Beberniss TJ, Spottswood SM, Ehrhardt DA, Wiebe R. Investigation of aeroelastic instabilities for a thin panel in turbulent flow. Nonlinear Dynamics. 2021;104(4):3323-46.

[65] Camacho PSF. Aeroelastic Analysis of Hybrid Multiscale Composite Plates. 2020.

[66] Camacho P, Akhavan H, Ribeiro P. Linear aeroelastic analysis of cantilever hybrid composite laminated plates with curvilinear fibres and carbon nanotubes. Composite Structures. 2021;266:113765.

[67] Akhavan H, Ribeiro P. Stability and bifurcations in oscillations of composite laminates with curvilinear fibres under a supersonic airflow. Nonlinear Dynamics. 2021;103(4):3037-58.

[68] Akhavan H, Ribeiro P. Reduced-order models for nonlinear flutter of composite laminates with curvilinear fibers. AIAA Journal. 2019;57(7):3026-39.

[69] Akhavan H, Ribeiro P. Aeroelasticity of composite plates with curvilinear fibres in supersonic flow. Composite Structures. 2018;194:335-44.

[70] Ashley H, Zartarian G. Piston theory-a new aerodynamic tool for the aeroelastician. Journal of the Aeronautical Sciences. 1956;23(12):1109-18.

[71] Barr GW, Stearman RO. Influence of a supersonic flowfield on the elastic stability of cylindrical shells. AIAA Journal. 1970;8(6):993-1000.

[72] Ribeiro P. Hierarchical finite element analyses of geometrically non-linear vibration of beams and plane frames. Journal of Sound and Vibration. 2001;246(2):225-44.

[73] Ribeiro P, Thomas O. Nonlinear modes of vibration and internal resonances in nonlocal beams. Journal of Computational and Nonlinear Dynamics. 2017;12(3).

[74] Babuška I, Suri M. The p and h-p versions of the finite element method, basic principles and properties. SIAM review. 1994;36(4):578-632.

[75] Bardell N. The application of symbolic computing to the hierarchical finite element method. International Journal for Numerical Methods in Engineering. 1989;28(5):1181-204.

[76] Gonçalves EH, Ribeiro P. Modes of vibration of single-and double-walled CNTs with an attached mass by a non-local shell model. Journal of Vibration Engineering & Technologies. 2022;10(1):375-93.

[77] Narita Y, Ohta Y, Yamada G, Kobayashi Y. Analytical method for vibration of angle-ply cylindrical shells having arbitrary edges. AIAA journal. 1992;30(3):790-6.

[78] Olson MD, Fung Y. Comparing theory and experiment for the supersonic flutter of circular cylindrical shells. AIAA Journal. 1967;5(10):1849-56.